

Estimation of particulate organic carbon export to the ocean from lateral degradations of tropical peatland coasts

Hiroki Kagawa¹, Koichi Yamamoto¹, Sigit Sutikno², Muhammad Haidar^{3,4}, Noerdin Basir⁵, Atsushi Koyama⁶, Ariyo Kanno¹, Yoshihisa Akamatsu¹, Motoyuki Suzuki¹

5 ¹Graduate School of Science and Technology for Innovation, Yamaguchi University, Ube city, Yamaguchi, Japan

²Faculty of Engineering, University of Riau, Pekanbaru, Riau province, Indonesia

³The Geospatial Information Agency of Indonesia, Jakarta, Indonesia

⁴Institute of Industrial Science, The University of Tokyo, Tokyo, Japan

⁵The state polytechnic of Bengkalis, Bengkalis, Riau province, Indonesia

10 ⁶Faculty of Engineering, University of Miyazaki, Miyazaki city, Miyazaki, Japan

Correspondence to: Koichi Yamamoto (k_yama@yamaguchi-u.ac.jp)

Abstract. Peatlands serve as long-term carbon sinks and are distributed across subarctic, Arctic, and tropical regions. However, in tropical and permafrost-dominated coastal areas, coastal erosion and peat mass movement events (PMMs) have emerged as major contributors to peatland degradation. These processes are thought to drive territorial loss and facilitate the export of particulate organic carbon (POC) to marine environments in the form of peaty debris. This study quantifies POC export and assesses the extent of peatland degradation driven by coastal erosion and PMMs in tropical coastal peatlands. Between 2017 and 2018, PMMs impacted approximately 68 ha of land in the northern part of Bengkalis Island, Indonesia, with collapse volumes ranging from 491 to 85,173 m³. Notably, a PMM event on 27 December 2014 resulted in an elevation loss of approximately 2 m, primarily triggered by flooding associated with the failure of a peat weir following 192 mm of rainfall over four days. An analysis of coastline changes from 2018 to 2021 revealed that erosion rates varied by land cover type. Oil palm plantations experienced erosion rates of 3.5 m per 30 days, exceeding those observed in mangrove areas and peat swamp forests. The highest recorded rate—24.8 m per 30 days—occurred during periods of elevated wind speeds and intense wave activity, highlighting the role of seasonal climatic drivers in accelerating peatland degradation. Estimated POC fluxes ranged from 6.35 to 23.9 ktC yr⁻¹ due to coastal erosion and 4.45 to 17.1 ktC from PMMs—values approximately 295 to 1,089 times greater than typical riverine POC export in tropical wet regions. These findings reveal a previously underrecognized carbon export pathway from tropical peatland coasts to the ocean and suggest that coastal peatland degradation may be a significant yet overlooked component of the marine carbon budget. Further research is essential to clarify the fate of exported peat—specifically, whether it remains suspended, settles on the seafloor, or undergoes decomposition in marine environments.

~~Peatlands, which function as long-term carbon sinks, are distributed across subarctic, Arctic, and tropical regions. However, coastal erosion and peat mass movement events (PMMs) are increasingly recognized as significant drivers of peatland degradation, particularly in tropical and permafrost-dominated coastal areas. In the tropics, rapid coastal erosion and PMMs contribute to territorial loss and the export of particulate organic carbon (POC) to the ocean. Similarly, in the Arctic~~

and subarctic regions, coastal retreat and permafrost thaw result in substantial peat loss. The fate of eroded peat whether it remains suspended, settles on the seafloor, or contributes to marine carbon sequestration remains poorly understood. This study quantifies the export of POC and evaluates the extent of peatland degradation due to coastal erosion and PMMs along the northern coast of Bengkalis Island, Indonesia, using field surveys and remote sensing. Between 2017 and 2018, PMMs affected 68 ha, with collapse volumes ranging from 491 m³ to 85,173 m³. UAV-based photogrammetry and cross-sectional topographic surveys revealed elevation losses of 2.01 to 2.07 m over short timescales, triggered by heavy rain and sudden fluctuations in water level. From 2018 to 2021, the rates of coastal erosion varied by land cover type, with erosion in oil palm plantations (3.5 m per 30 days) exceeding that in mangrove and peat swamp forests. The highest recorded rate of 24.8 m per 30 days coincided with high wind speeds and wave activity, emphasizing the role of seasonal climatic forces in peatland degradation. Estimated POC fluxes ranged from 6.35 to 23.9 ktC yr⁻¹ due to coastal erosion and 4.45 to 17.1 ktC from PMMs, values 295 to 1,089 times higher than typical riverine POC transport from tropical humid regions. This study identifies a new carbon export pathway from tropical peatland coasts to marine environments. It demonstrates that coastal peatland degradation may represent a previously overlooked contributor to marine carbon budgets. More research is needed to clarify the fate of exported peat, determining whether it remains suspended, settles on the seafloor, or undergoes further degradation.

1 Introduction

1 Introduction

Recently studies have increasingly recognized that tropical coastal peatlands may contribute to lateral carbon export via coastal erosion and peat mass movement events (PMMs). However, this pathway remains underexplored, particularly in contrast to well documented erosion processes in boreal and Arctic regions. This limited attention may stem from logistical challenges in accessing remote tropical sites, a lack of long term monitoring, and fewer reported failure events compared to boreal peatlands. Peat is a partially decomposed organic matter that accumulates under anoxic and waterlogged conditions, leading to the formation of peatlands across subarctic, arctic, and tropical zones and playing a significant role in the global carbon cycle throughout the Holocene. Globally, peatlands have functioned as persistent carbon sinks, storing more than 600 GtC at a sequestration rate exceeding 5 GtC per century (Kleinen et al., 2010; Yu, 2011). Despite occupying only ~3% of the Earth's land surface, they account for ~6% of the global soil carbon stock (Page et al., 2011; Scharlemann et al., 2014).

Tropical peatlands, primarily located in Southeast Asia, are categorized into inland and coastal types (Dommain et al., 2011). Coastal peatlands, which developed atop marine clays and mangrove sediments following Holocene sea level stabilization, are especially widespread along low-lying coastlines in Sumatra and Borneo, with Riau Province alone accounting for over 60% of Sumatra's coastal peat area (Ritung et al., 2011). Though tropical peatlands represent just 11% of

global peatland area, they store over 68.5 Gt of carbon, including an estimated 57.4 Gt in Indonesia (Page et al., 2011). Despite their limited spatial extent, their disproportionately large carbon storage underscores their global significance.

70 Yet, these ecosystems are increasingly threatened by deforestation, drainage, and fire, shifting them from long-standing carbon sinks to net sources of emissions (Hooijer et al., 2010; Couwenberg et al., 2010). In addition to fire induced carbon loss, physical degradation such as coastal erosion and PMMs are emerging concerns. On Bengkalis Island, for instance, the loss of protective mangroves has exposed peat cliffs to direct tidal and wave action, triggering toppling failure, rotational sliding, and cantilever collapse (Basir et al., 2023). These processes may represent a direct and measurable pathway for lateral particulate organic carbon (POC) transport to marine systems, yet their extent and magnitude remain poorly quantified (Fig.1 and Fig.2).

75 This study seeks to address this knowledge gap by investigating a representative tropical coastal peatland system undergoing active degradation—Bengkalis Island in Riau Province, Indonesia. While lateral erosion and mass movement have been widely reported in Arctic and boreal peatlands, the geoclimatic contrasts between these regions and tropical coasts underscore the uniqueness of tropical peatland degradation. For example, the Bykovsky Peninsula in Siberia exhibits erosion of ice-rich permafrost bluffs under the influence of storm activity and thawing, with buried Holocene peat and ice wedges
80 common in the stratigraphy (Lantuit et al., 2011). Similarly, Arctic coasts in Alaska are dominated by cryogenic processes, with erosion influenced by permafrost melt, short ice free seasons, and brackish water dynamics.

In contrast, tropical coastal peatlands like those in Indonesia lack permafrost and ground ice, experience high rainfall year round, and are dominated by freshwater hydrology. Their flat geomorphology contrasts with the thermokarst features, thaw slumps, and polygonal tundra of the Arctic, and their degradation is governed by tidal energy and monsoon driven storms
85 rather than freeze thaw cycles. Meanwhile, the southern Baltic Sea region illustrates a different model of peatland retreat, where Holocene sea level rise and wave driven abrasion remove glacially derived peat layers underlain by lacustrine and glacial till sediments (Furmanczyk and Dudzinska-Nowak, 2009).

In the British Isles, raised and blanket bogs—shallow, ombrotrophic systems reliant on precipitation—commonly undergo failure modes such as bog bursts and bogflows (Dykes and Warburton, 2007; Boylan et al., 2008). These contrasts
90 further highlight the distinct nature of tropical peat swamp failures, which are deeper, influenced by groundwater, and underlain by marine or fluvial sediments. Events such as the peat landslide on Bengkalis Island (Yamamoto et al., 2019) and the 1966 failure in Malaysia (Wilford, 1966) suggest that tropical PMMs share some morphological traits with boreal failures but arise under different hydrological and structural conditions. On Bengkalis Island, coastal landslide has occurred that closely resemble bog bursts observed in boreal peatlands (Dykes and Warburton, 2007). The residual landforms of these bog bursts
95 exhibit crack patterns like those described in progressive failure, a mechanism well known in rock mass collapse, as defined by Bjerrum, 1967.

Despite these differences, the implications for carbon cycling may be comparable. Globally, POC exported from riverine systems is estimated at 110–230 MtC yr⁻¹ (Galy et al., 2015), yet erosion of organic rich soils—including peat—has been increasingly recognized as a contributor to marine carbon budgets (Hilton et al., 2015). Particularly in tropical coastal

100 ~~zones, the direct mobilization of peat-derived POC into adjacent seas may represent a previously overlooked pathway of land-to-ocean carbon flux. If this exported material is buried in marine sediments, it could serve as a long-term carbon sink.~~

~~This study focuses on Bengkalis Island in Riau Province, Indonesia, as a representative site of tropical coastal peatland degradation. It aims to assess the geomorphic changes induced by coastal erosion and PMMs and to quantify the associated export of particulate organic carbon. By integrating these findings within a broader biogeographic and geoclimatic framework, this study seeks to fill a critical gap in understanding the role of tropical coastal peatlands in global carbon cycling. In the present study, we employ the conceptual model illustrated in Fig. 1 and Fig. 2 to integrate coastal erosion processes and peat mass movement events.~~

~~Peat is a partially decomposed organic matter that accumulates under conditions such as low temperatures and high humidity, leading to the formation of peatlands. Fig. 1 shows the global distribution of peatlands. These peatlands are distributed across subarctic, arctic, and tropical regions. Throughout the Holocene, peatlands have acted as sustainable carbon sinks, sequestering more than 600 GtC at an average rate exceeding 5 GtC per century (Kleinen et al., 2010; Yu, 2011). The global peatland area has been estimated to range from a minimum of 3,969,831 km² to a maximum of 4,258,068 km², with an intermediate estimate of 3,985,000 km² (Osaki and Tsuji, 2016). The Earth's land area is approximately 13 billion ha (Ministry of the Environment White Paper, 2002), with peatlands accounting for 3.05% to 3.28% of the total land area. Although peatlands cover only about 3% of the Earth's land area, they store approximately 6% of the Earth's total carbon (Page et al., 2011; Scharlemann et al., 2014).~~

~~Tropical peatlands are classified into inland peatlands, which typically form in poorly drained inland areas, and coastal peatlands, which develop in marine clays or mangrove sediments within approximately 80 km of the coast (Dommain et al., 2011). The formation of coastal peatlands is closely related to changes in sea level. The rise in sea level after the last ice age resulted in the formation of coastal peatlands, which later evolved into peat domes and inland peatlands around 14,000 years before present (kyBP). Furthermore, the submergence of Sundaland and the emergence of the Java Sea and the Strait of Malacca led to the formation of coastal peatlands when the sea level stabilised between 7,000 and 4,000 years before the present (Dommain et al., 2011). Coastal peatlands are prevalent along the coastlines of Borneo and Sumatra, with 60.1% of Sumatra's coastal peatland area located in Riau Province (Ritung et al., 2011). Tropical peatlands, which occupy 11% of the global peatland area, approximately 56% of the estimated carbon stock of 68.5 Gt in Southeast Asia, Indonesia holds 57.4 Gt of this carbon (Page et al., 2011). However, rapid forest clearing, extensive plantation development and repeated peat fire outbreaks due to drainage have led to substantial carbon emissions, making Indonesian tropical peatlands a global concern (Page et al., 2002; Couwenberg et al., 2010; Hooijer et al., 2010; Frohking et al., 2011). Therefore, Extensive studies on the carbon balance of tropical peatlands, including the biogenic oxidation of peat and other processes, have shown that the seasonality of rainfall, including El Niño-Southern Oscillation (ENSO) events, significantly affects the carbon balance (Hirano et al., 2007, 2012).~~

~~In tropical peatlands, rapid coastal erosion (Fig. 2a) and increased peat mass movement events (PMMs) (Fig. 2b) are of particular concern regarding territorial loss (Fig. 2c) (Sutikno et al., 2017; Yamamoto et al., 2019). Fig. 3 shows a schematic~~

of coastal erosion. Post-erosion coastal topography typically consists of steep cliffs with vegetated areas and the sea immediately adjacent and differentiated by clear boundaries. Additionally, PMMs and peaty debris fan (Evans and Warburton, 2007; Yamamoto et al., 2019) along the coast were identifiable, with clear boundaries demarcated in the hinterland areas of peaty debris fans where land collapses occurred. The coastline in the eroded coastal areas was defined as the opening of a collapsed area abutting a peaty debris fan. In the tropical peatland of Bengkalis Island, Riau Province, Indonesia, research has shown that the decline of the northern coastal mangrove area has led to the exposure of peat deposits along the shoreline. As a result, three types of erosion and progressive failure mechanisms—toppling failure, rotational sliding, and cantilever failure—are actively occurring, driven by tidal and wave conditions (Basir et al., 2023).

As shown in Fig. 1, peatlands worldwide are widely distributed along coastal areas. Among global peatlands, cases of coastal erosion have been more frequently documented in permafrost-dominated regions (Lantuit et al., 2011; Yunker et al., 1991; Brown et al., 2003; Kreuzburg et al., 2018). In the Arctic, ice-rich coastal areas are particularly vulnerable to erosion. One such site, the Bykovsky Peninsula in northern Siberia, is located along the Lena River Delta (Fig. 1a), extending approximately 150 km along the coastline. Coastal erosion rates in this region have been investigated over a 55-year period (1951–2006) using aerial photographs and satellite imagery, alongside in-situ meteorological and tidal data to analyse erosion mechanisms (Lantuit et al., 2011). The results reveal that annual erosion rates exhibit significant interannual and decadal-scale variability. At the Bykovsky Peninsula, sediment accumulation rates reach up to 5.00 m yr^{-1} in certain areas, while the most affected locations experience coastal retreat at rates of up to 10.00 m yr^{-1} . Specifically, the site recorded an average erosion rate of 1.09 m yr^{-1} between 1986 and 2006, while a higher rate of 2.06 m yr^{-1} was observed from 1975 to 1981. The local coastal morphology varies, ranging from relatively stable vegetated slopes to nearly vertical cliffs, with some areas featuring escarpments up to 45 m in height. The geological composition consists of silt, sand, peat, and complex deposits from the Holocene period. Focusing on the summer-to-autumn period in the Arctic (1 June to 15 October, approximately 4.5 per 30 days), storms were defined as events where wind speeds reached 10 m s^{-1} or higher for at least six hours. Based on this definition, 665 storms were recorded between 1958 and 2006, corresponding to an average annual occurrence of approximately 13.6 storms. While storms are often assumed to play a significant role in coastal erosion, no direct correlation has been demonstrated. In permafrost-dominated coastal regions, a "lag effect" (Lantuit and Pollard, 2008) has been identified, where the peak of coastal erosion does not coincide with the peak of storm activity.

Yunker et al., 1991 divided the coastline along the Beaufort Sea from Cape Dalhousie to the Alaska border into 776 coastal segments. For each segment, they calculated the rate of coastal retreat and multiplied it by the thickness of the peat layer to estimate the annual flux of peat material into the Beaufort Sea (Fig. 1b).

At Elson Lagoon, Alaska, a time-series of coastal erosion rates along a 10.8 km stretch of the lagoon shoreline was determined by georeferencing aerial photographs and high-resolution satellite imagery from 1949 to 2000 (Fig. 1c). The coastline retreated at an average rate of 0.56 m yr^{-1} from 1948 to 1979, and this rate increased by 47% to 0.86 m yr^{-1} from 1979 to 2000. During this latter period, a total of 28 hectares of land was lost. In the Arctic, coastal erosion is restricted to the ice-free period of approximately 3–4 months yr^{-1} . Along some sections of the Arctic coastline, erosion rates exceeding 10 m

yr⁻¹ have been recorded, while the regional average ranges from 2 to 6 m yr⁻¹ (Rachold et al., 2002). Observations of coastal retreat rates and coastal processes along the Barrow coastline, Alaska, began in the late 1940s and continued into the early 1980s (MacCarthy 1953; Harper 1978; Hume and Schalk 1967; Hume et al., 1972). Harper, 1978 reported that the coastline between Barrow Bay and Peard Bay (a 75 km stretch) experienced an average retreat rate of 0.31 m yr⁻¹ from 1949 to 1976. In the Barrow region, permafrost extends to a maximum depth of approximately 400 m, with a thin, peaty surface layer averaging less than 30 cm in thickness (Brown et al., 2003).

The coastal low-lying peatlands along the southern Baltic Sea are estimated to cover an area of approximately 0.16–0.2 km² (Fig. 1d). The offshore boundary of the former peatland roughly coincides with the offshore limit of a dynamic, coast-parallel longshore bar, with peat deposits eroded seaward. Globally, soft coastlines are increasingly affected by adverse processes such as erosion, flooding, and submergence. Sea level rise and climate change will further intensify the pressure on coastal urban areas and ecosystems, shaping their future development (Vestergaard, 1997; Furmanczyk and Dudzinska-Nowak, 2009). Ongoing coastal dynamic processes, such as wave and current induced erosion, sediment transport, and accumulation, have significantly influenced coastline evolution (Lehfeldt and Milbradt, 2000). These processes have led to coastline displacement through land loss or land reclamation, thereby altering the spatial extent of coastal ecosystems and habitats. Among the most vulnerable coastal areas are low-lying coastal wetlands, which face severe threats from saltwater intrusion, erosion, and submergence (Vestergaard, 1997; Nicholls and Cazenave, 2010; Wong et al., 2014). Along the Baltic Sea, approximately 1,800 km² of coastal wetlands are affected by saltwater intrusion (Sterr, 2008). In the southern Baltic Sea, coastal erosion has resulted in the loss of approximately 3 km of wetland in an eastward direction since the onset of peatland formation. This has led to peat layer exposure along the beach, where wave erosion occurs along the seaward margin of the wetland following the abrasion of overlying sand layers by storm events.

According to Chambers et al., 2019, the degradation of low-lying coastal wetlands is driven by stressors associated with global climate change and anthropogenic disturbance, leading to losses in both their health and spatial extent. Coastal wetlands are highly vulnerable to sea level rise, with projections estimating a 22–30% global areal loss by 2100 (Nicholls et al., 1999; IPCC, 2007). Occupying the intertidal ecotone between marine and terrestrial environments, coastal wetlands experience loss from multiple directions. On the seaward edge, storm events, increasing water depth, wave height, and wave power may accelerate erosion (Schwimmer, 2001; Mariotti and Fagherazzi, 2010), while drowning occurs when relative sea level rise outpaces soil surface elevation gains (Krauss et al., 2010). Additionally, steep topography and human infrastructure may restrict wetlands from migrating upslope, limiting their ability to maintain an optimal elevation relative to sea level. This constraint may result in habitat loss or conversion (Day et al., 2008; Hussein, 2009). Natural wetland degradation drivers include land subsidence, sea level rise, droughts, hurricanes, tsunamis, storms, erosion, and biological impacts (Dugan, 1993)

Malpica-Piñeros et al., 2024 reviewed research activities on Amazonian peatlands, which began with ecological studies in the 1950s. A substantial thematic expansion has been observed since 2009, initially focusing on carbon accumulation and greenhouse gas fluxes, and later shifting toward degradation and conservation after 2017. This trend has been accompanied

by a spatial bias favouring the Peruvian lowlands. To date, scientific attention remains limited for the peatlands of western Brazil, the Bolivian lowlands, and the Guianas. Most research on Amazonian peatlands has been conducted by international institutions, but recent years have seen a growing contribution from local research institutes and groups. Amazonia is home to the world's largest tropical rainforest and river system, containing 10% of global species diversity (Charity et al., 2016). Spanning nine countries in tropical South America, the Amazon Basin is primarily situated in Brazil (59%), with the remainder distributed across Bolivia (BOL), Colombia (COL), Ecuador (ECU), French Guiana (GUF), Guyana (GUY), Peru (PER), Suriname (SUR), and Venezuela (VEN) (Charity et al., 2016). High-altitude peatland landscapes in the Amazon Basin are found across three major regions: the lower Andean Cordillera, the Guiana Shield, and the Brazilian Shield, at elevations between 500 and 1500 m. In Guiana, beach erosion has been reported (Chevallier et al., 2023), indicating a potential for similar coastal processes in this study's context (Fig. 1e).

In boreal peatlands, gully formation due to fluvial erosion is a common process of blanket bog peatland erosion (Evans and Warburton, 2005). In addition to fluvial erosion, peatland failures in boreal peatlands are triggered by snowmelt, rainfall, drainage construction, and peat extraction. Peatland failures have been described using various terms, including peat landslides, bog bursts, and peat failures. However, in Dykes et al., 2007 classified previously documented peatland failures under the broader category of peat mass movements (Fig. 1f).

Numerous peatland failures have been reported in northern peatlands such as northern England and Ireland since the 16th century (Bowes et al., 1960; Crisp et al., 1964; Kirk et al., 2001; Mills et al., 2002; Warburton et al., 2004; Dykes et al., 2006; Boylan et al., 2008; Dykes et al., 2011). Peatland failures in northern peatlands are often triggered by heavy or prolonged rainfall (~90 mm in 90 min) (Dykes et al., 2007b). Most failures occur on thin (~2–3 m thick) blanket bog slopes, sometimes involving tens to hundreds of thousands of cubic meters of peat (Dykes et al., 2007). Reported consequences of peatland failures include mass fish kills in river systems (McCahon et al., 1987; Wilson et al., 1996) and disruptions to natural drainage systems (Alexander et al., 1986; Coxon et al., 1989). Peatland failures have been classified based on failure block morphology, soil composition, post-failure topography (e.g., secondary features such as tension cracks), failure mechanisms, peat mass displacement velocity, and moisture content of the failed slope (Dykes et al., 2007). According to this classification, peatland failures are categorized into bog burst, bog flow, bog slide, peat slide, peaty-debris slide, and peat flow (Dykes et al., 2007). According to Boylan et al., 2008, 70 peat slope failures have been reported in Ireland over the past 400 years, although the actual number of occurrences is believed to be significantly higher. Reported cases have increased since 1800, with some failures reaching volumes of up to 5,000,000 m³, although most are small-scale. A negative correlation between peat thickness and slope angle has been observed, with most failures occurring on slopes between 4° and 8°. However, failures can also occur on steeper slopes (>20°) if the peat layer is thinner, often involving interactions with the underlying mineral soil. Failure zones range from hundreds of meters to several kilometres, and larger failure volumes tend to result in longer peat mass displacement distances.

In tropical peatlands, reports of peat mass movements are significantly fewer compared to boreal peatlands. Aside from a recent case on Bengkalis Island (Yamamoto et al., 2019), the only previously documented instance was a suspected

peat landslide along the Tutoh River, Malaysia, in 1966 (Wilford, 1966) (Fig. 1h). On Bengkalis Island, coastal landslide has occurred that closely resemble bog bursts observed in boreal peatlands (Dykes et al., 2007). The residual landforms of these bog bursts exhibit crack patterns like those described in progressive failure, a mechanism well known in rock mass collapse, as defined by Djerrum, 1967.

240 These lateral degradation processes indicate the export of carbon reservoirs. Furthermore, lateral degradation in coastal areas signifies the export of terrestrial carbon reservoirs to marine environments. A significant portion of this carbon export to marine environments originates from riverine sources. Riverine carbon fluxes are the main source of terrestrial carbon exports into the ocean, with the annual global export of biogenic organic carbon through from 70 river systems (42.7×10^6 km²) estimated to be approximately 110–230 MtC (2.58 – 5.39 tC km⁻² yr⁻¹) (Galy et al., 2015). The Yellow River has the highest particulate organic carbon (POC) discharge in the world, with a discharge rate of approximately 14.678 tC km⁻² yr⁻¹ (Ludwig et al., 1996), for example. Although few studies have focused on the discharges of organic carbon from the erosion of organic-rich soils, including peatland, the export of POC to the ocean from these soils acts as a global carbon sink (Hilton et al., 2015).

245 The study by Hedges et al., 1986 demonstrated that most of the organic matter transported by the Amazon River consists of recently biospheric carbon (OC_{recent}) derived from lowland ecosystems. During riverine transport, the oxidation of this dissolved and particulate organic matter releases approximately 500 MtC yr⁻¹ into the atmosphere (Richey et al., 2002). Most of this oxidation originates from OC_{recent} and, therefore, does not have a significant impact on the long-term regulation of atmospheric CO₂ (Mayorga et al., 2005). Assuming that CO₂ is emitted from this POC, the resulting CO₂ emissions would correspond to approximately 25 times the total POC flux.

250 These coastal hazards contribute to lateral carbon transport, as peat particles are exported from coastal areas to the ocean. The ongoing export of peat material from tropical coastal peatlands due to coastal erosion and peat mass movements may have significant implications for the regional carbon budget, particularly if these exports act as a carbon sink in the marine environment. The objective of this study is to assess the extent of peatland degradation caused by coastal erosion and peat mass movement events and to quantify the amount of particulate organic carbon (POC) exported to the ocean due to these lateral degradation processes.

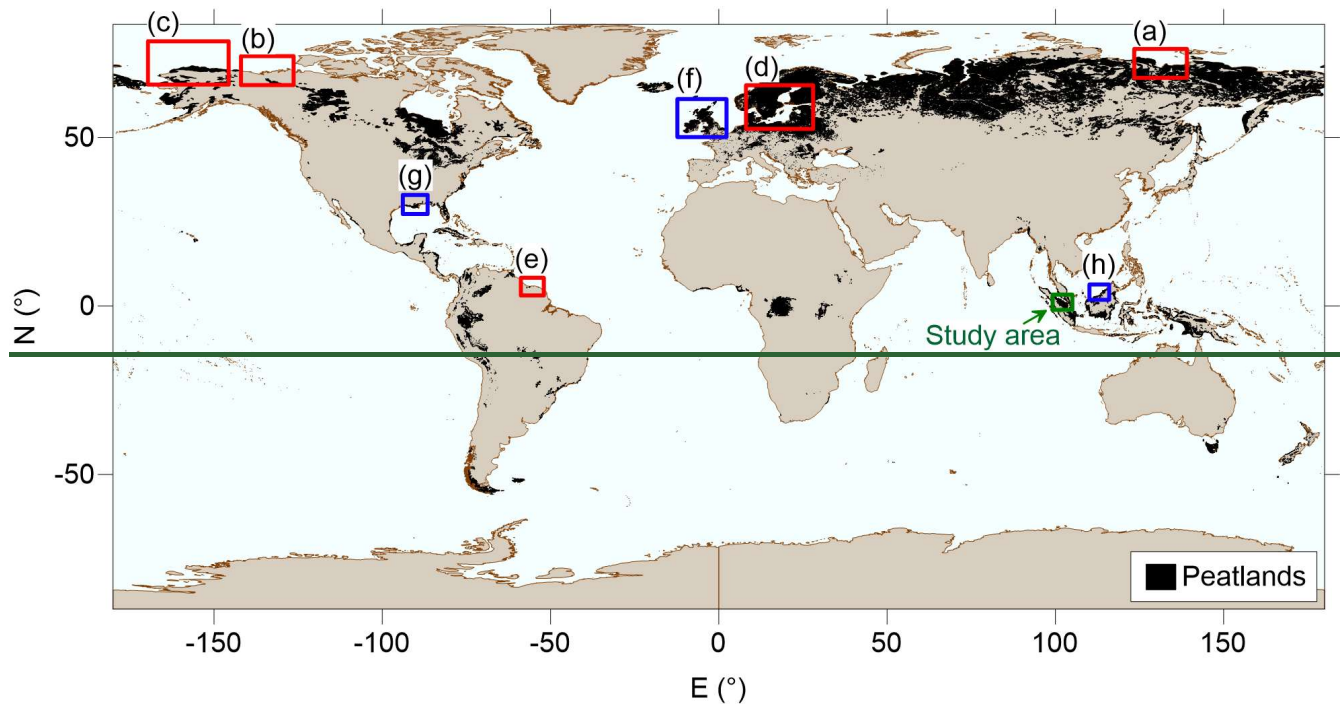


Figure 1: Global Distribution of Peatlands (Based on data from the Global Peatland Database / Greifswald Mire Centre (2024))

265 Peatlands are distributed across subarctic, Arctic, and tropical regions (Fig. A1). Peat, a partially decomposed organic material, accumulates under waterlogged and anoxic conditions, leading to the formation of extensive peatland ecosystems. Throughout the Holocene, peatlands have played a pivotal role in the global carbon cycle by serving as long-term carbon sinks. Globally, they have stored over 600 GtC at a sequestration rate exceeding 5 GtC per century (Kleinen et al., 2010; Yu, 2011). Despite covering only 3% of the Earth’s land surface, peatlands account for approximately 6% of the global soil carbon stock (Page et al., 2011; Scharlemann et al., 2014).

270 Tropical peatlands, primarily located in Southeast Asia, are broadly classified into inland and coastal types (Dommain et al., 2011). Coastal peatlands developed on marine clays and mangrove sediments following Holocene sea-level stabilization and are particularly extensive along the low-lying coasts of Sumatra and Borneo. In Sumatra, Riau Province alone contains more than 60% of the island’s coastal peatland area (Ritung et al., 2011). Although tropical peatlands represent only 11% of the global peatland area, they store more than 68.5 Gt of carbon—approximately 57.4 Gt of which is in Indonesia (Page et al., 2011). This disproportionately high carbon storage underscores their global importance.

275 However, these ecosystems are increasingly threatened by deforestation, drainage, and fire, which are transforming tropical peatlands from persistent carbon sinks into net sources of greenhouse gas emissions (Hooijer et al., 2010; Couwenberg et al., 2010). Table 1 summarizes reported values of carbon export from boreal and tropical peatlands, providing a comparative overview across climatic zones. Lateral degradations in boreal peatlands, such as gully erosion and peat failures, are known to

280

285 cause large-scale peat discharge (Evans and Lindsay, 2010; Boylan et al., 2008). The POC export flux associated with gully erosion has been reported as $3.09 \pm 0.1 \times 10^4$ gC km⁻² yr⁻¹ (Evans and Lindsay, 2010). In contrast, tropical coastal peatlands experience substantial peat loss driven by coastal erosion (Yamamoto et al., 2014). In contrast to fire-related emissions, physical degradation processes such as coastal erosion and peat mass movement events (PMMs) have been underrecognized as a pathway of carbon loss from peatland. Recent research has confirmed that tropical coastal peatlands are undergoing substantial degradation and loss due to coastal geomorphological processes, such as erosion retreat and peat bog burst. (Nabilah et al., 2024). Yet, this pathway remains unquantified, especially in contrast to the well-documented fluvial peat erosion processes in boreal and Arctic peatlands (Nabilah et al., 2024). The lack of long-term monitoring of coastal processes and the low number of reported failure events also contribute to this unresolved situation.

290 For example, on Bengkalis Island, the degradation of mangrove vegetation has left peat cliffs exposed to direct tidal and wave forces, leading to toppling failures, rotational slides, and cantilever collapses (Basir et al., 2023). These failures may represent a direct and measurable pathway for the export of particulate organic carbon (POC) to adjacent marine systems; however, the spatial extent and magnitude of this process remain poorly understood.

295 While lateral erosion and mass movements have been well studied in boreal and Arctic peatlands, distinct mechanisms are observed in those regions. For example, erosion along the Bykovsky Peninsula in Siberia is driven by thawing of ice-rich permafrost and storm surges, with buried Holocene peat and ice wedges commonly found in the stratigraphy (Lantuit et al., 2011). Similarly, Arctic coasts in Alaska experience cryogenic processes influenced by permafrost degradation, brackish water, and short ice-free seasons.

300 In the southern Baltic Sea region, another contrasting model is observed, where Holocene sea-level rise and wave-induced abrasion have eroded glacially derived peat layers overlying lacustrine and glacial till sediments (Furmanczyk and Dudzińska-Nowak, 2009). In the British Isles, raised and blanket bogs—shallow, ombrotrophic peatlands reliant on precipitation—frequently exhibit failure modes such as bog bursts and bog flows (Dykes and Warburton, 2007; Boylan et al., 2008). For example, coastal landslides on Bengkalis Island have closely resembled bog bursts reported in boreal regions (Yamamoto et al., 2019), and the residual landforms display crack patterns characteristic of progressive failure—a mechanism well established in rock mass collapse (Bjerrum, 1967). However, the landscape of the failure site differs fundamentally, occurring in coastal lowlands rather than upland terrain typical of boreal peatlands. Documented events—such as the peat landslide on Bengkalis Island (Yamamoto et al., 2019) and the 1966 failure in Malaysia (Wilford, 1966)—suggest that tropical PMMs may share morphological features with boreal failures yet arise under distinctly different hydrological and hydraulic regimes. Despite these differences, the implications for carbon cycling may be broadly comparable.

310 Global POC export from riverine systems is estimated at 110–230 MtC yr⁻¹ (Galy et al., 2015). Meanwhile, erosion of organic-rich soils—including peat—has increasingly been recognized as a major contributor to the marine carbon budget (Hilton et al., 2015). Particularly in tropical coastal zones, the direct mobilization of peat-derived POC into adjacent seas may represent an underrecognized component of land-to-ocean carbon flux. If ultimately buried in marine sediments, this exported material could function as a long-term carbon sink.

315 [This study focuses on Bengkalis Island as a representative system of tropical coastal peatland degradation. We](#)
[investigate geomorphic changes associated with coastal erosion and PMMs, with the goal of quantifying the resulting export](#)
[of POC. By situating these findings within a broader biogeographic and geoclimatic context, this study addresses a critical gap](#)
[in our understanding of the role of tropical coastal peatlands in global carbon cycling. To support this analysis, we employ a](#)
[conceptual model \(Figs. 1 and 2\) that integrates coastal erosion processes and PMMs.](#)

320

325

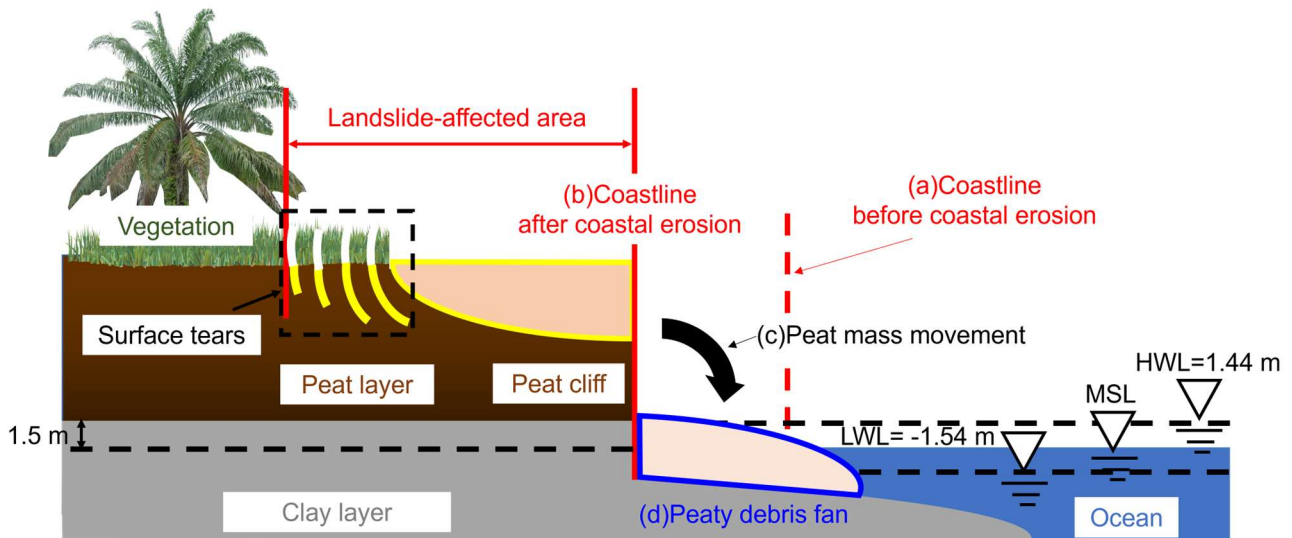
330

Table 1: Comparison of carbon export studies in Boreal and Tropical peatlands.

Location	Cause	Species	Peat volume (m ³)	Flux (kgC km ⁻² yr ⁻¹)	CO ₂ emission (μgC gC ⁻¹ h ⁻¹)	Load (TgC yr ⁻¹)	Note	Reference	
Northern England	Peat Erosion								
	a) Gully Erosion	POC	1.63 × 10 ⁷	3.09±0.1 × 10 ⁴	-	-	-	Evans and Lindsay, 2010.	
		DOC	-	2.75 × 10 ⁴	-	-	-	Pawson et al., 2012.	
	b) Fluvial Erosion	POC	-	8.75 × 10 ²	-	-	-	Pawson et al., 2007.	
UK		DOC	-	1.99±5.77 × 10 ⁻²	-	-	-		
Boreal peatlands	Ireland	Peat failures	Peat soil	5.00 × 10 ⁶	-	-	In 1900	Boylan et al., 2008.	
	Arctic Circle	Wild Fire	CO ₂	-	1.74 × 10 ⁶	-	-	Witze, 2020.	
Netherlands	Decomposition								
	a) Aerobic Decomposition		-	-	1.09	-	t=24 hours		
		CO ₂	-	-	3.09	-	t=15 weeks	Tolunay et al., 2024.	
	b) Anaerobic Decomposition		-	-	0.78	-	t=24 hours		
			-	-	0.42	-	t=15 weeks		
Tropical peatlands	Coastal Erosion		Peat soil	3.90 × 10 ⁷	-	-	1998-2013	Yamamoto et al., 2014.	
	Fluvial Carbon Export		DOC	-	-	-	0.3	Baum et al., 2007.	
	Indonesia	Peat Fire	CO ₂	-	4.25 × 10 ⁵ -1.35 × 10 ⁶	-	-	-	Page et al., 2002.
				-	6.02 × 10 ⁻¹	-	-	In 2002	
		Oxidative Decomposition	CO ₂	-	3.82 × 10 ⁻¹	-	-	In 2003	Hirano et al., 2007.
		-	3.13 × 10 ⁻¹	-	-	In 2004			
		-	3.28±2.04 × 10 ⁻¹	-	-	-	Hirano et al., 2012.		



335 **Figure 12:** Example of lateral degradations in tropical coastal peatland. (a) Coastal erosion (Rangsang Island, Indonesia); (b) Peat mass movement events (Bengkalis Island, Indonesia); (c) Situation where peat is discharged into the ocean due to lateral degradations (Bengkalis Island, Indonesia).

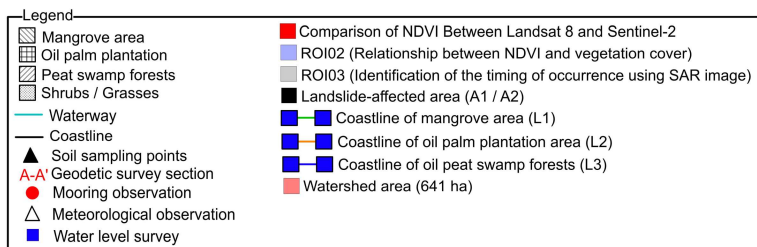
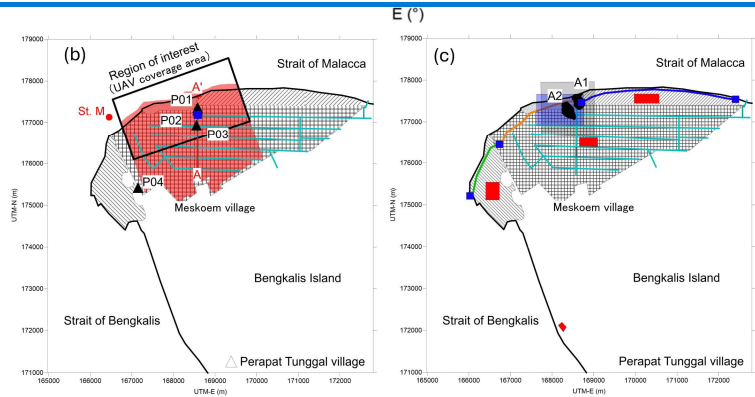
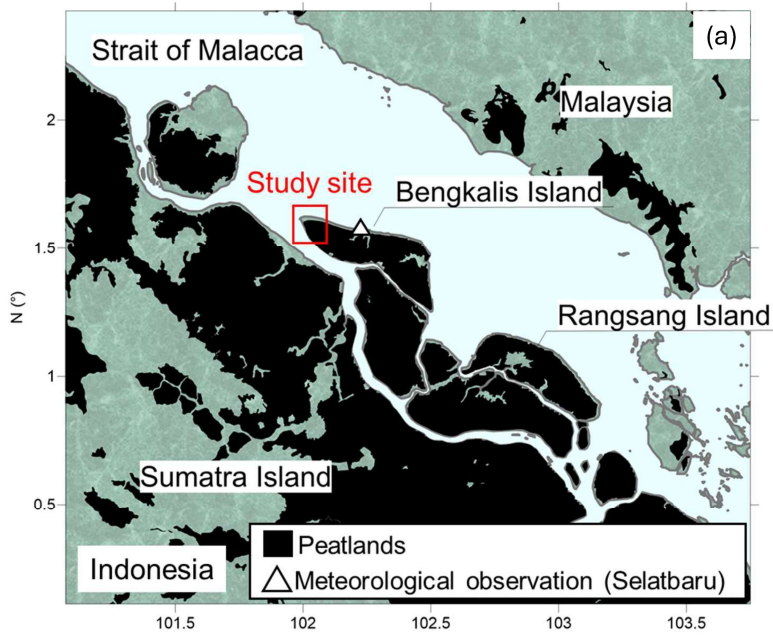


340 **Figure 23:** Conceptual figure of coastal erosion and PMMs on the peatland coast. Where the **High Water High-Water** Level (HWL) is 1.44 m, the Mean Sea Level (MSL) is 0 m, and the Low Water Level (LWL) is -1.54 m. (a)~(d) show the transitional changes in the coastal landform and a cross-section of the coast. (a) coastline before coastal erosion; (b) coastline after coastal erosion; (c) trace of where PMM occurred; and (d) peaty debris fan formed by peat overhanging the coastline due to the occurrence of PMMs. When PMMs occur, cracks through the peat layer, known as surface tears, appear in the hinterland. In this study, the area affected by the
345 landslide was defined as the hinterland from the peaty debris fan to the head of the source of surface tears. Landslide-affected areas have a thinner vegetation cover.

2 Study area

Bengkalis Island in Riau Province, Indonesia, is a tropical coastal peatland island that encompasses the Straits of Malacca and Bengkalis located 1.6 ° North and 102 ° East, covering an area of approximately 900 km² (Fig. 34). Local observations from 2015 to 2018 recorded annual precipitation ranging from 1,381 mm to 2,402 mm. With peat accumulation dating back 5,000 to 6,000 years, the island is characterised by its flat topography and is composed primarily of five peat domes, reaching a maximum elevation between 10 and 15 m above sea level (Supardi et al., 1993). Since 1988, land use trends on the island have changed considerably. In 2019, oil palm plantations had expanded to cover 31.12 % of the island's total area, accompanied by the construction of waterways designed to transport oil palm fruit bunches (Umarhadi et al., 2022).

Currently, the northwest area of Bengkalis Island is experiencing considerable coastal erosion. The coastline gradually approached the highest area of the peat dome on northwest Bengkalis Island. Satellite imagery analysis from 22 December 1988 to 18 July 2013, revealed a coastal erosion rate of approximately 34 m yr⁻¹ (Kagawa et al., 2017). Maps created by the U.S. Army Map Service in 1955 documented the presence of mangrove belts on all northern coasts. However, these mangrove belts cover only a limited area of the northwest coast, revealing the erasure of inland peatland forests facing the sea and the formation of approximately 6 m tall peat cliffs. Furthermore, the island experienced an average subsidence rate of 2.646±1.839 cm yr⁻¹ between 2018 and 2019, with the northwestern part recording significant subsidence rates of up to 17.416 cm yr⁻¹ due to peat bursts (Umarhadi et al., 2022).



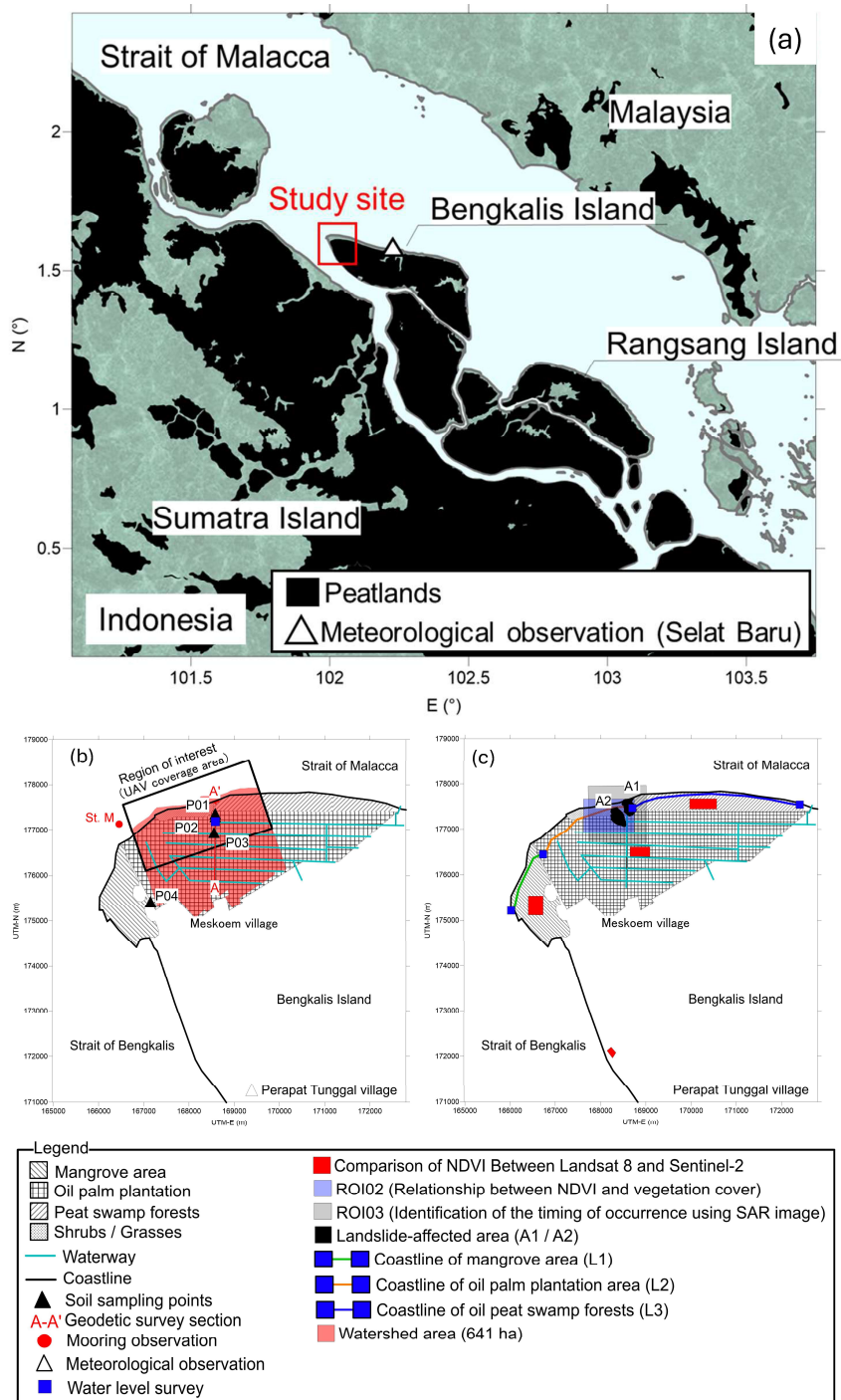


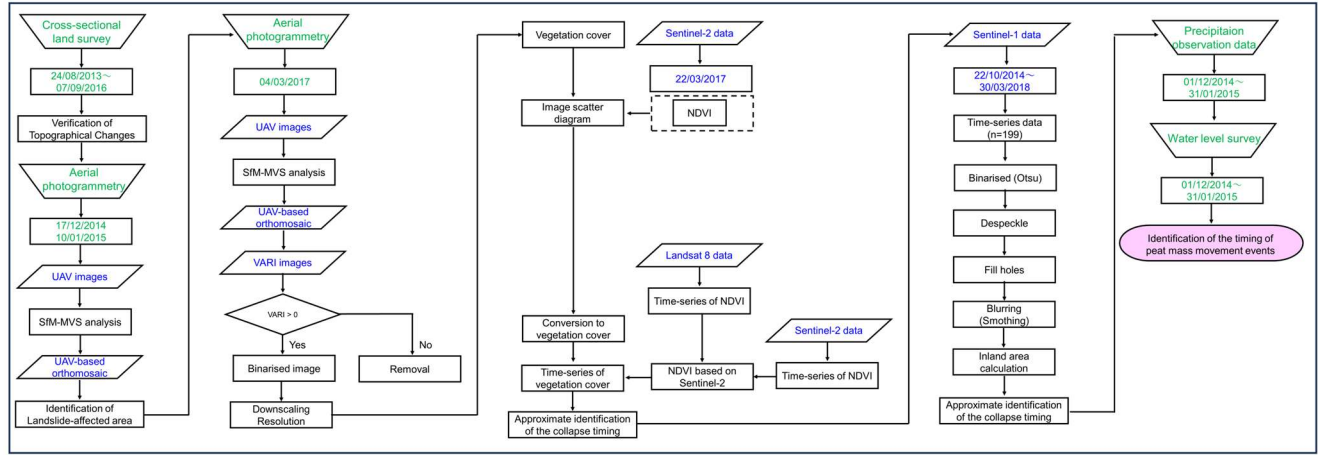
Figure 34: Location of the study site (northwest coast of Bengkalis Island). The peat area is delineated referring to Xu et al., 2017. The northern coast of the island is the area eroded by coastal erosion. The classification of land use is based on field observation.

370 **3 Materials and Methods**

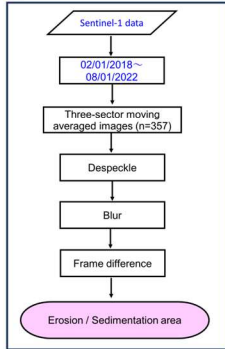
The methodology of this study consists of (Fig. 45): (a) To clarify the actual state of PMMs, we identified the timing of their occurrence, (b) To clarify the actual state of coastal erosion, we estimated the coastline retreat, (c) estimation of barren land area using machine classification satellite images, (d) modification of the digital surface model (DSM) to a digital terrain model (DTM), (e) estimation of the POC from the displacement of peat mass caused by PMMs using field surveys and satellite image analyses, and (f) estimation of the POC flux due to coastal erosion using field survey and satellite image analysis. And the meanings of the abbreviations appearing in this study are given in Table 24 and Fig. 56. In this study, multispectral and panchromatic satellite imagery, aerial photogrammetry, DSM data, cross-sectional land surveys and soil sampling were used to assess coastal and peatland degradation. Table 23 lists the images used in this study. Combining the above steps in Sections 3.2.1 through 3.2.6 yields the overall workflow depicted in Fig. 4.

380

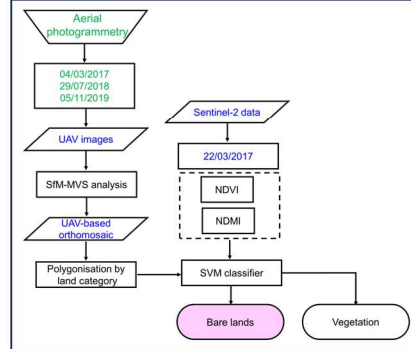
(a) Identification of the timing of peat mass movement events



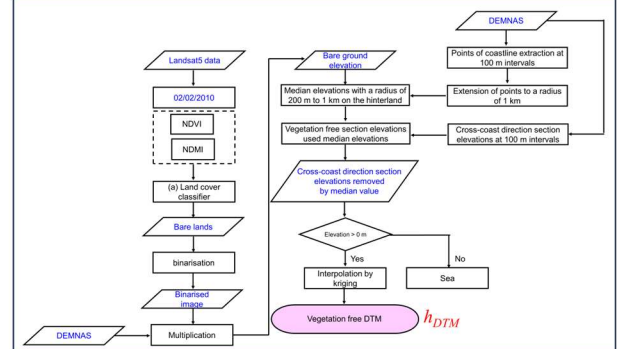
(b) Estimation of coastal retreat



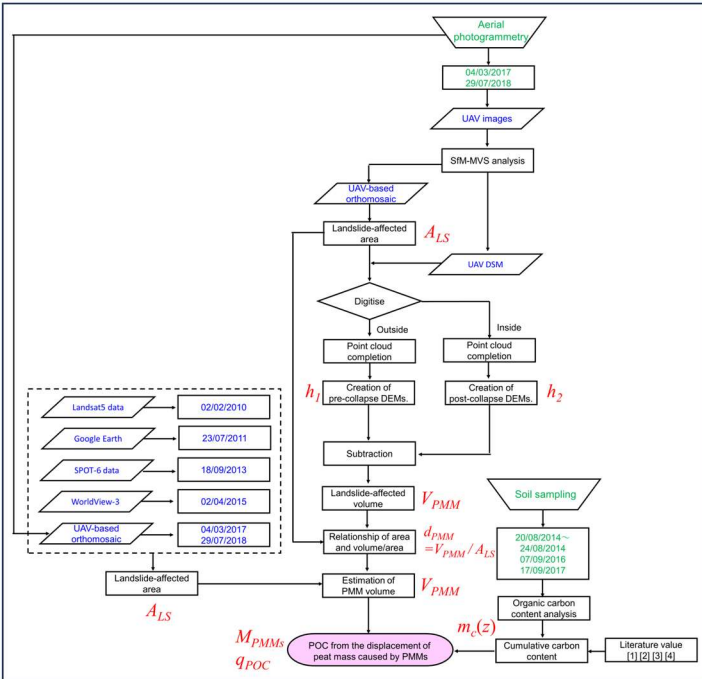
(c) Land cover classification



(d) DTM created from DEMNAS



(e) Estimation of the POC from the displacement of peat mass caused by PMMs



(f) Estimation of POC flux into ocean due to coastal erosion

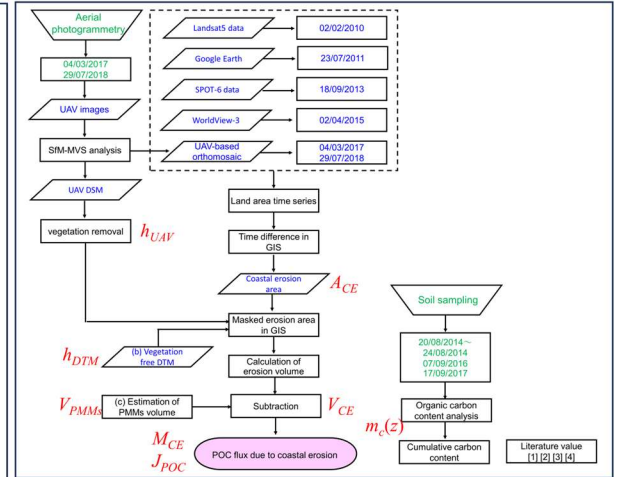


Figure 45: Flow chart used in this study for field surveys and satellite image analysis; (a) To clarify the actual state of PMMs, we identified the timing of their occurrence; (b) To clarify the actual state of coastal erosion, we estimated coastline retreat; (c) an estimation of barren land area by machine classification satellite imaging; (d) the modification of a digital surface model (DSM) to a digital terrain model (DTM).). Abbreviations used: h_{DTM} – Elevation of DTM; (e) and estimation of POC from displacement of peat mass caused by PMMs. Abbreviations used: A_{LS} – Landslide-affected area, h_1 – Elevation before landslide, h_2 – Elevation after landslide, V_{PMM} – Peat mass movement volume, d_{PMM} – Depth of affected by landslide, $m_c(z)$ – Carbon stocks, M_{PMMs} – Mass of POC due to PMMs, q_{POC} – POC fluxes to ocean due to PMMs; (f) an estimation of the POC flux due to coastal erosion; Literature values [1] [2] [3] [4] sourced from Wahyunto et al., 2003; Dariah et al., 2012; Warren et al., 2012 and Rudiyanto et al., 2018. Abbreviations used: h_{UAV} – Elevation of DSM from UAV photogrammetry, A_{CE} – Coastal erosion area, h_{DTM} – Elevation of DTM, V_{PMMs} – Peat mass movements volume, V_{CE} – Coastal erosion volume, $m_c(z)$ – Carbon stocks, M_{CE} – Mass of POC due to coastal erosion, J_{POC} – POC fluxes to ocean due to coastal erosion.

Table 42: Glossary and abbreviations.

Abbreviation	Term	Brief Description
PMM	Peat mass movement	The abbreviation for the term "peat mass movement," which refers to a phenomenon where the ground suddenly collapses and causes landslides due to heavy rainfall or other factors. The areas affected by landslides are characterised by cracks in the surface and peat layers, known as surface tears, which are secondary features located at the head of the landslide zone.
V_{PMM}	Peat mass movement volume	The volume of peat exported to the ocean as a result of a peat mass movement (PMM) event. The loss of the peat volume by a PMM event.
A_{LS}	Landslide-affected area	An area affected by a PMM event, including regions where surface tears, a secondary feature of the collapse, are present.
h_1	Elevation before landslide	The elevation before being affected by a PMM event.
h_2	Elevation after landslide	The elevation after being affected by a PMM event.
V_{PMMs}	Peat mass movements volume	The total volume of peat exported to the ocean as a result of peat mass movement (PMM) events.
V_{CE}	Coastal erosion volume	The total volume of peat exported to the ocean as a result of coastal erosion.
A_{CE}	Coastal erosion area	The area lost as a result of coastal erosion.
h	Elevation of ground before lateral degradation	The elevation before being affected by lateral degradations.
h_B	Thickness of the clay base layer	The thickness of the clay layer, which forms the base layer of peatland coasts.
d_{PMM}	Depth of affected by landslide	The average decline of the elevation by a PMM event, synonymous with V_{PMM} / A_{LS} in this study.
h_{DTM}	Elevation of DTM	The elevation of the ground before coastal erosion and PMMs, specifically the DTM elevation, which is derived from the DEMNAS data.
h_{UAV}	Elevation of DSM from UAV photogrammetry	The elevation of the DSM obtained from UAV photogrammetry, with tree height removed.
z	Peat layer depth from the surface ground	The depth of the peat layer from the surface of the ground in peatland coasts.
$m_c(z)$	Carbon stocks	Carbon stocks as a function of peat depth in peatland coasts.
ρ_d	Dry density of peat	Dry density as a function of peat depth in peatland coasts.
a_c	Organic carbon content of peat	Organic carbon as a function of peat depth in peatland coasts.
M_{PMM}	Mass of POC due to PMM	The mass of particulate organic carbon (POC) exported to the ocean as a result of a PMM event.
M_{PMMs}	Mass of POC due to PMMs	The mass of particulate organic carbon (POC) exported to the ocean as a result of PMM events.
M_{CE}	Mass of POC due to coastal erosion	The mass of particulate organic carbon (POC) exported to the ocean as a result of coastal erosion.
l	Coastline distance	Coastline distance in the region of interest for each period.
q_{POC}	POC fluxes to ocean due to PMMs	The particulate organic carbon (POC) from the displacement of peat mass caused by PMMs.
J_{POC}	POC fluxes to ocean due to coastal erosion	The particulate organic carbon (POC) fluxes to the ocean due to coastal erosion.
V_{PMM} / A_{LS}	Depth of affected by landslide	The average decline of the elevation by a PMM event, synonymous with d_{PMM} in this study.

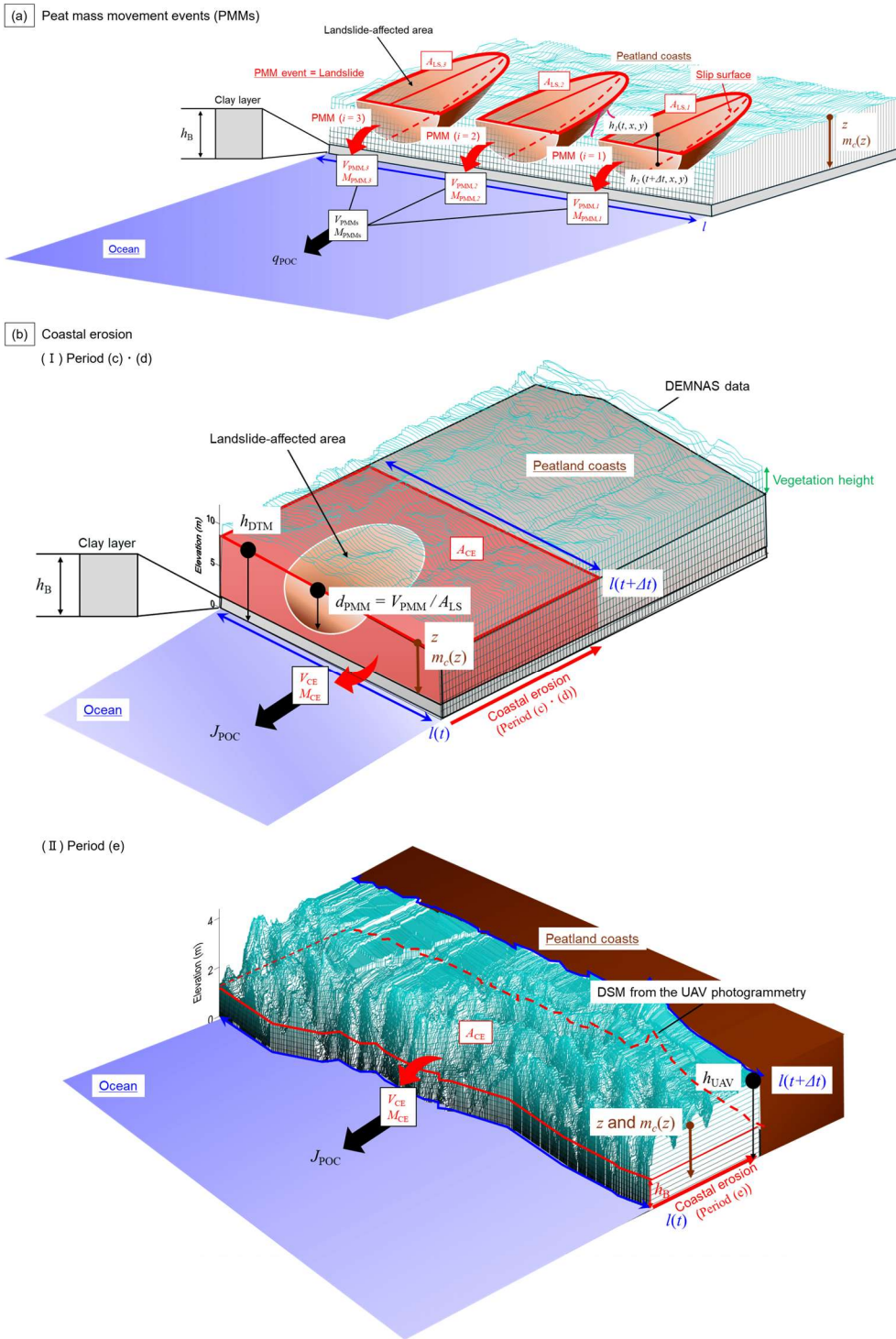


Figure 65: Illustrative image of abbreviations. (a) Model of abbreviations associated with peat mass movement events; (b) Model of abbreviations associated with coastal erosion.

Table 23: Remote sensing data used in this study. Satellite imagery data was used in addition to UAV-based orthomosaic and DSM from the aerial photogrammetry results of the field survey.

Image acquisition	Data source	Resolution (m)	Bands used
22/10/2014~ 30/03/2018 05/01/2018~ 08/01/2022	Sentinel-1	5×20	C-band
17/12/2014 10/01/2015 5/3/2016 04/03/2017 29/07/2018 5/11/2019	UAV-based orthomosaic	0.494 0.1 0.086 0.285 1 0.5	- - - - - -
02/02/2010 23/07/2011 18/09/2013 02/04/2015 09/03/2017 03/10/2017~ 19/02/2022 22/03/2017 03/10/2017~ 19/02/2022	Landsat5 Google Earth SPOT-6 WorldView-3 Landsat8 Sentinel-2	30 - 6 1.24 30 10	Red/Green/Blue/NIR/SWIR1 Panchromatic Red/Green/Blue Red/Green/Blue Red/Green/Blue/NIR Red/NIR/SWIR1
04/03/2017 29/07/2018 2013	UAV DSM DEMNAS	0.285 1 8	- - X-band/L-band

405 3.1 Materials

3.1.1 WorldView satellite data and Google Earth image

To identify areas of coastal erosion and PMMs, Google Earth images captured on 23 July 2011 and WorldView-3 multispectral data from 2 April 2015, were used. Launched on 13 August 2014, WorldView-3 operated from a circular sun-synchronous orbit at an altitude of 617 km. WorldView-3 provides eight bands of multispectral data at resolutions of 1.24 (nadir) and 1.38
410 m (20° off-nadir), and hence a revisit frequency of 4.5 days. Both sensors in the WorldView constellation provide high-resolution Earth observation imagery.

3.1.2 Landsat data

In this study, multispectral Landsat series images, including Landsat 5 Thematic Mapper (TM) and Landsat 8 Operational Land Imager (OLI), were used. Landsat 5 TM images captured on 2 February 2010 were used to delineate coastal erosion and

415 areas affected by landslides. Additionally, Landsat 5 TM imagery was used to extract bare lands. Landsat 5 TM was launched
in March 1984 and carries a Multispectral Scanner Subsystem (MSS) and a TM onboard (USGS and NOAA, 1984). TM has
improved the spectral, radiometric, and spatial resolutions relative to MSS. Landsat 8 OLI images from 9 March 2017 to 19
February 2022 were used. Landsat 8 was launched in 2013 and provides high-quality multispectral images at a resolution of
30 m and a revisiting time of 16 days. It aims to provide data continuity to the Landsat Earth observation program, started in
420 the 1970s. These Landsat series data were downloaded from the USGS EarthExplorer (<https://earthexplorer.usgs.gov/>), and
the cloud cover in the collected images was 0%.

3.1.3 Sentinel-1 data

For the identification of the timing of PMM occurrence, Sentinel-1 data acquired from 22 October 2014 to 30 March 2018
were used. In addition, for the estimation of coastal retreat, Sentinel-1 data collected from 5 January 2018 to 8 January 2022
425 were employed. Sentinel-1 is a constellation of two radar imaging satellites that are part of the European Union's Copernicus
Programme. Equipped with C-band synthetic aperture radar (SAR) sensors, Sentinel-1 can capture high-resolution images of
the Earth's surface regardless of weather conditions or lighting, making it ideal for continuous monitoring. In its Interferometric
Wide swath mode, it offers a resolution of approximately 5×20 m. Its data are used for a variety of applications, including land
and ocean monitoring, disaster management, and environmental observation. Data were obtained from USGS EarthExplorer
430 (<https://earthexplorer.usgs.gov/>).

3.1.4 Sentinel-2 data

Sentinel-2 multispectral imagery captured on 22 March 2017, was used for land cover classification. Sentinel-2B provides 13
bands of multispectral imaging at a resolution of 10 m. Sentinel-2B was launched on 7 March 2017. Part of a European fleet
of satellites aimed at delivering core data to the European Commission's Copernicus programme, a programme whose services
435 address six thematic areas: land, marine, atmospheric, climate change, emergency management, and security. In a sun-
synchronous orbit at a mean altitude of 786 km above the Earth's surface, MSI samples 13 spectral bands in the visible-near
infrared (VNIR) and short-wave infrared (SWIR) spectral range at three different spatial resolutions (10, 20, and 60 m) and
allows for a 290 km swath width with a high revisit frequency of 10 days. Data were obtained from USGS EarthExplorer
(<https://earthexplorer.usgs.gov/>).

440 3.1.4.5 SPOT-6 data

To elucidate the evolution of PMMs due to coastal erosion, SPOT-6 data captured on 18 September 2013, were used. SPOT-
6 provides high-resolution optical images with a resolution of 6 m in multispectral bands. SPOT-6 was launched on 9,
September 2012. The satellite is in a nearly circular, sun-synchronous orbit with a period of 98.97 minutes at an altitude of
approximately 694 km. SPOT-6 acquires 12-bit data in five spectral bands: blue, green, red, panchromatic, and near-infrared.

445 **3.1.56 DEMNAS (National Digital Elevation Model in Indonesia)**

The National Digital Elevation Model in Indonesia (DEMNAS) is a digital surface model (DSM) that was used to create a vegetation-free DTM for the coastal zone in this study. DEMNAS is the result of interpolation from multiple data sources such as IFSAR, TERRASAR-X and ALOS PALSAR at 5 m, 5 m, and 11.25 m resolutions, respectively, with the addition of [stereoplottedstereo plotted](#) mass point data in the calculation (EGM2008 vertical datum).

450 **3.1.67 Aerial photogrammetry**

To investigate coastal erosion and PMMs, an unmanned aerial vehicle (UAV) was used for aerial photogrammetry. Fig. 34 shows the areas of interest. Table 34 lists the survey schedules, and the equipment used in this study. For photogrammetry, ground control points (GCPs) were established and geolocated using static GNSS measurements (5700/5800, Trimble, USA) or RTK-GNSS (GRX2, Sokkia, Japan). Commercially available software (Photoscan Professional, Agisoft, Russia) was used
455 to process the resulting images for SfM-MVS analysis to create a DSM.

Table 34: Geodetic and aerial photogrammetry survey schedule and equipment.

Year	Month	Geodetic survey	Total length (m)	Aerial photogrammetry survey	Total Area (ha)	Camera
2013	8	✓	740		-	-
2014	3	✓	469		-	-
2014	8	✓	497		-	-
2014	12		-	✓	21	DSLR
2015	1	✓	512	✓	91	DSLR
2015	8	✓	421		-	-
2015	11	✓	304		-	-
2016	3		-	✓	68	DSC
2016	9	✓	399		-	-
2017	3		-	✓	408	DJI Phantom4
2018	7		-	✓	220	DJI Phantom4
2019	11		-	✓	214	DJI Phantom4

460 **3.1.78 Cross-sectional land survey**

To examine changes in the cross-sectional profile of the land, particularly in the plantation in Meskom Village, a survey was carried out along a north–south transect (Section A-A’). Fig. 34 displays the transect and Table 34 lists the survey schedules. A Sokkia GRX2 RTK-GNSS system based on reference points located in the Bengkalis state polytechnic was used to perform the measurements.

465 **3.1.89 Sampling and analysis of peat soils**

Soil sampling was performed to determine the organic carbon content of the peat soil. Fig. 34 shows the sampling points and Table 45 lists the sampling and analysis information. A Dutch-style peat sampler (DIK-105A, Daiki Rika Kogyo Co., Ltd.,

Saitama, Japan) was used to extract samples up to 6 m below the clay layer. Quantitative sampling was performed to measure the density at the time of collection. The samples were dried at 105 ° C and the organic carbon and nitrogen content was analysed using a CHN analyser (JM-10 analyser, J-Science Lab., Kyoto, Japan).

Table 45: Details of the sampling and analysis of peat soil.

No.	Coordinates		Date	Depth (cm)	Layers (50 cm)	Land use	Analysis items
	Latitude	Longitude					
P01	1.6019°N	102.0218°E	20 - 24/08/2014	600	12	Oil palm plantation	Moisture content, Dry density, Carbon content
P02	1.6025°N	102.0218°E	20 - 24/08/2014	600	12	Oil palm plantation	Moisture content, Dry density, Carbon content
P03	1.5987°N	102.0216°E	17/09/2017	167	4	Oil palm plantation	Moisture content, Dry density, Carbon content
P04	1.5849°N	102.0090°E	07/09/2016	294	6	Oil palm plantation	Moisture content, Dry density, Carbon content

3.1.910 Mooring observations

From 4 November 2019 to 13 January 2020, a pressure-type memory wave gauge (INFINITY-CTW) was moored approximately 500 m offshore from a coast undergoing significant erosion to measure wave heights from the temporal variation in pressure (Fig. 34 St.M). Based on these measurements, significant wave heights were calculated for every two-hour interval.

3.1.101 Meteorological observations

To elucidate the temporal characteristics of PMMs occurrences and the features of coastal erosion, meteorological observation instruments were installed at Selat bBaru and Perapat Tunggal on Bengkalisunkaris Island (Fig. 34), and measurements were conducted. The instruments used were the SESAME II-05d (Midori Engineering Institute). This study utilized data collected from 2014 to 2021.

3.1.112 Water level survey

To investigate changes in water levels within channels in areas where peat collapse occurs frequently, a water level gauge was installed at the location shown in Fig. 34. A monitoring well was constructed at the measurement site using a polyvinyl chloride (PVC) pipe, and the channel water level was recorded using a HOBO U-20 water level logger. This study utilized data collected from 1 December 2014 to 31 January 2015.

3.2 Methods

3.2.1 Identification of the timing of PMM occurrence

[Time-series NDVI \(Normalized Difference Vegetation Index\) data were analysed using the Sentinel Hub EO Browser, with average NDVI values calculated within predefined polygons across a specified temporal range to evaluate vegetation dynamics](#)

(see Appendix B for details). The relationship between NDVI and vegetation cover was also examined, demonstrating a strong correlation between NDVI values obtained from Sentinel-2 and Landsat 8 imagery (Appendix C). These analyses provide a robust framework for detecting vegetation changes and estimating the timing of peat mass movements (PMMs). In particular, the occurrence of PMMs is often preceded by the formation of surface tears—cracks that appear on the ground surface—leading to a localized decline in vegetation cover. This characteristic reduction in NDVI serves as a key indicator of the onset of PMMs. Appendix B describes the methodology used to analyze time-series NDVI (Normalized Difference Vegetation Index) data via the Sentinel Hub EO Browser. Average NDVI values were computed within designated polygons over a defined temporal range to evaluate vegetation dynamics. Appendix C further investigates the relationship between NDVI and vegetation cover, demonstrating a strong correlation between NDVI data derived from Sentinel 2 and Landsat 8 imagery. These analyses provide a robust framework for detecting vegetation changes and estimating the timing of PMMs. In particular, the occurrence of PMMs is often accompanied by the formation of surface tears—cracks that appear on the ground surface—leading to a localized decline in vegetation cover. This characteristic NDVI reduction serves as a key indicator for identifying the onset of PMMs.

Time-series changes in NDVI were analyzed using Landsat8, while Sentinel-2 imagery was employed to examine the relationship between NDVI and vegetation cover. Consequently, we first established the relationship between NDVI values from Landsat8 and Sentinel-2. An oil palm plantation was selected as the target for comparison (Fig. 4c). To determine whether NDVI variation is related to vegetation coverage, VARI (Visible Atmospherically Resistant Index) images were generated from UAV aerial photogrammetric data acquired on 4 March 2017. The VARI images were binarized using a threshold of 0, and a scatter diagram was constructed to compare the binarized VARI values with the NDVI data. Pixel sizes were matched to facilitate the correlation analysis between vegetation coverage and NDVI. NDVI (Landsat 8), NDVI (Sentinel-2) and VARI were calculated using Eq. (1), Eq. (2) and Eq. (3).

$$NDVI = (B5 - B4) / (B5 + B4) \quad (1)$$

$$NDVI = (B8 - B4) / (B8 + B4) \quad (2)$$

$$VARI = (G - R) / (G + R - B) \quad (3)$$

Where $B5$ represents the NIR with 30 m resolution (wavelength: 850-880 nm); $B4$ represents the red band with 30 m resolution (wavelength: 640-670 nm); $B8$ represents the NIR with 10 m resolution (wavelength: 842 nm); $B4$ represents the red band with 10 m resolution (wavelength: 665 nm). G represents the green band; R represents the red band; B represents the blue band.

3.2.3 Identification of the timing of PMM occurrence using SAR image

Changes in the land area within the landslide-affected areas were analysed using Sentinel-1 SAR images acquired between 22 October 2014 and 30 March 2018. The time-series data were downloaded as an animated GIF from the EO Browser, and the region of interest is shown in Fig. 43. The image analysis procedure involved applying a moving average over

three consecutive acquisition intervals and smoothing the coastline using a blurring technique. Subsequently, noise within the region of interest was removed. After blurring, the images were binarized to isolate the land areas, thereby revealing changes in the extracted region. The expansion of this area a characteristic feature of peaty debris fans occurs following peat mass movement events.

3.2.24 Estimation of coastal retreat using SAR image

Using 359 Sentinel-1 SAR images acquired from 5 January 2018 to 8 January 2022, the average cumulative coastline retreat was calculated for each land cover type namely, the mangrove belt, oil palm plantation, and peat swamp forest. The specific coastlines corresponding to these land cover types are shown in Fig. 43, and the analytical workflow is illustrated in Fig. 54.

The analysis procedure was as follows. First, a moving average was applied over three consecutive acquisition intervals (including the day before and after each image) to smooth the data. Next, the coastline and land areas were separated by binarization. Noise reduction was then performed, and the difference between consecutive images was computed to extract the regions undergoing coastline changes. The area of these regions was calculated, and by dividing the computed area by the corresponding coastline length for each land cover type, the average coastline retreat was determined.

For 2018 and 2021, local observations (Fig. 34) of precipitation and wind speed were summarized as annual precipitation and annual maximum wind speed. Furthermore, the relationship between significant wave height and maximum wind speed was examined for the period from 4 November 2019 to 13 January 2020 using data from mooring observations. In analysing maximum wind speed, data recorded at Selat bBaru were used; since the moored observation points differed, a moving average covering two hours before and after each observation was applied to better represent the relationship between significant wave height and maximum wind speed.

Additionally, annual wind roses were generated using 10-minute interval observations of maximum wind speed and direction recorded at Selat bBaru and Perapat Tunggal in 2018 and 2021. These combined meteorological and remote sensing analyses allowed for a comprehensive discussion of coastal erosion characteristics across different land cover types.

3.2.5 Land cover classification using machine learning

~~To extract bare land from oil palm plantations in satellite images, we used the normalised difference vegetation index (NDVI) and the normalised difference moisture index (NDMI) derived from Sentinel 2 imagery to classify the land cover. NDVI and NDMI were calculated using Eq. (2) and Eq. (4), respectively. For machine learning, Support Vector Machine (SVM) algorithms were used to classify the oil palm tree plantations from the other landcovers. The UAV images, taken on 4 March 2017, 29 July 2018, and 5 November 2019, were used as the ground truth of the land cover. The precision of the land cover classification was evaluated by calculating the true positive rate, recall, specificity, precision, negative predictive value and F-score based on the confusion matrix. The dividing lines were calculated with palm oil plantation vegetation as true positives (TP) and other types of land cover as false negatives (FN):~~

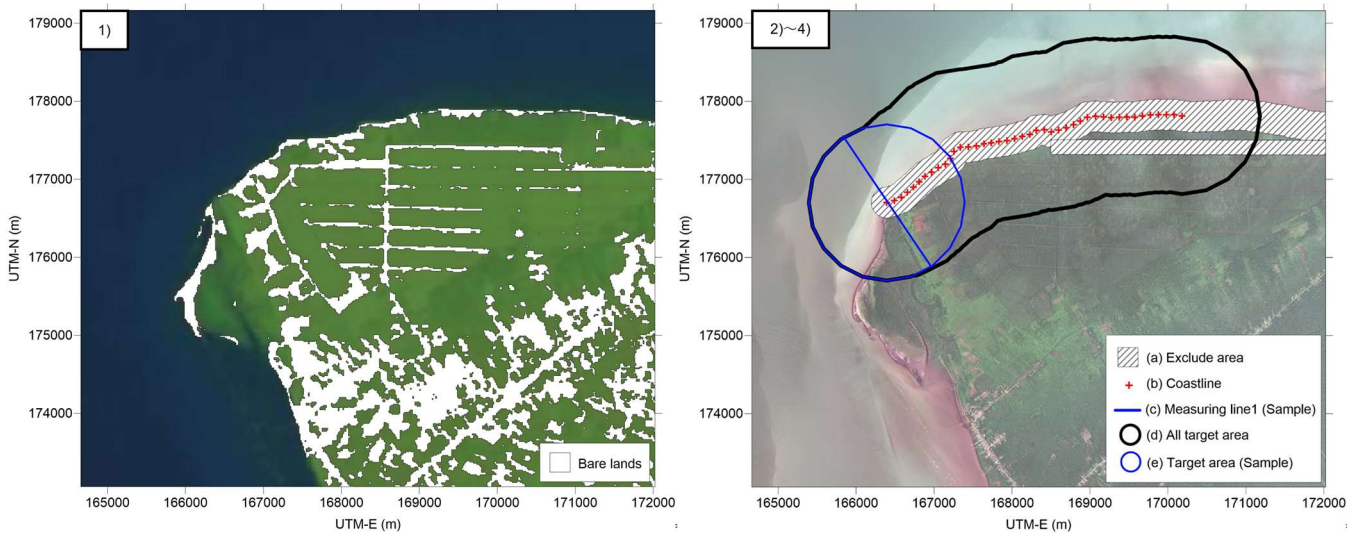
$$NDMI = \frac{B8A - B11}{B8A + B11} \quad (4)$$

560 Where *B8A* represents the NIR with 20 m resolution (wavelength: 865 nm); *B11* represents the SWIR with 20 m resolution (wavelength: 1610 nm). According to Mandanici and Bitelli, 2016, the Pearson correlation coefficient and the slope of the linear relationship between the reflectance and index values of the multispectral instrument (MSI) and the TM5 bands are as close to 1 as possible, with the intercept close to 0. Therefore, the machine learning model for land cover classification created for Sentinel 2 images was applied directly to Landsat5 images.

565 **3.2.6 Vegetation removal from DEMNAS data**

Because DEMNAS is a DSM that contains the tree height (vegetation), we removed the tree height from the DSM to make DTM. First, the bare lands in the research area in Landsat 5 image taken on 2 February 2010 were identified by the classifier that was established in 3.2.1 and binarized. The binarized bare land area and DEMNAS data were combined to extract elevation values for bare land. During this process, the peat swamp forest and adjacent bare road and a radius of 200 m from the coastline that were flagged as anomalies were masked (Fig. 7a). The 200 m radius DEMNAS data depicted collapsed terrain, which would not need to remove tree heights; therefore, these areas were excised. The DEMNAS derived coastline, which the points of the altitudes of 0 m at 100 m intervals were extracted (Fig. 7b). An approximation of the polynomial curve of the extracted coastline was calculated and a 2 km offshore measurement line was constructed centred on the coast (Fig. 7c). The radius of 1 km from the coastline was set as a buffer area for buffer analyses in GIS to obtain elevation of the bare land (Figs. 7d and 7e). For any point in which statistical values were not attainable, linear interpolation was applied between adjacent points. The elevation difference from the median bare land elevation was considered as tree heights and the difference was subtracted to calculate the bare land elevation. Values above 0 m elevation were used to interpolate by kriging to generate a DTM with an 8 m resolution.

580



585 **Figure 7: Methodology of removal of vegetation from DEMNAS data. 1) A Landsat5 image (2 February 2010) was used to classify bare land and other land covers using machine learning. 2) The bare land raster was set at 1 and multiplied by the DEMNAS data to produce the bare land elevation data. The elevation anomalies at the boundary between the peat swamp forest and the bare road and a radius of 200 m from the coastline (a) were masked. 3) A measuring line was made in the offshore direction from inland at points where the coastline was divided at 100 m intervals (b) (c). 4) The median elevation of the bare lands located 1 km (d) (e) from the coastline was assigned to the coastline and linearly complemented.**

3.2.37 Estimation of the volume of exported land slide-induced peat to the ocean

590 Aerial photogrammetry-derived DSMs were used to establish the relationship between the area and the loss of the peat volume by PMMs. This relationship was then used to estimate the losses in peat volume in areas affected by landslides identified in multispectral satellite imagery. Elevations before and after collapse were obtained by manually digitising the edges and inside the landslide-affected area within the GIS software (QGIS ver. 3.20) using orthomosaics and DSMs resulting from aerial photogrammetry carried out on 4 March 2017 and 29 July 2018, respectively, and within Estimation of the volume of export of land slide-induced peat to the ocean (Figs. FA1g, FA1h). The landslide-affected areas were judged by the characteristics of the ground, such as surface tension cracks or the presence of peat blocks. Tension cracks and irregular peat blocks are some of the characteristic features of peat mass movements (Warburton et al., 2004). Two digital elevation models (DEMs) were generated using aerial photogrammetry results. The first DEM was the initial land surface, which was recreated by interpolation using elevations of the points extracted from the edges of the areas affected by landslides within the DSM (Fig. FA1g). The second DEM was the post-collapse DEM, which were generated by sampling elevation data in areas affected by landslides in the vegetation removed DSM (Figs. FA1f, FA1h and FA1i). The volume of peat exported to the sea due to collapse was deduced by calculating the difference between the first DEM and the second DEM. The method to calculate the volume of peat exported by a PMM event is expressed in Eq. (15),

$$V_{PMM,i} = \iint_{A_{LS,i}} (h_1(t, x, y) - h_2(t + \Delta t, x, y)) dx dy \quad (51)$$

605 where $V_{PMM,i}$ represents the volume of peat exported to the ocean by a PMM event i (m^3), $A_{LS,i}$ represents the area i affected by the landslide (m^2), h_1 represents the elevation before the landslide (m), h_2 represents the elevation after the landslide (m), x and y represent the distance (m), t represents the change in time.

3.2.48 Estimation of the volume of peat exported by the PMMs using optical satellite images and UAV-based orthomosaic

610 Landslide-affected areas were extracted from optical satellite images and orthomosaic based on UAVs (Fig. FA1a, FA1b, FA1c, FA1d and FA1e). When landslide-affected areas were extracted from multispectral satellite imagery, areas with sparse vegetation were spotted using the true colour image and the false colour image (Figs. FA1a, FA1b, FA1c, and FA1d). The volumes of peat exported by landslide were estimated in these areas based on a previously determined area-volume/area

relationship. Landslide-affected area: $A_{LS,i}$ calculation was performed in the GIS software. The total amount exported to the ocean by PMMs: the V_{PMMs} are shown in Eq. (26) and Eq. (37).

$$615 \quad V_{PMMs} = \sum V_{PMM,i} \quad (26)$$

$$V_{PMMs} = \sum f(A_{LS,i}) \quad (37)$$

where $A_{LS,i}$ represents the area i affected by the landslide (m^2). f represents a function to estimate the volume of the Landslide-affected area. This study considered traced errors in landslide-affected areas, which were calculated by manual tracing in GIS software (Fig. G1B). We evaluated the errors caused by differences in resolution using satellite images from Landsat 8 and Sentinel-2 acquired at the same time ($n=7$). To achieve this, we conducted 20 tracings per time for comparison (Fig. H1E).

3.2.59 Calculation of coastal erosion volume

Accurate estimation of coastal erosion volume required detailed land cover classification and the removal of vegetation from elevation data. Appendix D outlines the land cover classification methodology based on machine learning, employing NDVI (Normalized Difference Vegetation Index) and NDMI (Normalized Difference Moisture Index) derived from Sentinel-2 imagery to differentiate between bare ground and vegetated areas. Appendix E describes the procedure for vegetation removal from DEMNAS elevation data in order to generate a Digital Terrain Model (DTM), thereby eliminating the influence of tree canopy height on surface elevation. These preprocessing steps provided a refined baseline essential for improving the accuracy of coastal erosion volume estimation.

To elucidate the area and volumetric magnitude of peatland loss due to coastal erosion, we drew coastlines using GIS software (QGIS 3.10) based on satellite images, orthomosaic results from aerial photogrammetry, and analysed their temporal changes. The defining equation to calculate coastal erosion is shown in Eq. (48).

$$630 \quad V_{CE} = \iint_{A_{CE}} (h(x,y) - h_B(x,y) - d_{PMM}(x,y)) dx dy \quad (48)$$

where V_{CE} represents the volume of peat exported by coastal erosion in each period (m^3), h represents the elevation of the ground before coastal erosion and PMMs (m), h_B represents the thickness of the clay base layer (m), A_{CE} represents the area eroded by coastal erosion (m^2) and d_{PMM} represents the average elevation drop by a PMM event (m). d_{PMM} is described by the following Eq. (59).

$$635 \quad d_{PMM} = \frac{V_{PMM}}{A_{LS}} \quad (59)$$

where V_{PMM} represents the volume of peat exported to the ocean by a PMM event (m^3), and A_{LS} represents the landslide-affected area (m^2).

640 Multispectral satellite imagery from Table 23 and orthomosaic results from aerial photogrammetry were used to plot the coastlines. For period (c), from 18 September 2013 to 2 April 2015, and (d) from 2 April 2015 to 4 March 2017, the ground elevations before the erosion were determined using the DTM derived from the DEMNAS data. During period (e), spanning from 4 March 2017 to 29 July 2018, perversion ground elevations were obtained from a DSM generated using aerial photogrammetry results obtained from the UAV. The DSM of the UAV photogrammetry was adjusted to remove the height

645 of the tree prior to use. The process of excluding tree heights from the DSM was carried out by checking trees on a UAV-
 based orthomosaic. Furthermore, the DSM of the UAV was corrected using the root mean square error (RMSE) values of the
 DTM generated from the RTK-GNSS and DEMNAS data. DTM using DEMNAS data does not consider landslide-affected
 areas, so landslide volumes are subtracted, but DSM from aerial photogrammetry results reflect spilt volumes due to landslides,
 so landslide volumes were used as they are, without subtraction. The volume of peat exported by coastal erosion, estimated
 650 using DTM, and the volume of peat exported by coastal erosion, estimated using DSM from UAV photogrammetry, are shown
 in the Eq. (610).

$$V_{CE} = \begin{cases} \iint_{A_{CE}} (h_{DTM}(x, y) - h_B(x, y) - d_{PMM}(x, y)) dx dy & (h = h_{DTM}) \\ \iint_{A_{CE}} (h_{UAV}(x, y) - h_B(x, y)) dx dy & (h = h_{UAV}) \end{cases}$$

(610)

where V_{CE} represents the volume of peat exported by coastal erosion in each period (m^3), h_{DTM} represents the elevation of the
 655 ground before coastal erosion and PMMs, that is, the elevation of DTM (m), h_B represents the thickness of the clay base
 layer (m), A_{CE} represents the area eroded by coastal erosion (m^2), and d_{PMM} represents the average decrease in elevation due
 to a PMM event (m). h_{UAV} [representsstands for](#) the elevation of the vegetation-free DSM based on the UAV photogrammetry
 (m). This study considered traced errors in coastal erosion areas, which were calculated by manual tracing in GIS software
 (Fig. BG).

660 3.2.610 Estimation of POC mass by PMM event and estimation of POC flux due to coastal erosions

The mass of the POC by the displacement of peat mass caused by PMMs and the POC flux due to coastal erosions were
 calculated by the spatial distributions of the loss of the peat volume and depth-dependent carbon stock of the peat. The carbon
 stock of peat $m_c(z)$ ($t m^{-2}$) until the depth z (m) of the peat from the surface of the ground was calculated using the following
 Eq. (744),

$$665 \quad m_c(z) = \int_0^z \rho_d \alpha_c dz \quad (744)$$

where ρ_d represents the dry density ($t m^{-3}$) and α_c represents the organic carbon content (-). They were combined from the
 results of field surveys with the value of the literature obtained from Wahyunto et al., 2003; Dariah et al., 2012; Warren et al.,
 2012 and Rudiyanto et al., 2018.

The mass of POC caused by a PMM event was calculated using Eq. (812),

$$670 \quad M_{PMM} = m_c(d_{PMM})A_{LS} \quad (812)$$

where M_{PMM} (tC) represents the mass of POC, the variable d_{PMM} represents the average decrease of elevation by a PMM event
 (m), and A_{LS} represents landslide-affected area (m^2). The amount of POC exported by the PMMs (tC) in each period was
 calculated using the Eq. (913),

$$M_{PMMs} = \sum M_{PMM} \quad (913)$$

675 where M_{PMMs} (tC) represent the mass of POC exported by the PMMs in each period. The mass of POC which is exported to the ocean caused by coastal erosion in each period was calculated using the Eq. (104). Eq. (104) is divided into two cases for elevation h (m) before coastal erosion and a PMM event: the case using DTM and the case using UAV aerial photogrammetry results.

$$M_{CE} = \begin{cases} \iint_{A_{CE}} m_c(h_{DTM}(x, y) - h_B(x, y) - d_{PMM}(x, y)) dx dy & (h = h_{DTM}) \\ \iint_{A_{CE}} m_c(h_{UAV}(x, y) - h_B(x, y)) dx dy & (h = h_{UAV}) \end{cases}$$

680 (104)

where M_{CE} represents the mass of POC caused by coastal erosion (tC), h_{DTM} represents the elevation of the ground before coastal erosion and PMMs, i.e. the elevation of the DTM (m), h_B represents the thickness of the clay base layer (m), A_{CE} represents the eroded area by coastal erosion (m^2) and d_{PMM} represents the average decline of the elevation by a PMM event (m), and h_{UAV} represents the elevation of the DSM from the UAV photogrammetry was removed tree height (m). The POC from the displacement of peat mass caused by PMMs and from fluxes due to coastal erosion were calculated using Eq. (115) and Eq. (126), where q_{POC} ($tC m^{-1}$) represents the POC from the displacement of the peat mass caused by PMMs. J_{POC} ($tC m^{-1} yr^{-1}$) represents the POC fluxes due to coastal erosion, l (m) represents the coastline distance, Δt (yr) represents the years of interval for coastal erosion. The POC from the displacement of peat mass caused by PMMs was not measured by fluxes, as PMMs are a sudden disaster. Instead, it was calculated based on the areas that had already collapsed by each date. In general, peat mass movements in boreal peatlands only uses the unit without time such as m^3 or tons to evaluate the magnitudes of these events (Dykes and Warburton, 2007).

$$q_{POC} = M_{PMMs} l^{-1} \quad (115)$$

$$J_{POC} = M_{CE} l^{-1} \Delta t^{-1} \quad (126)$$

690 The calculated POC shows the standard deviation (SD) of five patterns, including the values from the literature.

695

4 Results and discussion

4.1 ~~C~~Generation of digital terrain models and characteristics of landslide-affected area

700 ~~As a result of the machine learning of the landcover classification using NDVI and NDMI, we got the partition line separating vegetation area and bare land area given by Eq. (17). Validation results of the machine learning were as follows: true positive rate, 0.8804; recall, 0.6940; specificity, 0.9950; precision, 0.9885; negative predictive value, 0.8410; and F score, 0.4077.~~

$$\del{NDMI = 0.5198NDVI + 0.7505} \quad (17)$$

~~Fig. 8 shows the differences in the DEMNAS before and after vegetation removal. The median elevation values of the bare land within 1 km from coastline were used in the vegetation removal from the DEMNAS data. Comparison between ground surface geodetic survey results by Real Time Kinematic Global Navigation Satellite System (RTK-GNSS) and DEMNAS data~~

705 ~~after vegetation removal are presented in Fig. 9. The RMSE of the ground elevation obtained from the RTK-GNSS and DEMNAS data after vegetation removal was 0.6951 m. The RMSE was subtracted from the DSM obtained from the UAV aerial photogrammetry to match the DEMNAS elevation. This elevation difference can be caused from the skewness by the elevation decline because of the waterway.~~

710 An analysis of the correlation between the area and volume/area of PMMs from 2017 to 2018 in the coastal area of the oil palm plantation is presented in Fig. 610 and Eq. (138), Eq. (149), where V_{PMM} represents the loss of peat volume by PMMs (m^3), and A_{LS} represents the landslide-affected area (m^2).

$$\frac{V_{PMM}}{A_{LS}} = 3.0 \times 10^{-5} A_{LS} + 0.9121 \quad (R^2 = 0.2687)$$

(138)

$$f(A_{LS}) = 3.0 \times 10^{-5} A_{LS}^2 + 0.9121 A_{LS}$$

715 (149)

A linear relationship was observed between the landslide area and volume of the peatlands. If the V_{PMM} / A_{LS} is assumed to be the depth of the landslide-affected area, the higher the A_{LS} , the deeper the depth of the collapse. When collapse also occurs, it will be as deep as 1 m. The smallest collapse had an area of 0.11 ha and a volume of 491 m^3 . The largest collapse had an area of 3.70 ha and a volume of 85,173 m^3 . On average, the landslide-affected areas measured 1.51 ha in area and 22,546 m^3 in volume. The relationship between the volume exported to the ocean by peat mass movements (V_{PMM}) and landslide-affected area (A_{LS}) on Bengkalis Island indicates that the average reduction in ground level ($d_{PMM} = V_{PMM} / A_{LS}$), which ranged from 0.94-1.93 m (mean value = 1.33 m), increased with the area of landslide-affected area (A_{LS}). The ground-level drop was found to be around 0.91 m in small collapses. The depths of peatland degradation varied, but typically in boreal peatlands, blank peat degradation occurred at a depth of 0.6-3 m (Warburton et al., 2004). Koyama et al., 2018 performed geotechnical investigation results in the northwest of Bengkalis Island and revealed a tendency for sedimentary peat to be less than approximately 2 m below groundwater level and the penetration strength to decline. Furthermore, the average difference between the pre-collapse ground elevation and the bottom surface of the peatland cracks was 2.01 m, which indicates a possible correlation between the peatland degradation slide surface and sedimentary peat location.

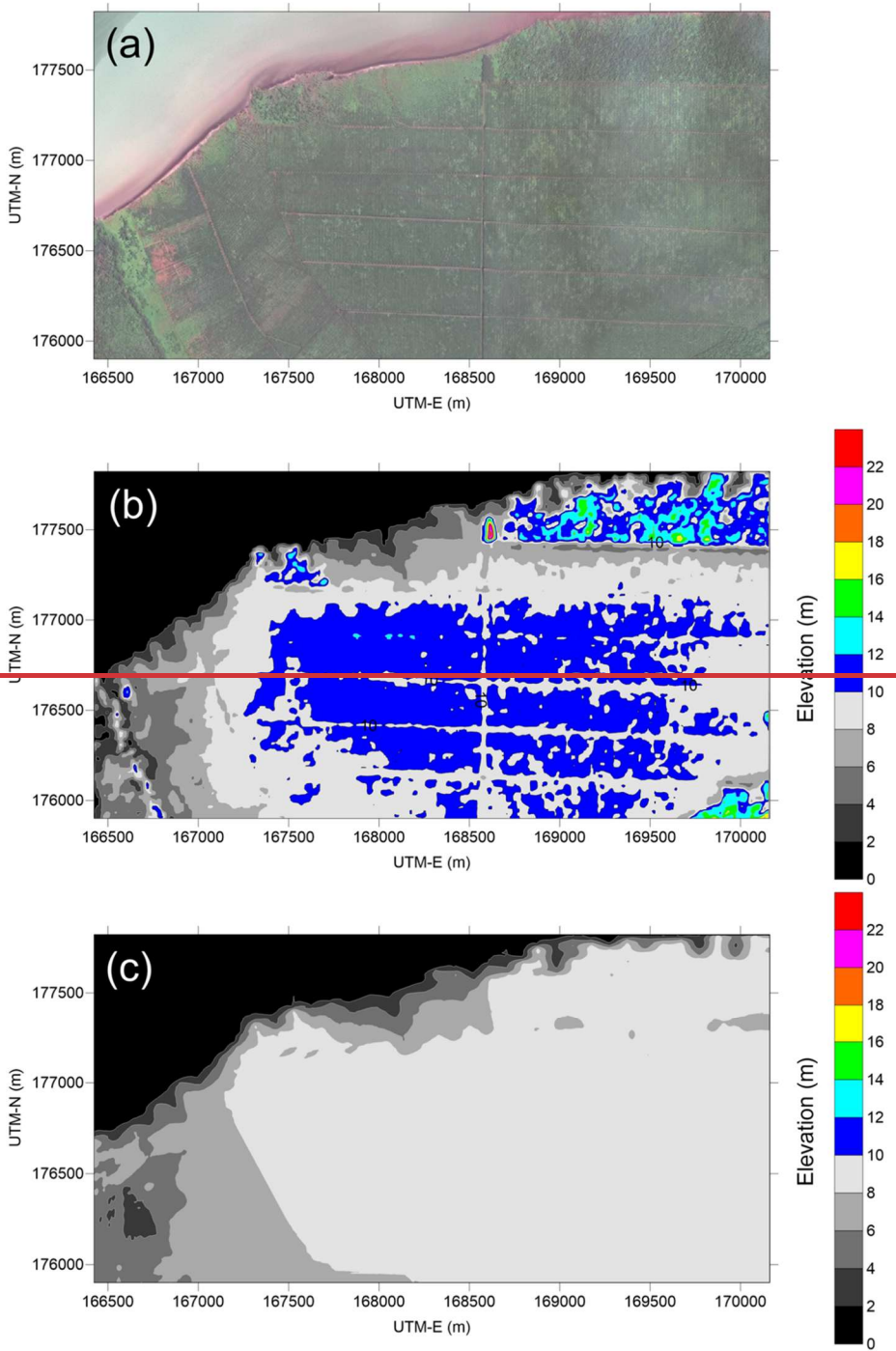
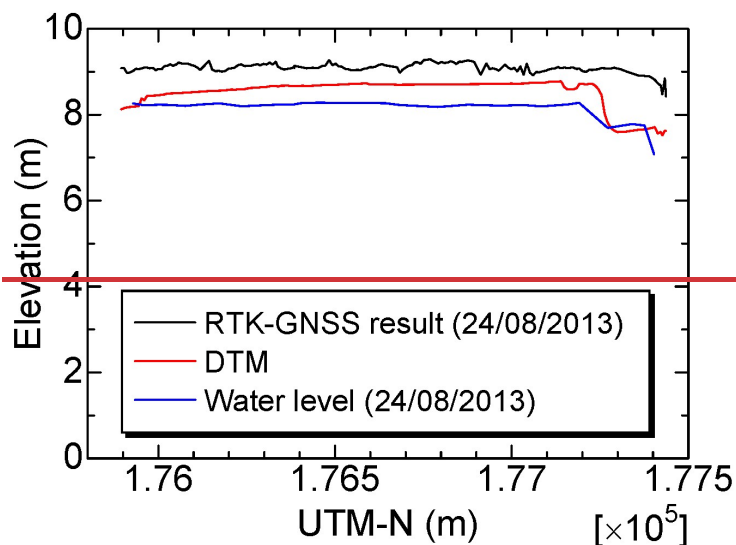
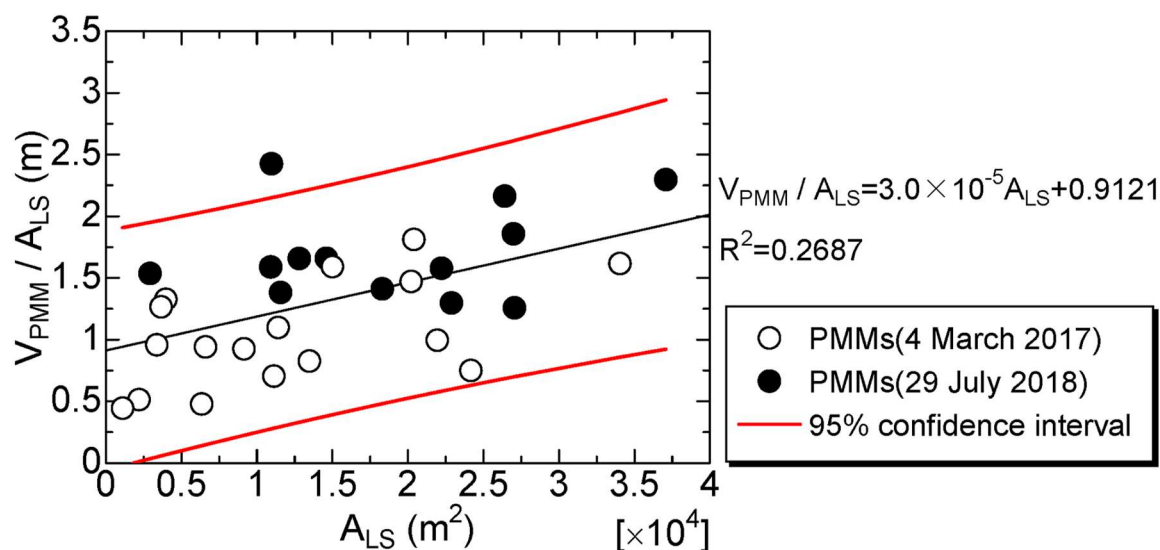


Figure 8: Comparison of (a) SPOT-6 data with (b) original DEMNAS data with (c) DTM removed from vegetation. The elevation of the bare land above 0 m was used to interpolate and generate a DTM with an 8 m resolution by kriging.

730



735 **Figure 9: Comparison of the RTK-GNSS land survey with a section created from DEMNAS data. The section where the elevations of DTM has decreased was the section where the collapse was identified in December 2013 after the RTK-GNSS land survey. The RMSE of removing the landslide-affected area was 0.6951 (m).**



740 **Figure 10: Area-Volume/Area relationship of a peat mass movement event. Where, A_{LS} is landslide-affected area, V_{PMM} is the loss of the peat volume due to a PMM event. There is a linear relationship between A_{LS} and V_{PMM} / A_{LS} ; If V_{PMM} / A_{LS} is assumed to be the depth of landslide-affected area, the greater the A_{LS} , the deeper the depth of the collapse. It was found that the ground level drop was around 0.91 m in small collapses.**

745 4.2 Identification of the timing of peat mass movement events

Fig. 744 shows the temporal changes in elevation along survey section A-A'. Variations in elevation indicate the occurrence of surface tears. In the section corresponding to UTM-N from 177,300 m to 177,400 m, the elevation decreased by an average of 2.01 m between 24 August 2013 and 11 March 2014. UAV-based aerial photogrammetry conducted on 17 December 2014 revealed that a peat collapse had occurred (Fig. 34c (A1)).

750 Fig. 842 displays an image obtained by SPOT-6 satellite imagery, UAV-based orthomosaic images and calculating the Visible Atmospherically Resistant Index (VARI) from UAV-based orthomosaic image in which only the exposed peat substrate is delineated. The extent of this PMM was estimated at 8.95 ha in area, with a volume of 321,940 m³, an aperture length of 296 m, and a length of 379 m. The landslide-affected area spans peat swamp forests, oil palm plantations, and shrublands. Furthermore, since 18 September 2013, the coastline has extended seaward, forming a fan-shaped deposit of peaty debris.

755 Next, the timing of the PMM was determined. In this analysis, the characteristic discontinuity in surface vegetation resulting from the collapse was used to pinpoint its timing. ~~Changes in NDVI and vegetation cover were plotted as a time series to highlight where the vegetation became discontinuous. Fig. 13a illustrates the relationship between vegetation cover and NDVI which exhibits a clear correlation, as expressed by Eq. (20) (with VC representing vegetation cover and $NDVI_{Sentinel-2}$ representing NDVI of Sentinel-2). Additionally, a strong correlation was observed between the NDVI values from Landsat 8 and Sentinel-2; this relationship is shown in Fig. 13b and expressed by Eq. (21), where x is the $NDVI_{Landsat8}$ from Landsat 8 and $NDVI_{Sentinel-2}$ is that from Sentinel-2.~~

760 ~~$$VC = 1.5692NDVI_{Sentinel-2} - 0.3817 \quad (R^2 = 0.8582)$$~~
(20)

765 ~~$$NDVI_{Sentinel-2} = 1.2578NDVI_{Landsat8} - 0.2349 \quad (R^2 = 0.9571)$$~~
(21)

Fig. 914 presents the time series of vegetation cover for the peat collapse area identified in Fig. 34c (A1). The vegetation cover dropped sharply from 0.87 on 27 December 2013 to 0.21 on 13 February 2014, indicating that the collapse occurred between these dates.

770 Moreover, along survey section A-A' in the UTM-N range from 177,000 m to 177,300 m, the elevation decreased by an average of 2.07 m between 20 August 2014 and 10 January 2015 (Fig. 147). UAV-based aerial photogrammetry on 10 January 2015 confirmed that this decrease in elevation was due to a ~~peat~~-(peat (Fig. 34c (A2)). Areas exhibiting fluctuating elevations indicate the presence of peat rafts—blocks of peat displaced by the collapse (Warburton et al., 2004). Fig. 150 shows an image obtained by SPOT-6 satellite imagery, UAV orthomosaic images and calculating the VARI from UAV orthomosaic images, with only the exposed peat substrate delineated. In this case, the PMM was estimated to cover an area of 14.9 ha with a volume of 0.068 km³, an aperture length of 303 m, and a length of 554 m. The PMM also resulted in the formation of a large

peaty debris fan, which had an area of 13.7 ha, an aperture length of 583 m, and a length of 268 m; the formation of such an extensive fan underscores the large scale of the collapse.

The time series of vegetation cover at the landslide-affected area (Fig. 914) shows that between 27 October 2014 and 16 February 2015 the vegetation cover decreased rapidly from 0.82 to 0.48, suggesting that the PMM occurred during this period. Furthermore, Sentinel-1 satellite imagery indicates that approximately 18.4 ha of land area expanded abruptly between 22 December 2014 and 28 December 2014 (Fig. 914), clearly indicating that a large-scale collapse occurred during this interval.

Fig. 161 presents the water level data alongside rainfall data from Selat bBaru at the landslide-affected area. During the observation period, the maximum rainfall recorded was 107.9 mm day⁻¹ on 23 December and 84.1 mm day⁻¹ on 26 December. Following this record rainfall, the water level in the waterway suddenly dropped on 27 December 2014. Although the crest level of the waterway is 9.00 m, the water level was recorded at 9.124 m at 11:10 on 27 December 2014 and then fell sharply to 7.896 m just ten minutes later (Fig. 161). This abrupt decrease suggests that a breach of the weir occurred between 11:10 and 11:20 on 27 December 2014, triggering the PMM. It was also confirmed that the on-site water level logger had shifted by approximately 30 m. The changes in coastal topography indicate that, because of the PMM, peat was exported into the marine environment. At the study site, continuous rainfall exceeding 20 mm·h⁻¹ was recorded from 21 December to 26 December, suggesting that the precipitation after 21 December may have triggered the collapse on 27 December.

Boylan et al., 2008 investigated the relationship between the runout distance and failure volume of 44 recorded peat landslides in northern parts of the United Kingdom (particularly the North Pennines) and throughout Ireland (particularly Connacht and Munster). According to this data, the runout distance generally increases with failure volume, although there is considerable variability. Larger failure volumes and consequently longer runout distances tend to occur in raised bogs, which contain deeper and more extensive peat deposits. The long runout of peat landslides can be transported over long distances when they enter rivers and streams and mix with floodwaters. Runout distance can reach up to approximately 7000 m, and the failure volume can reach up to approximately 10,000,000 m³. Specifically, the PMM in Fig. 812 is smaller in scale than the peat landslides in boreal peatlands. However, compared to the boreal peatland landslides in Fig. 150, it has a shorter runout distance but a volume that is 6.8 times larger.

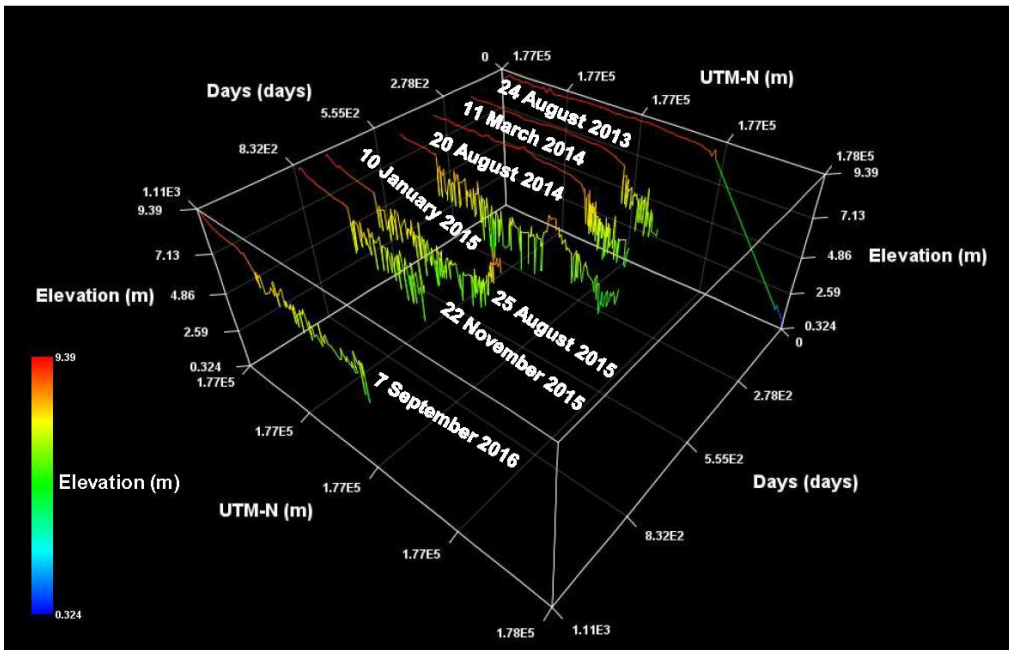
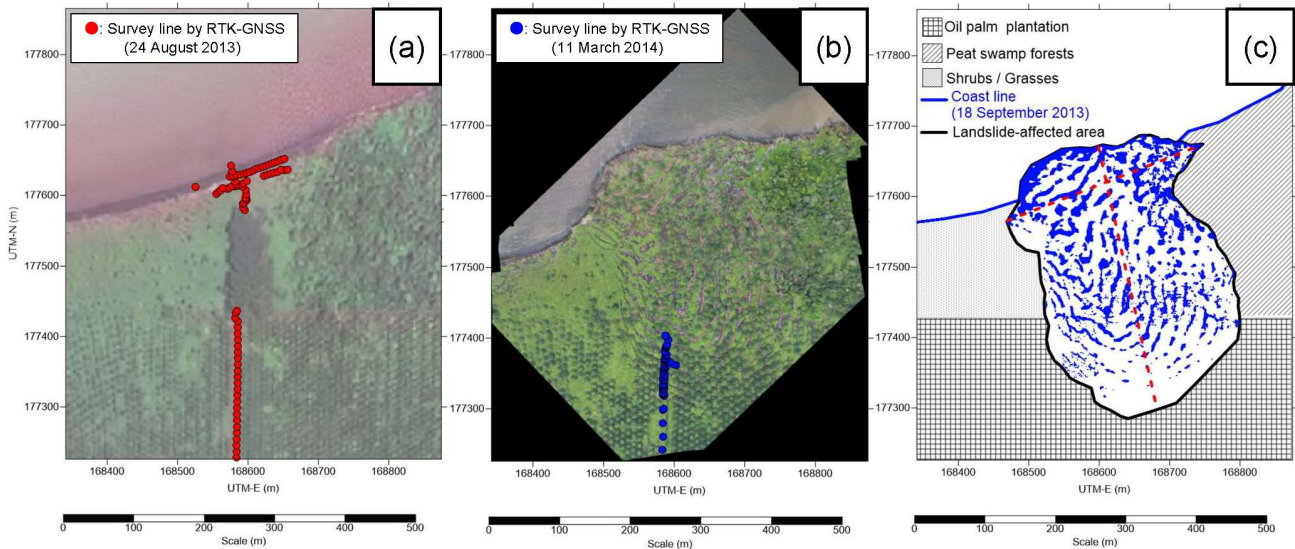


Figure 117: The change in temporal elevation in Section A-A'. The elevation decreased due to PMM from 24 August 2013.



805

Figure 812: (a) SPOT-6 image (18 September 2013) and (b) UAV-based orthomosaic image (17 December 2014), and (c) anatomy of the landslide-affected area. The scale of the landslide-affected area is as follows: the affected area is 8.95 ha, the volume is 321,940 m³, the length is 379 m, and the aperture length is 296 m. The collapse extended over or into peat swamp forests, oil palm plantations, and shrub areas.

810

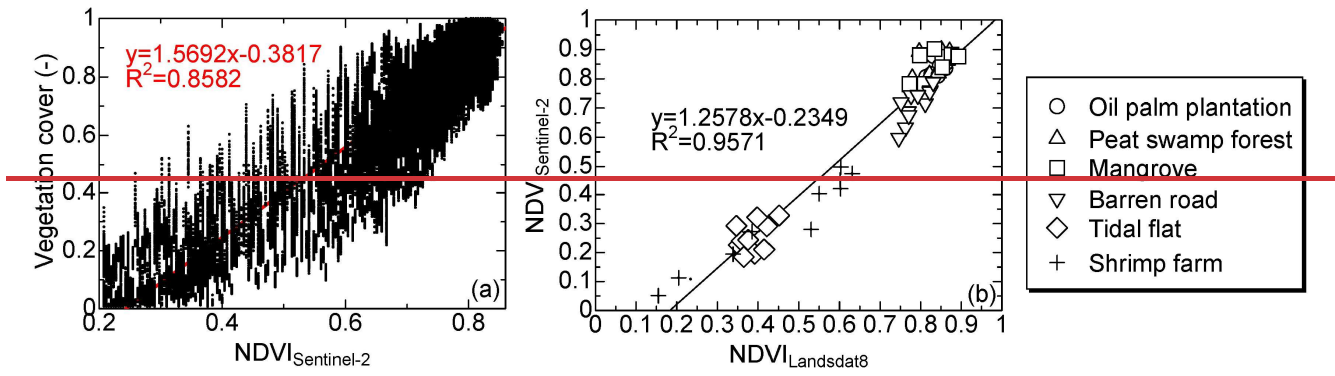
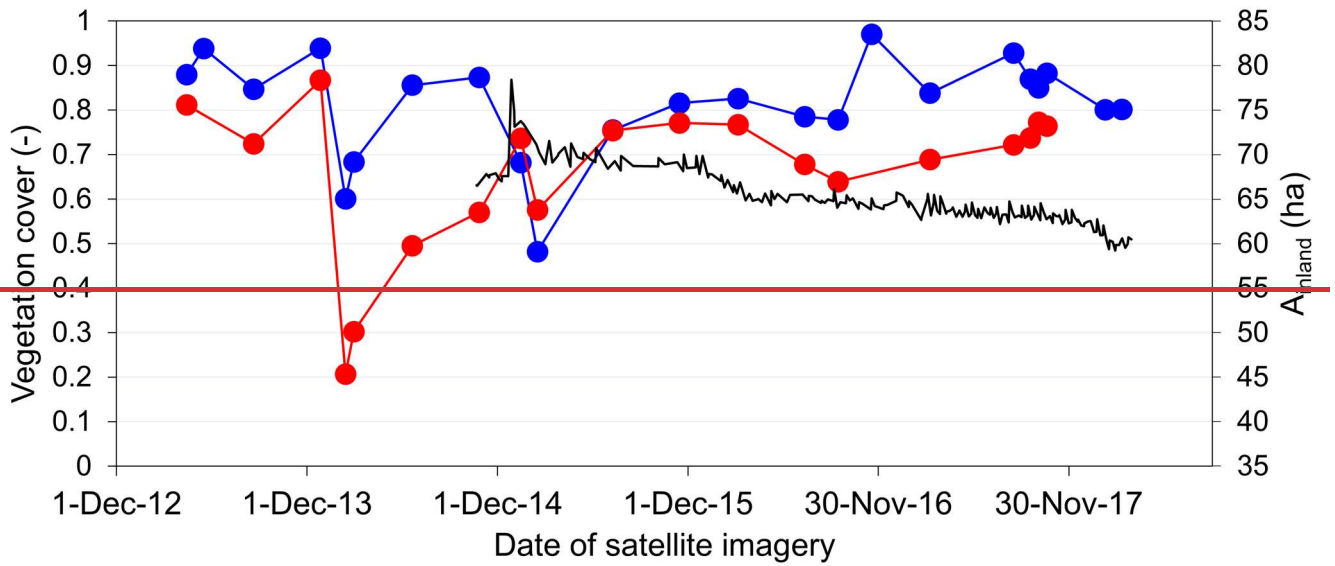
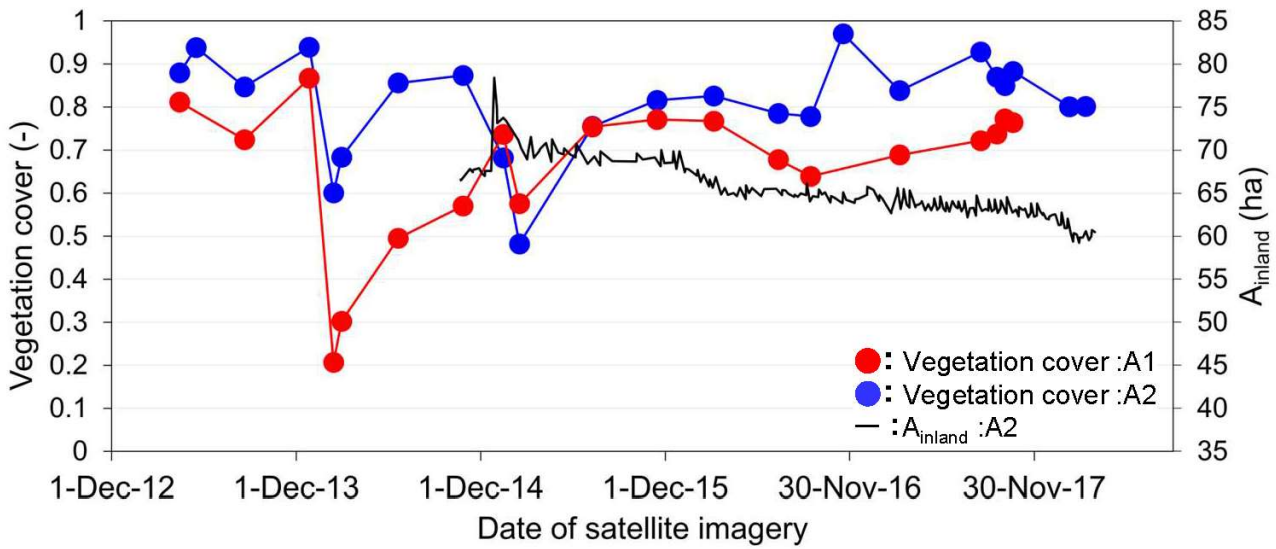


Figure 13: (a): Relationship between Sentinel 2 NDVI and vegetation cover (b): Relationship between Landsat 8 NDVI and Sentinel 2 NDVI, and Both figures show a linear relationship.

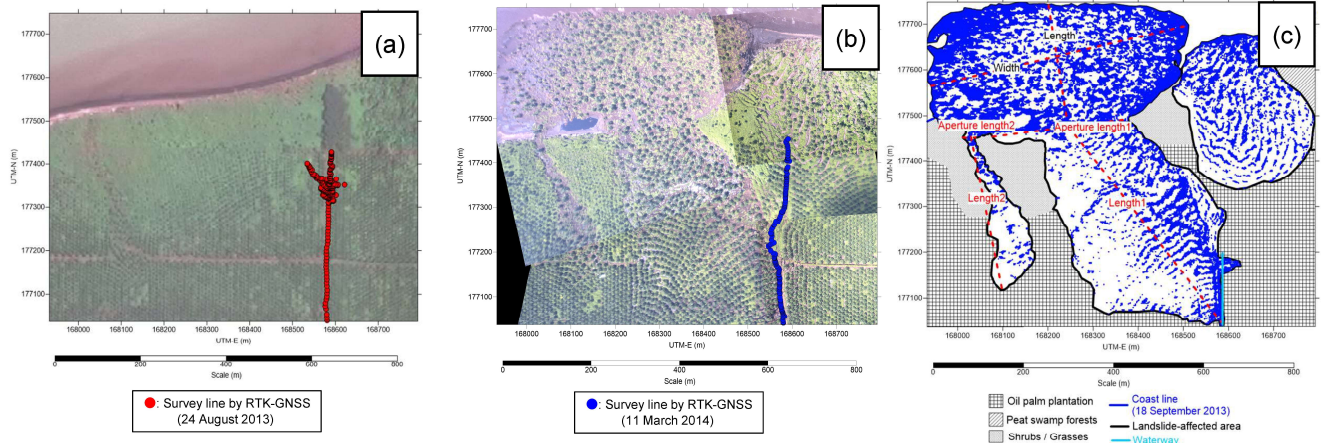


815

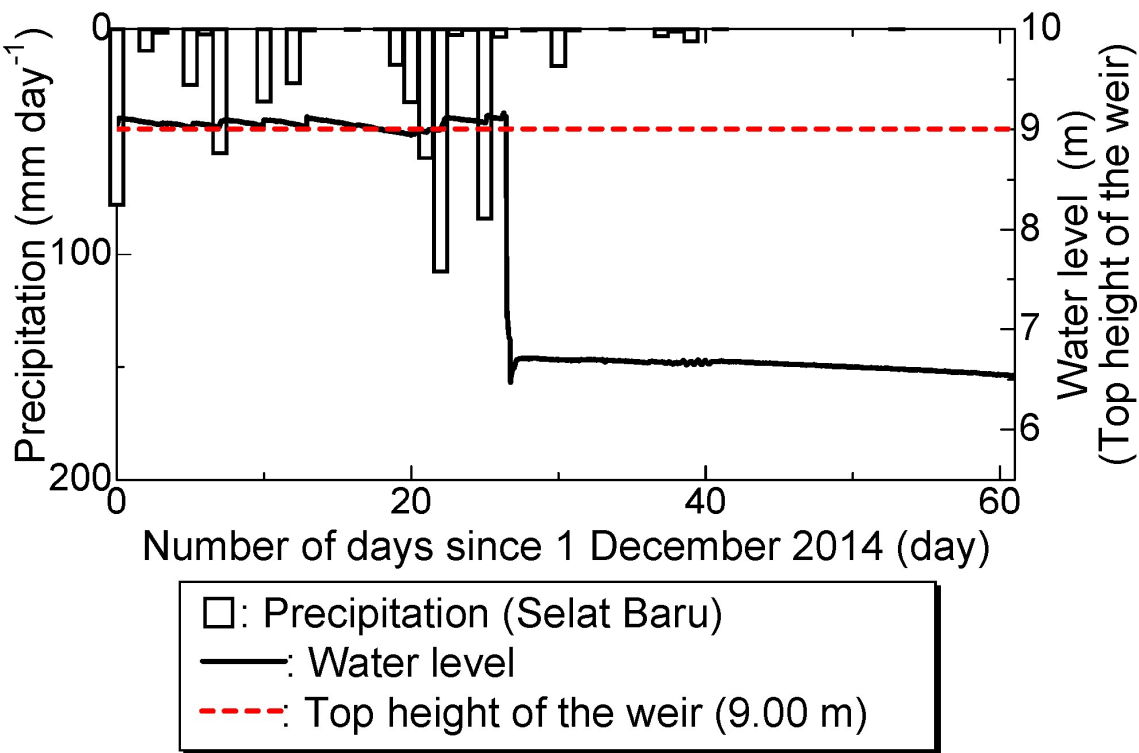
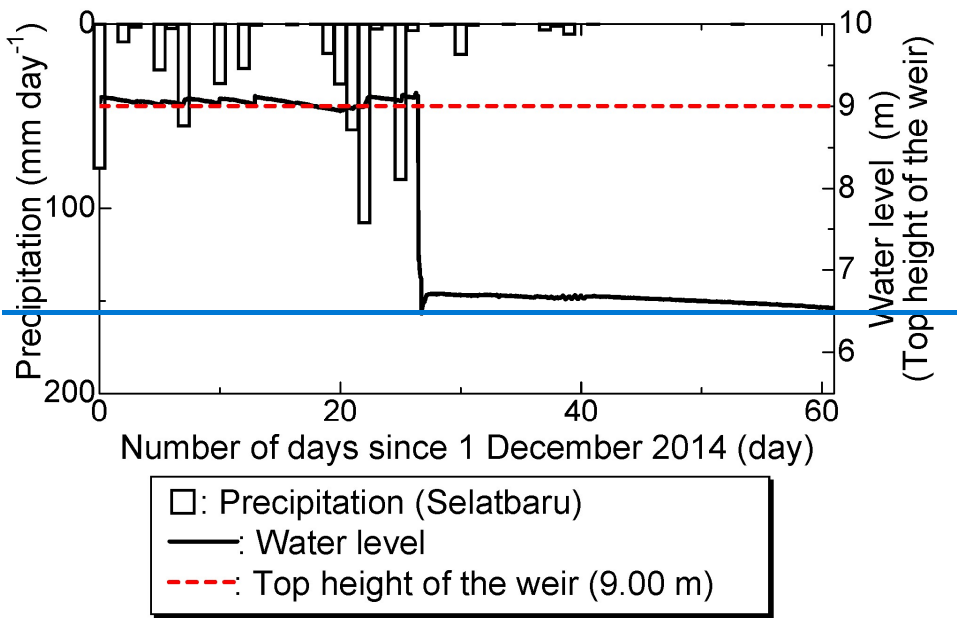


820

Figure 914: Time series of vegetation covers in landslide-affected areas. Vegetation covers rapidly decreased from 27 December 2013 to 13 February 2014, dropping from 0.87 to 0.21 (A1). Similarly, vegetation covers rapidly decreased from 27 October 2014 to 16 February 2015, declining from 0.87 to 0.48 (A2). The land experienced a sudden extension, increasing by approximately 18.4 ha between December 22 and 28, 2014 (A2).



825 **Figure 150:** (a) SPOT-6 image (18 September 2013), (b) UAV-based orthomosaic image (10 January 2015), and (c) anatomy of the landslide-affected area. The scale of the landslide-affected area is as follows: the area is 14.9 ha, the volume is 0.068 km³, Length 1 is 554 m with an aperture length of 303 m, and Length 2 is 341 m with an aperture length of 28 m. The scale of the peaty debris fan is as follows: the area is 13.7 ha, the length is 268 m, and the width is 583 m.



830 Figure 161: Water level of the water way at P02 and precipitation at Selat Baru station during the peat mass movement event on 27th Dec. 2014. The major precipitations before the event were 107.9 mm day⁻¹ (Dec. 23) and 84.1 mm day⁻¹ (Dec. 26). Subsequently,

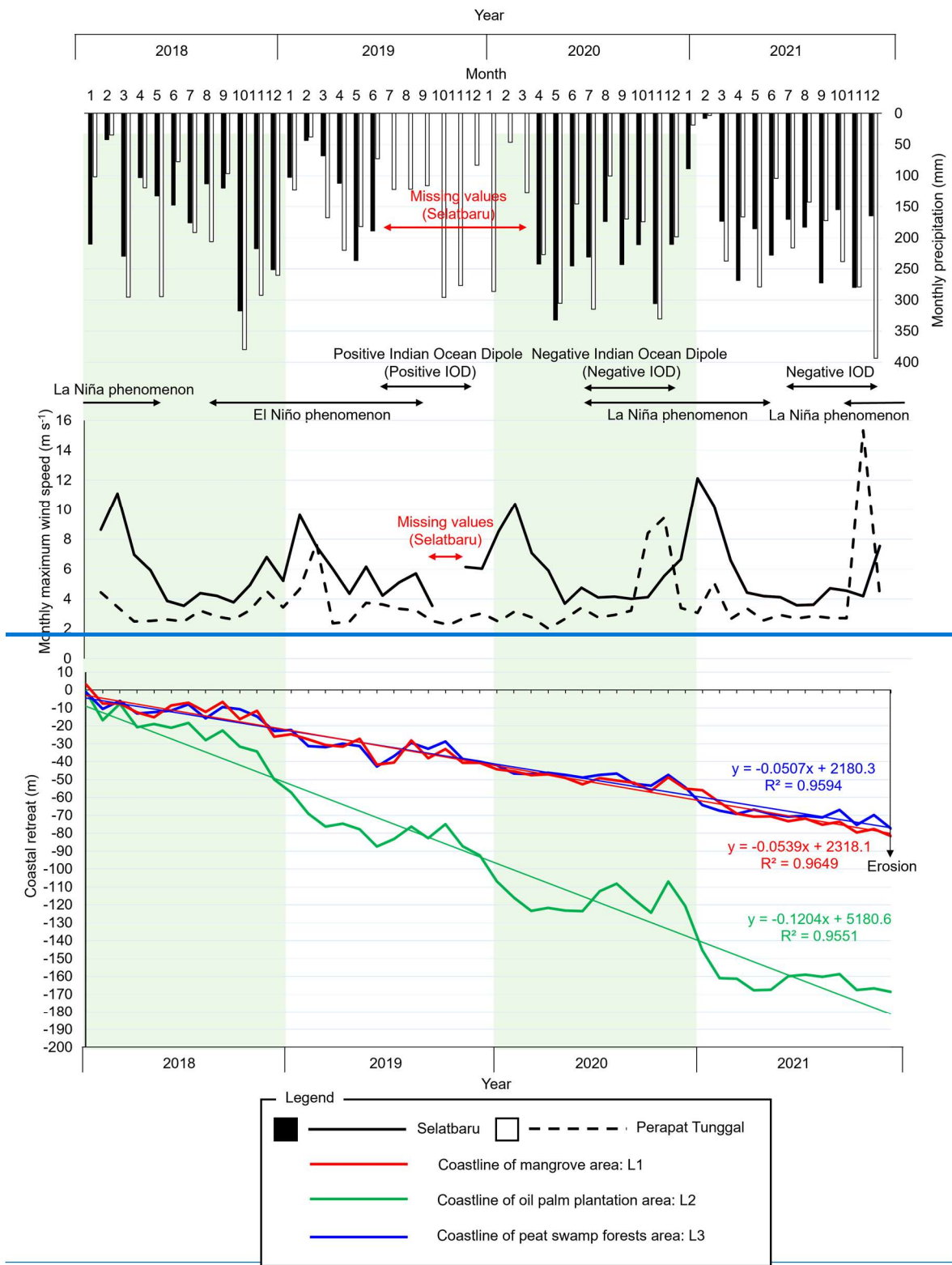
the water level of the water way dropped suddenly on Dec. 27, 2014. The top height of the weir was 9.00 m, but the water level was recorded at 9.124 m at 11:10 on December 27, 2014, followed by a sudden drop to 7.896 m just 10 minutes later.

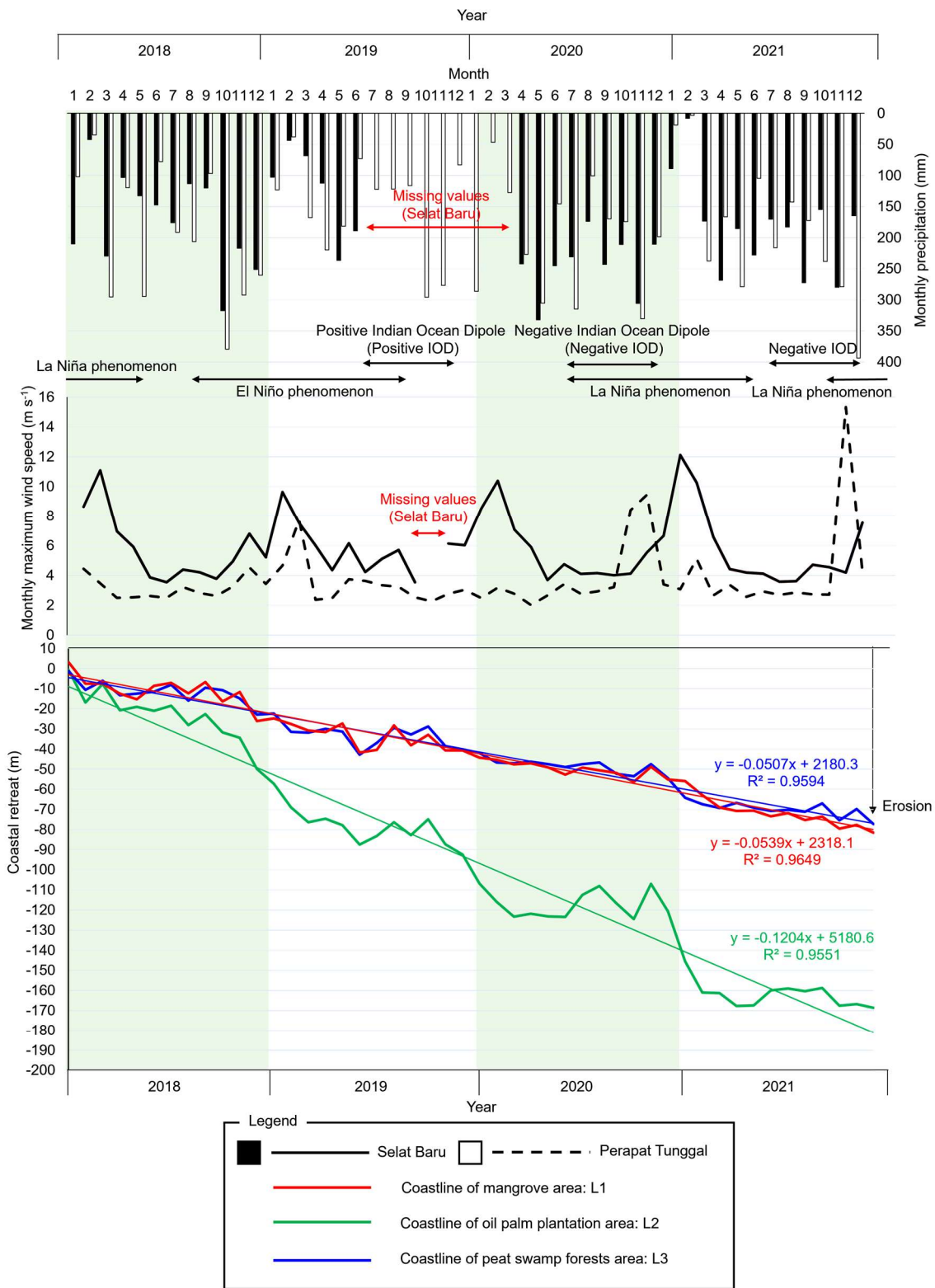
835 4.3 Estimation of coastal retreat

Based on the long-term changes observed in SAR imagery, along with local meteorological and mooring observations, the actual state of coastal erosion along the northern coast of Bengkalis Island was elucidated using land cover information and meteorological conditions. Fig. 127 shows the cumulative retreat of the coastline by land cover type from 2018 to 2021, as derived from Sentinel-1 data, alongside concurrent meteorological observations. Although coastal erosion has progressed in all land types including mangrove area, oil palm plantations, and peat swamp forests the erosion rate in oil palm plantations is more than twice that observed in mangrove area and peat swamp forests. Moreover, between 2018 and 2021, coastal erosion in oil palm plantations proceeded at an average rate of 3.5 m per 30 days, exceeding the typical average during Indonesia's rainy season, with the highest rate recorded at 24.8 m per 30 days in January 2020. These results suggest that elevated wave heights induced by seasonal winds may accelerate the erosion process.

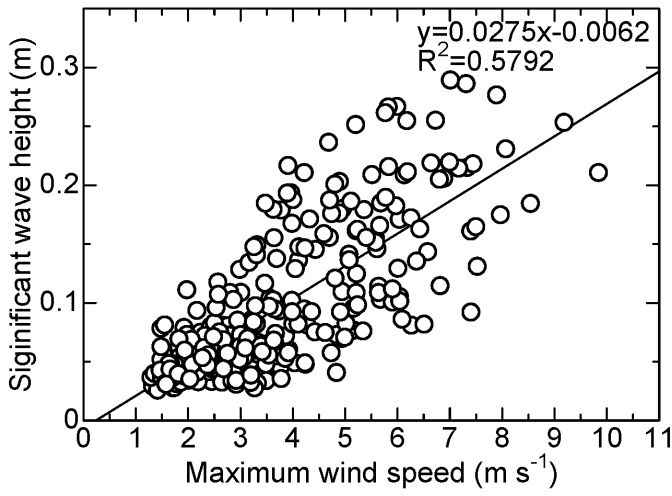
845 Fig.138 illustrates the relationship between significant wave height and maximum wind speed, demonstrating that higher wind speeds correspond to greater significant wave heights. Additionally, annual wind roses for Perapat Tunggal and Selat bBaru for 2018 and 2021 are presented in Fig.149. In Perapat Tunggal, both years exhibit dominant winds from the west and northwest throughout the year, with westerly winds accounting for 16.39% of the observations and a maximum wind speed of 65 m s⁻¹ recorded at 14:30 local time on 30 October 2018. In contrast, in Selat bBaru, winds from the east and northeast predominated in both years; in 2018, easterly winds were most frequent at 15.20%, and in 2021 a maximum wind speed of 20.3 m s⁻¹ was recorded.

855 Along the northern coast of Bengkalis Island, the lateral degradation of the mangrove areas has exposed the underlying peat substrate to coastal processes. Under the prevailing tidal and wave conditions, three types of erosion and progressive failure namely, toppling failure, rotational sliding, and cantilever failure have been documented (Basir et al., 2023). Consequently, during seasons characterized by dominant high wind speeds, increased wave heights may further accelerate coastal erosion.



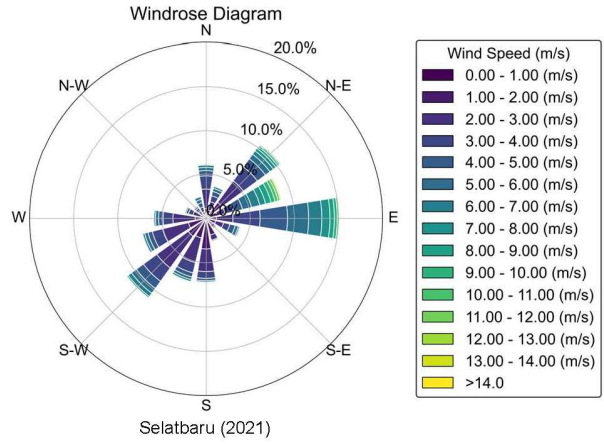
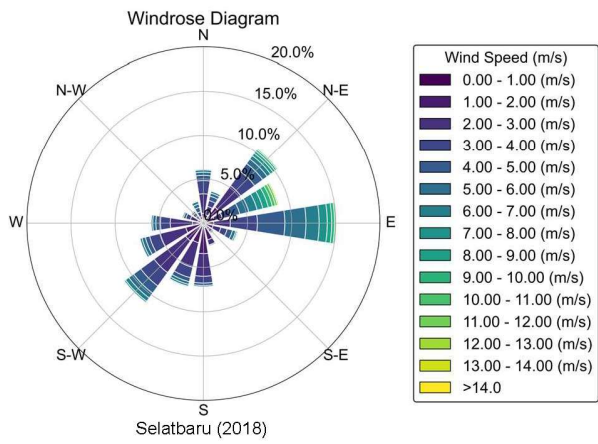
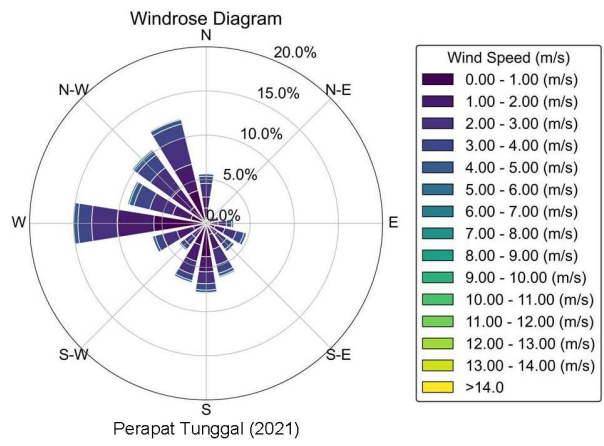
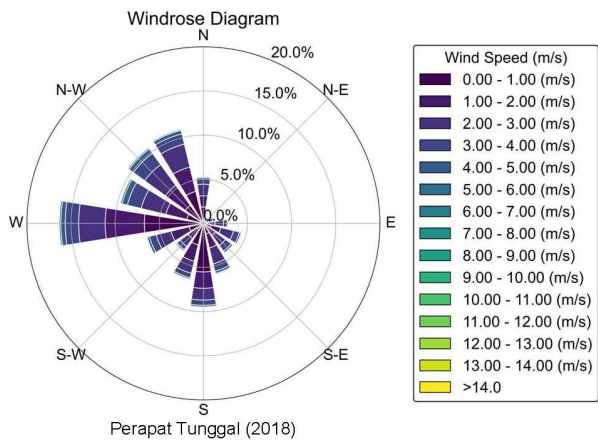


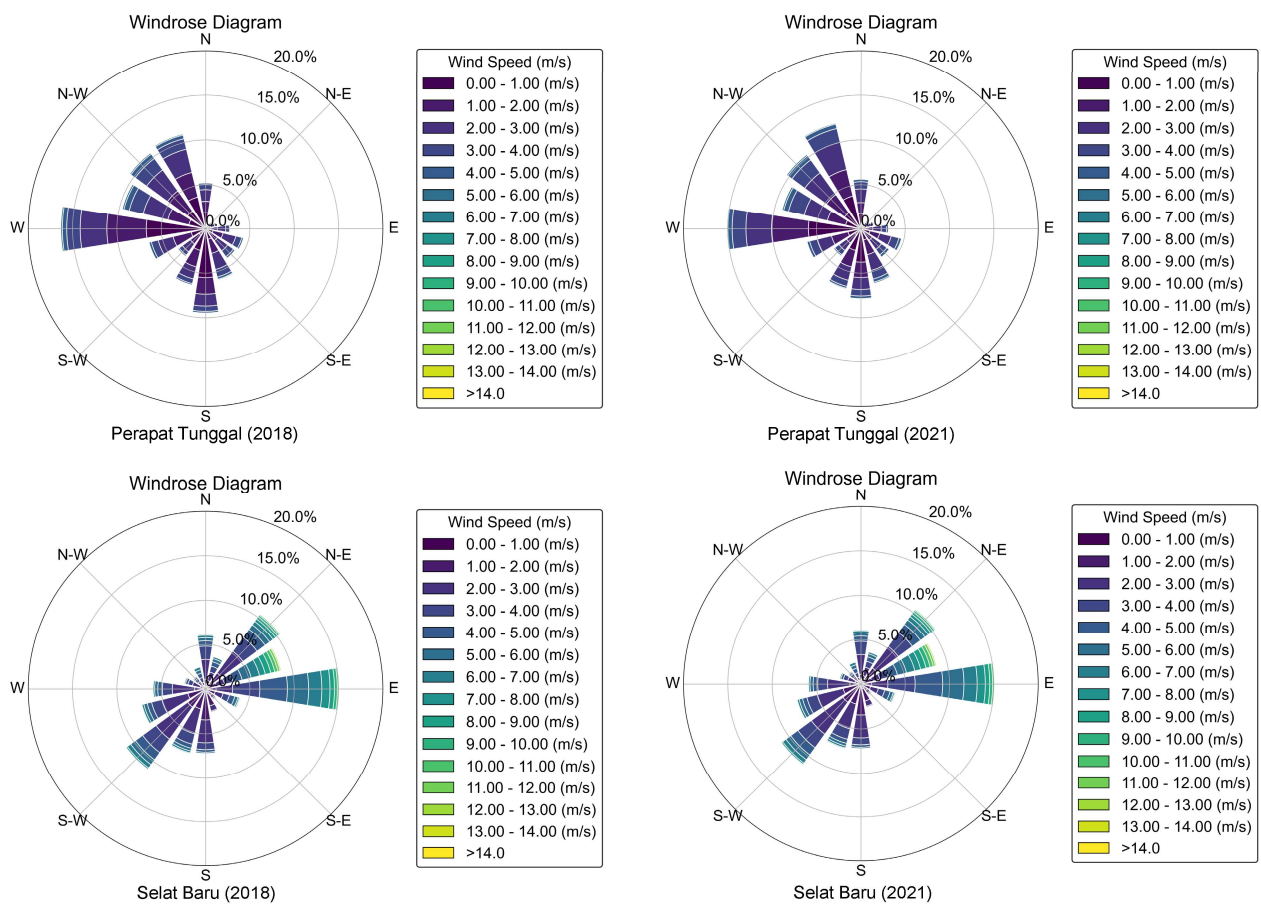
860 **Figure 127:** Cumulative coastline retreat by land cover type from 2018 to 2021, derived from Sentinel-1 data, alongside concurrent meteorological observations. Coastal erosion has progressed across all land types, including mangrove areas, oil palm plantations, and peat swamp forests. However, the erosion rate in oil palm plantations is more than twice that in mangrove areas and peat swamp forests. Erosion is further accelerated by the prevailing monsoon winds during ~~the winter~~ the winter in the northern hemisphere.



865

Figure 138: Relationship between maximum wind speed and significant wave height at the offshore of the Bengkalis Island (St. M).





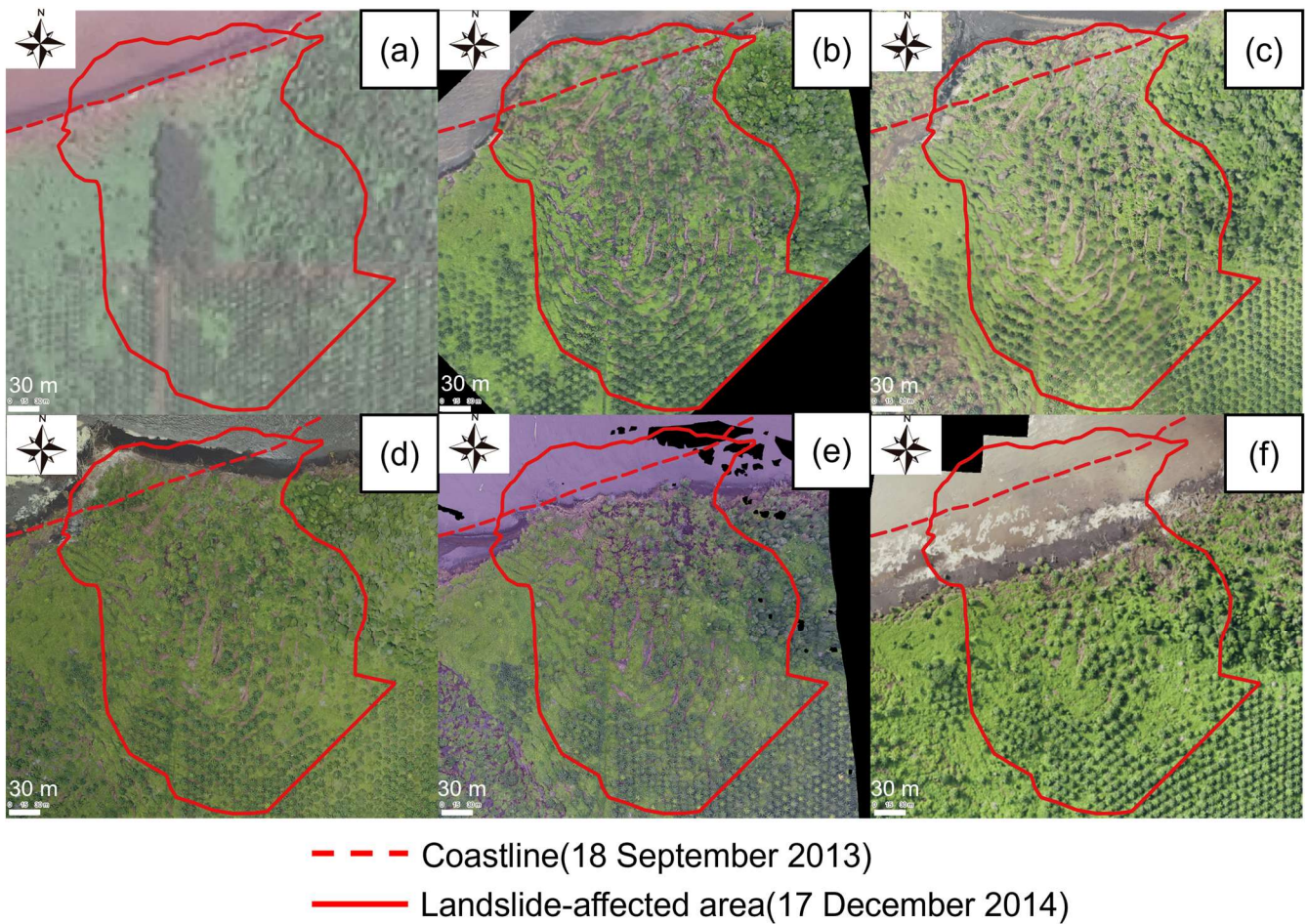
870 **Figure 149:** Annual wind rose diagrams for Perapat Tunggal and Selat Baru in 2018 and 2021.

4.4 Lateral degradation process of tropical peatland coasts

In tropical coastal areas, coastal erosion is accompanied by PMMs. A common characteristic of coastal land collapses is the spontaneous release of peat masses from the inland to coastal regions due to concentrated rainfall, which forms a peaty debris fan-shaped terrain. This article presents a one-year interval field observation study reporting the occurrence of a PMM event accompanied by coastal erosion. Fig. 1520 shows the annual changes in the area affected by landslides in the northwest area of Bengkalis Island. Following the PMM event, continuous coastal erosion resulted in traces of collapse. The land area initially increased after the PMM event but subsequently decreased during coastal erosion. Fig. 1520a shows a high-resolution satellite image (SPOT-6) captured on 18 September 2013, which depicts the state before the PMM event. At the concerned site, the southern part consists of an oil palm plantation and the northern part consists of a peat swamp forest. Although the state of the PMM event after capture is uncertain, given the consistent coastal erosion in this area since 1972, according to Landsat images, coastal erosion could have occurred after the collapse. Fig. 1520b shows the area affected by the landslide after the PMM

875
880

event photographed by UAV on 17 December 2014. Peat masses migrated from inland to the coast and formed a peaty debris fan. The fan extended offshore beyond the coastline on 18 September 2013. The area of the peaty debris fan formed is 0.80
885 hectares. Further inland, pull-apart cracks were observed, which could have been caused by the gushing of peat toward the coast. From 18 September 2013, coastal erosion has continued in non-cracked coastal areas. This phenomenon indicates continued coastal erosion even before any coastal PMM event. Fig. [1520c](#) shows the conditions captured by the UAV on 10
January 2015. A larger PMM event occurred on the western side of the coastal PMM event, as identified in the previous year. UAV observations resulted in the identification of a larger, peaty debris fan-shaped structure that was not confirmed on 17
890 December 2014. The structure of the peaty debris fan-shaped land formed by the movement of peat masses was observed to have changed, although no significant changes were observed in the PMM event on 17 December 2014. Fig. [1520d](#) shows the UAV results from 5 March 2016. The peaty debris fan-shaped land caused by the large-scale PMM event in the west on 10
January 2015, had disappeared. The peaty debris fan-shaped land formed due to the PMM event on 17 December 2014, notably disappeared on 10 January 2015. Between 10 January 2015 and 5 March 2016, the peaty debris fan was gradually eroded from
895 the east by waves (Fig [1520d](#)). Fig. [1520e](#) shows the UAV results for 4 March 2017. The peaty debris fan-shaped land that jutted out from the coastline on 18 September 2013, formed due to the PMM event on 17 December 2014, had completely
disappeared by 4 March 2017, and the coastline retreated from its original position on 18 September 2013. Fig. [1520f](#) shows the UAV results from 29 July 2018. The coastline has receded considerably since September 18, 2013, due to progressive
900 coastal erosion. From 18 September 2013 to 29 July 2018, the coastline receded by approximately 90 m, averaging an annual retreat of approximately 18 m. As shown in this chapter, when a PMM event occurs in the coastal zone, a peaty debris fan is
formed, leaving a collapse scar in the hinterland. The coastal erosion then proceeds until peat cliffs are formed.



905 **Figure 1520:** Annual changes at the landslide-affected area in the northwestern part of Bengkalis Island. (a) Initial status of the focus area with a peat cliff coastline (SPOT-6, 18 September 2013). (b) The immediate aftermath of a peat mass movement; a peaty debris fan was confirmed outside the initial coastline, with many tears observed on the ground surface of the hinterland (UAV-based orthomosaic, 17 Dec. 2014). (c) A larger peat mass movement occurred in the western area, creating a second peat fan, while the first peat fan remained (UAV-based orthomosaic, 10 Jan. 2015). (d) The second peaty debris fan in the west area completely disappeared, while the first peaty debris fan remained (UAV-based orthomosaic, 5 Mar. 2016). (e) Gradually, the first peaty debris fan eroded and decreased in area (UAV-based orthomosaic, 4 Mar. 2017). (f) The first peaty debris fan disappeared, and the coastline receded approximately 90 m from the initial status on average, returning to a peat cliff (UAV-based orthomosaic, 29 Jul. 2018).

910

4.5 Analysis of soil sampling results: distribution of dry density, carbon concentration, and moisture content

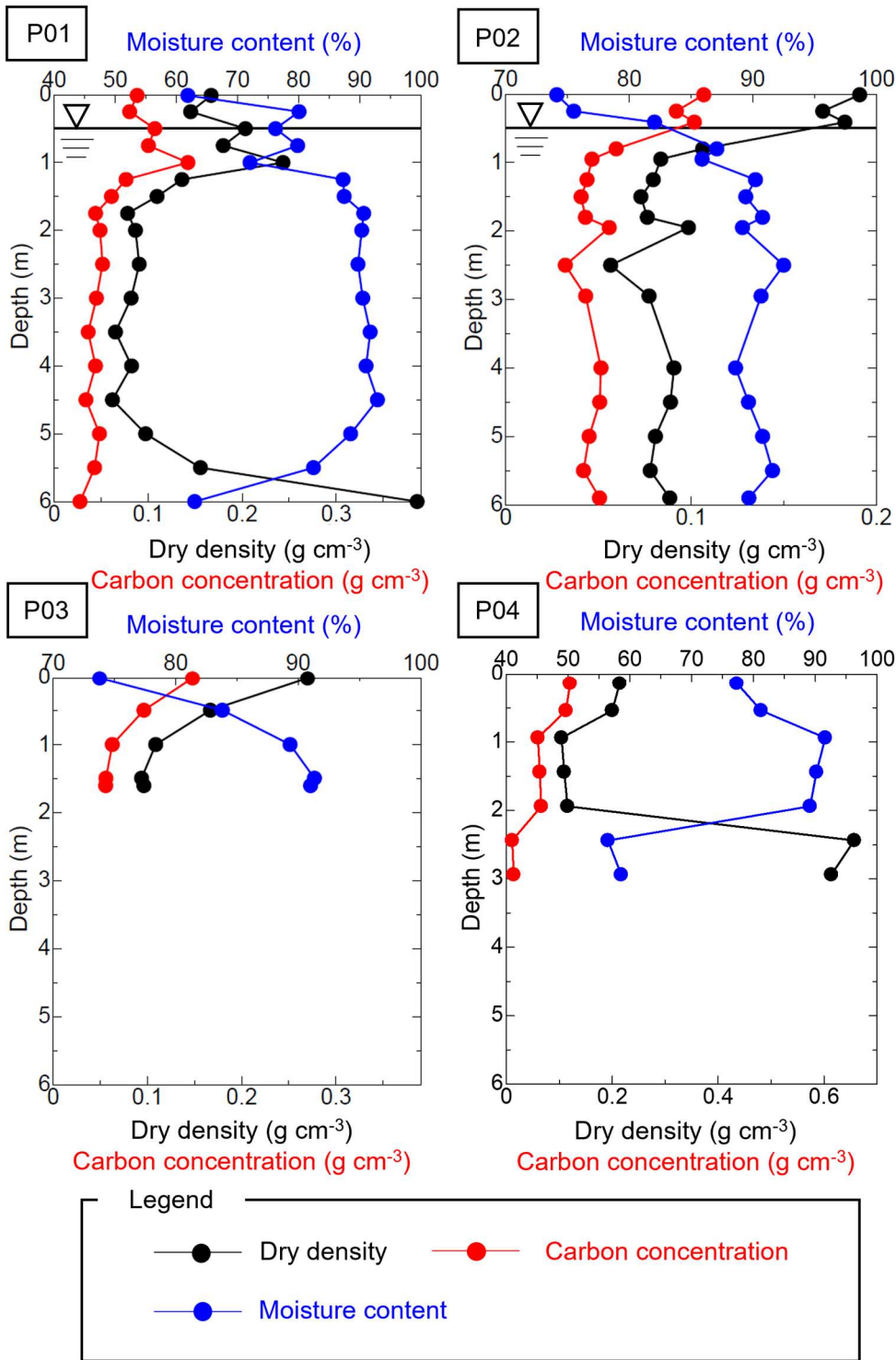
Fig. 1621 shows the vertical distributions of dry density, carbon concentration, and moisture content. Under the groundwater level, a high moisture content, low dry density, and low carbon concentration were observed. High values of dry density and carbon concentration may have been observed on the surface of groundwater due to oxidative decomposition.

The accumulated organic carbon content was calculated vertically downward from the surface. The accumulated organic carbon content derived from the field survey results and literature values (Wahyunto et al., 2003; Dariah et al., 2012; Warren et al., 2012; Rudiyanto et al., 2018) is shown in Fig. 1722. The accumulated organic carbon content was approximated by Eq. (1522), using peat obtained from the field survey. where $m_c(z)$ represents the accumulated carbon content ($t\ m^{-2}$), and z represents the depth of the peat layer from the ground surface (m).

$$m_c(z) = 0.0982z^{0.679} \quad (R^2 = 0.9636)$$

(1522)

The results of peat sampling during the field survey could be approximated by the power approximation curve. The higher cumulative carbon content to a depth of 2 m is due to the groundwater table being present at a depth of 2 m, the environment being conducive to oxidative decomposition at the surface, and consolidation results in a higher bulk density. The outflow of particulate organic carbon into the sea due to coastal erosion and peatland degradation was estimated using the power approximation curve relationship described in this section.



930

Figure 1621: Vertical distribution of dry density of peat, carbon concentration, and moisture content by peat core analysis.

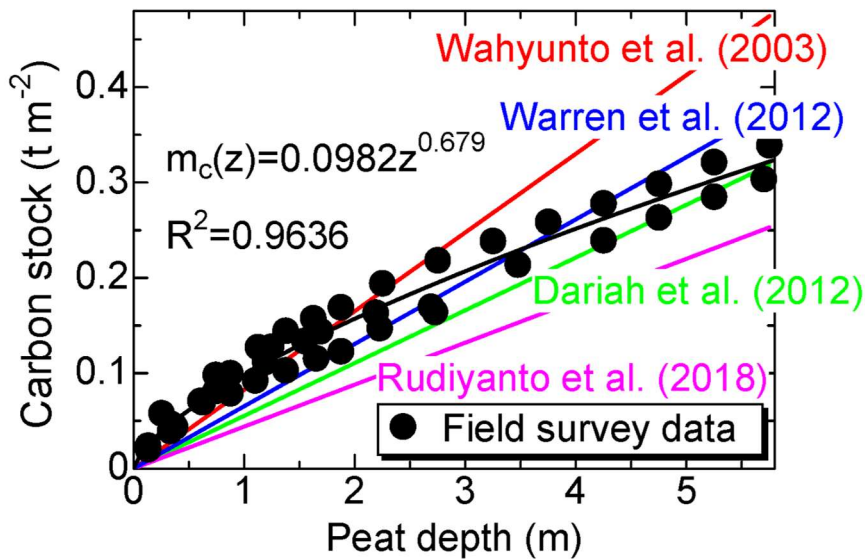


Figure 1722: Cumulative carbon content relative to depth. Literature values sourced from Wahyunto et al., 2003; Dariah et al., 2012; Warren et al., 2012 and Rudiyanto et al., 2018. The literature values from Wahyunto et al., 2003 were calculated using average values for the bulk density and carbon content of Hemic peat. Literature values from Dariah et al., 2012 were calculated using a function to estimate carbon stocks according to the depth of the peat layer. The literature values from Warren et al., 2012 were calculated using a function to estimate carbon stocks from average bulk density. Literature values from Rudiyanto et al., 2018 estimated carbon stocks from average carbon content and bulk density.

4.6 Estimation of POC export to the ocean from lateral degradations

This study quantifies the export of POC to the ocean resulting from coastal erosion and PMMs. We estimated the amount of particulate organic carbon (POC) exported to the ocean due to coastal erosion and peat mass movement events (PMMs). Fig. 18 shows the annual changes in coastal erosion and landslide-affected areas. The estimated amounts of POC flux to the ocean are shown in Fig. 19 and Table 56. The average flux of POCs to the ocean due to coastal erosion along the study research area of Bengkalis Island was estimated to be in the range of 2.06 to 7.60 tC m⁻¹ yr⁻¹. The average POC from the displacement of peat mass caused by PMMs was estimated to be in the range of 1.43 to 5.41 tC m⁻¹, with an average increase of 2.23 tC m⁻¹ from 2010 to 2018.

Such fluxes, particularly from coastal erosion, far exceed those observed in natural river systems. These POC fluxes—particularly from coastal erosion—are substantially higher than typical values reported for natural fluvial systems. The POC flux due to coastal erosion in the studied catchment area (641 ha) was estimated at 1.01–3.74 ktC km⁻² yr⁻¹, which is up to 1,089 times greater than the average POC export from tropical wet regions (0.00343 ktC km⁻² yr⁻¹; Ludwig et al., 1996).

3.74 kt km⁻² yr⁻¹, and from PMMs at 0.70–2.66 kt km⁻². When normalized per unit area, these values are up to 1,089 times greater than the average particulate organic carbon export from tropical humid regions (3.43 tC km⁻² yr⁻¹; Ludwig et al., 1996). This underscores the significant role of coastal erosion in tropical peatland carbon dynamics. This highlights the disproportionately large role that coastal erosion may play in tropical peatland carbon dynamics.

In boreal peatlands, particulate organic carbon (POC) export has been attributed to gully erosion, with reported fluxes ranging from 0.0299 to 0.0319 ktC km⁻² yr⁻¹ (Evans and Lindsay, 2010). In comparison, the POC flux associated with coastal erosion in the present study area is substantially higher, exceeding these boreal values by a factor of approximately 34 to 83. This contrast emphasizes both the spatial disparity in lateral carbon export and the underrecognized role of coastal erosion in tropical systems. Ongoing coastal erosion continuously discharges carbon into the ocean.

In addition to the carbon mass continuously discharged into the ocean due to ongoing coastal erosion, sudden and episodic PMMs contribute to short-term, high-volume discharges of deeply stored peat-derived carbon. On Bengkalis Island, 1 m of coastal erosion resulted in POC loss equivalent to annual CO₂ emissions from 0.41–1.52 ha of degraded peatland. On Bengkalis Island, (Hirano et al., 2014), underscoring the climate relevance of lateral POC flux the POC loss from the erosion of one metre of shoreline was equivalent to the annual CO₂ emissions from 0.41–1.52 ha of drained or logged peatland (Hirano et al., 2014). The POC associated with PMMs was equivalent to emissions from 0.29–1.08 ha per metre of coastline. This indicates that coastal POC fluxes may rival or surpass emissions from degraded inland peatlands. This equivalence suggests that the lateral carbon fluxes from peatland coasts can rival or exceed the emissions typically associated with terrestrial degradation hotspots.

On a peatland coast with an average length of 3,152 m, the estimated POC exported to the ocean due to PMMs ranged from 4.45 to 17.1 ktC, while that from coastal erosion ranged from 6.35 to 23.9 ktC yr⁻¹. Together, these processes constitute a dual mechanism of carbon loss that alters the carbon balance of tropical coastal peatlands. This combination of gradual and abrupt processes indicates a dual mechanism of carbon loss that can significantly alter the carbon balance of tropical coastal peatlands.

POC export from terrestrial to marine environments is primarily driven by riverine transport. A global assessment estimated that approximately 0.38 GtC of organic carbon is exported annually, of which 0.21 GtC is dissolved organic carbon (DOC) and 0.17 GtC is POC (Ludwig et al., 1996). Tropical humid regions contribute approximately 45% of this flux, with POC predominantly reaching the Indian and Pacific Oceans. The total area of tropical humid regions is 23,633,000 km², and the POC flux is approximately 3.43 tC km⁻² yr⁻¹. In contrast, the POC flux from coastal erosion in our study area was between 295 and 1,089 times higher than this regional average, suggesting that coastal peatland degradation may represent a previously underappreciated contributor to oceanic carbon budgets.

When terrestrial organic matter (TOM) enters the ocean, its fate depends on its form. DOC is prone to oxic degradation or photolysis (Mopper et al., 1991), while POC is more likely to settle and accumulate in marine sediments, particularly under

anoxic conditions. Therefore, POC exported by coastal erosion and PMMs may represent a more permanent carbon sink than DOC, especially in low-energy coastal environments with limited sediment resuspension.

The annual precipitation in the study area was 2,013 mm (from 1 January to 31 December 2018January 1–December 31, 2018). Assuming an evapotranspiration rate of 4 mm day⁻¹, the annual discharge from groundwater and rivers was estimated at 553 mm. With an average riverine DOC concentration of 62 mg L⁻¹, the annual DOC export was estimated at approximately 34 tC km⁻² (Yamamoto et al., 2020). Approximately 1% of the POC is leached as DOC during PMMs and coastal erosion (Yamamoto et al., 2020), potentially undergoing oxidation and being released as CO₂.Furthermore, approximately 1% of DOC leaches from POC during PMMs and coastal erosion, potentially being oxidized and released as CO₂ (Yamamoto et al., 2020).

Fig. 20 illustrates the estimated carbon fluxes for the Bengkalis Island watershed. These findings indicate new pathways of carbon export beyond conventional river systems. Exported peat may follow two potential pathways: deposition on the seafloor, functioning as a carbon sink, or accumulation along the shoreline, potentially acting as a source of emissions (Matsuo et al., 2025). Approximately 145,000 km² of global tropical peatlands are located at or below 5 m elevation, making them vulnerable to future sea-level rise (Whittle and Gallego-Sala, 2016). Sea-level rise poses significant threats to low-lying tropical peatlands, particularly in Southeast Asia, including Kalimantan and Sumatra (Whittle and Gallego-Sala, 2016). In addition to sea-level rise, lateral degradation has also been observed across peatlands worldwide (Table 1 and Appendix A). Regarding coastal erosion, the coastline of the study area is retreating at 34 m yr⁻¹ (Kagawa et al., 2017), which is dozens of times faster than erosion rates observed in boreal peatlands (The observed coastal erosion rates in boreal peatlands are 0.56 - 10 m yr⁻¹; Appendix A). In addition to coastal erosion, PMMs represent another form of lateral degradation as shown in this study. Although erosion rates are particularly high here, sea facing peatlands globally may face similar threats. Furthermore, considering that peat decomposition leads to land subsidence, the situation becomes even more critical (Umarhadi et al., 2022). Considering the above situations, tropical peatlands are increasingly threatened by both lateral and vertical degradation processes. However, the fate of the exported peat remains unclear. Clarifying whether exported peat serves as a carbon sink (blue carbon) or a source of carbon emissions is essential for understanding its role in the global carbon cycle.The lateral carbon flow determined in this study (Fig. 20) suggests a novel export route beyond conventional fluvial systems. This coastal mechanism may have particular significance in lowland peat dominated regions where frequent tidal forcing and shoreline retreat expose deeply buried organic carbon to oceanic transport pathways. The combined role of erosion and PMMs thus warrants more detailed investigation, particularly with respect to long term POC burial efficiency, sediment dynamics, and the biogeochemical transformation of exported material.

Notably, in the western part of the study area, field observations and sampling revealed that peat discharged from lateral degradation has redeposited along the peat beach, forming a secondary carbon reservoir (Matsuo et al., 2025). Groundwater samples from this site exhibited high concentrations of dissolved organic carbon (DOC: 379.2 mg C/L) and dissolved organic nitrogen (DON: 7.12 mg N/L), along with strong foaming properties, indicating enhanced microbial activity

1025 and peat decomposition under near neutral pH conditions (pH = 6.91). Experimental data showed that peat particles are physically lifted and floated by surfactants generated during decomposition. At 50% groundwater concentration, 1.9% of peat floated, and the foam volume reached 122% (226 cm³), demonstrating a strong link between peat flotation and groundwater chemistry. Microbial community analysis indicated a high abundance of Actinobacteria, which are known to degrade complex organic matter, particularly in the upper beach redeposition zones (St.1-2). Furthermore, the degree of humification—measured by absorbance at 340 nm—was highest in these beach samples (1.1×10^3), significantly exceeding that at other redeposition sites such as E1 (9.3×10^2) and P2 (7.2×10^2), indicating more advanced decomposition of the redeposited peat. (Matsuo et al., 2025).

1030 Principal component analysis further revealed that foaming properties are strongly correlated with DOC and DON concentrations, suggesting that foaming is a visible indicator of peat decomposition processes. These results challenge the prevailing assumption that peat transported to the ocean is largely inert. Instead, they demonstrate that in tropical coastal settings, redeposited peat may remain biologically active, undergoing continued microbial degradation and potentially contributing to additional CO₂ fluxes. This adds complexity to the coastal carbon budget and underscores the need to include post-depositional peat transformation in carbon cycle assessments (Matsuo et al., 2025).

1035 ————— To fully integrate the contribution of tropical coastal peatlands into global carbon models, future studies should establish long-term observational networks that monitor shoreline change, erosion rates, and POC fluxes at high temporal and spatial resolution. In addition, interdisciplinary approaches combining geomorphological, biogeochemical, and hydrodynamic modeling are essential to accurately represent lateral carbon flows. Incorporating such coastal carbon processes into Earth system models will improve predictions of land-ocean carbon fluxes and enhance our understanding of feedback between coastal degradation and the global climate system.

1040 Future work should address key uncertainties, such as: (1) the proportion of exported POC that undergoes burial versus remineralization; (2) the decomposition rates of exposed deep peat at eroding cliff faces; (3) the hydrodynamic factors controlling POC dispersion and accumulation in nearshore environments; and (4) the reactivity and long-term fate of redeposited peat along tropical coasts.

1045 This study is one of the first cases to quantify POC fluxes from tropical coastal peatlands driven by both coastal erosion and PMMs. This study is among the first to quantify particulate organic carbon fluxes from tropical coastal peatlands due to both progressive erosion and sudden peat mass movements. By combining erosion data with microbial and biochemical evidence from redeposition zones, this study provides a more comprehensive picture of lateral carbon dynamics in tropical coastal peatlands. These findings provide a foundation for incorporating coastal carbon export processes into peatland carbon budgets and highlight the urgency of protecting vulnerable shoreline peatlands from further degradation. We estimated the amount of POC exported to the ocean due to coastal erosion and PMMs. Fig. 23 shows the annual changes in coastal erosion and landslide-affected areas. The estimated amounts of POC flux to the ocean are shown in Fig. 24 and Table 5. The average flux of POCs to the ocean due to coastal erosion along the research area of Bengkalis Island was estimated to be in the range of 2.06 to 7.60 tC m⁻¹ yr⁻¹. The average POC from the displacement of the peat mass caused by PMMs along the study area

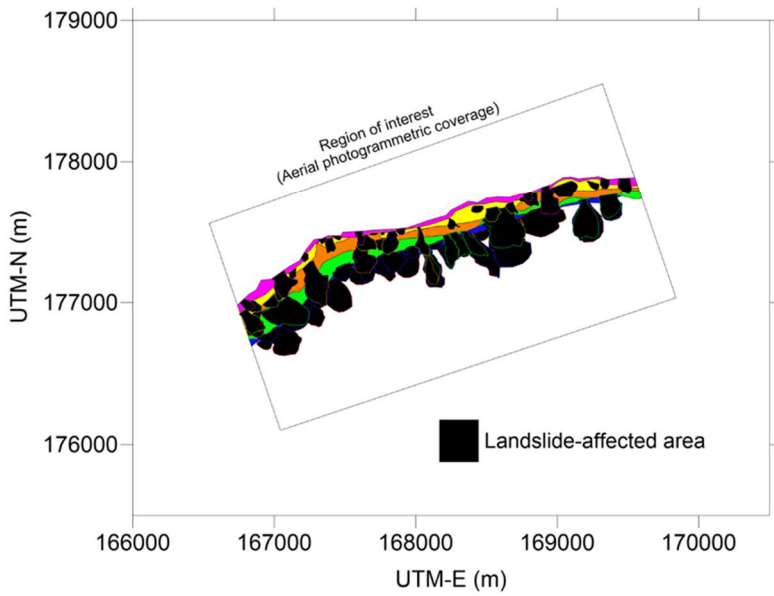
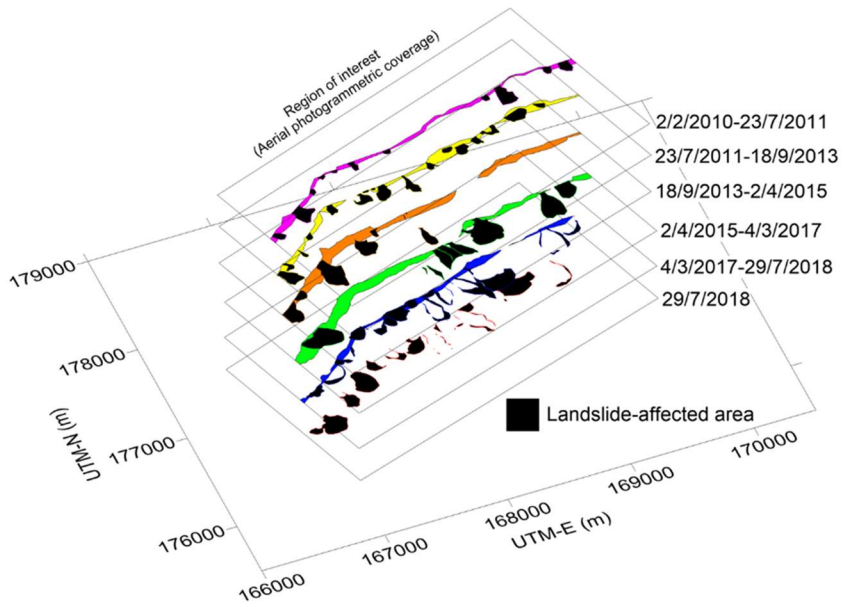
1050

1055 of Bengkalis Island was estimated to be in the range of 1.43 to 5.41 tC m⁻¹, with an average increase of 2.23 tC m⁻¹ from 2010 to 2018. In addition to the carbon mass continuously discharged into the ocean due to ongoing coastal erosion, an additional carbon mass is released into the ocean because of sudden PMMs. The POC fluxes from the coastal erosion and the PMMs were calculated for the catchment area (641 ha) of the target coastline (3,152 m) and found that the coastal erosion was 1.01–3.74 kt km⁻² yr⁻¹, and the PMMs were 0.70–2.66 kt km⁻².

1060 Carbon dioxide emissions from drained or logged peatlands can reach 499 g m⁻² yr⁻¹ (Hirano et al., 2014). To put this carbon footprint in perspective, on Bengkalis Island, POC loss from erosion of one metre of shoreline is equivalent to the annual carbon dioxide emissions from 0.41–1.52 ha of drained or cut peatland. And the POC from the displacement of the peat mass caused by PMMs on Bengkalis Island in our study is equivalent to the carbon emissions produced over a year of 0.29–1.08 ha of drained or logged peatlands, measured as carbon dioxide per metre of coastline. On a peatland coast with an average
1065 length of 3,152 m, the amount of POC exported to the ocean due to PMMs were estimated to range from 4.45 ktC to 17.1 ktC, while the POC exported due to coastal erosion was estimated to range from 6.35 ktC yr⁻¹ to 23.9 ktC yr⁻¹.

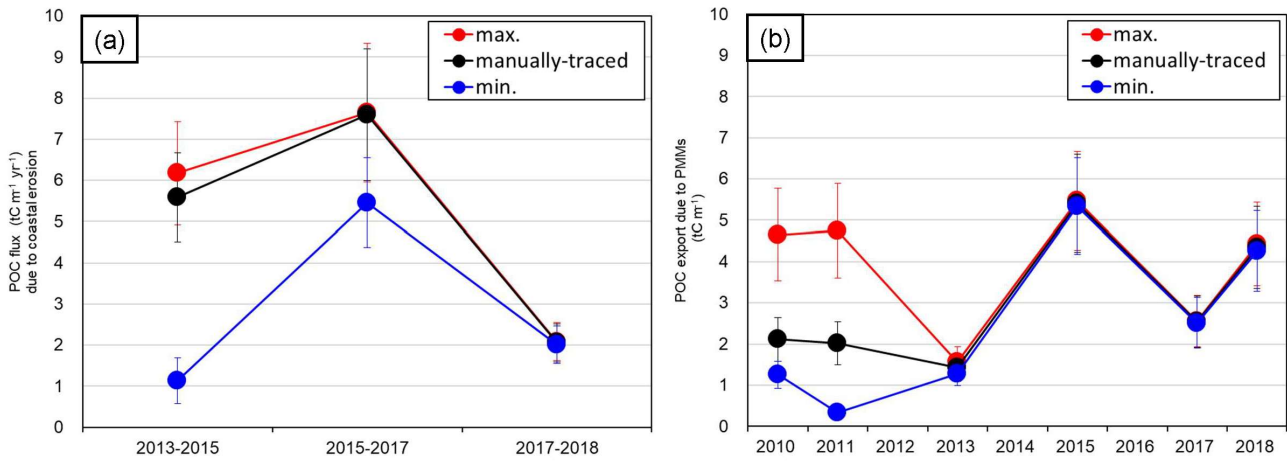
The export of POC from terrestrial to marine environments is primarily driven by riverine transport. A study investigating the relationship between climate, biota, and geomorphological patterns in major river basins worldwide and their impact on organic carbon fluxes predicted that approximately 0.38 GtC of organic carbon are exported to the ocean annually.
1070 Of this, about 0.21 GtC are in dissolved form, while approximately 0.17 GtC are in particulate form (Ludwig et al., 1996). Notably, organic carbon export from tropical humid regions accounts for approximately 45% of the total, with most of the dissolved organic carbon entering the Atlantic Ocean and most particulate organic carbon being transported to the Indian and Pacific Oceans (Ludwig et al., 1996). According to Ludwig et al., 1996, the total area of tropical humid regions is 23,633,000 km² and the POC discharge to the oceans was estimated to be 81.09 TgC yr⁻¹. Therefore this corresponds to be a POC flux of
1075 3.43 tC km⁻² yr⁻¹. Comparing to this case, POC flux due to the coastal erosion in the watershed in studied region of 641 ha (Fig. 4) was 295 to 1,089 times greater than the value.

When terrestrial organic matter (TOM) particulate discharges into the ocean, much of it is likely to settle in seawater and accumulate in coastal seabed sediments for decades to centuries. In contrast, dissolved TOM undergoes oxic biodegradation or photolytic decomposition when it rinses oxygen rich surface waters (Mopper et al., 1991). The annual
1080 precipitation in the study area was 2,013 mm (from 1 January to 31 December 2018). Assuming an estimated evapotranspiration rate of 4 mm day⁻¹ in tropical peatlands, the annual discharge from groundwater and rivers is calculated to be 553 mm. Given a riverine DOC concentration of 62 mg L⁻¹, the estimated annual DOC export is approximately 34 tC km⁻² (Yamamoto et al., 2020). And approximately 1% of DOC leaches from POC and rinses into the ocean due to PMM or coastal erosion (Yamamoto et al., 2020). Leached DOC can be released as carbon dioxide through oxidative or photolytic decomposition. The carbon load
1085 flow in the study area, as determined in this study, is shown in Fig. 25. It is necessary to investigate the fate of deep peat when it is exposed to the atmosphere due to PMMs and erosion or transported into the ocean, including whether it remains suspended at the surface or accumulates on the seafloor. This lateral carbon export along the tropical peatland coast indicates a new route of carbon export to the ocean in addition to the common riverine export of POC to the ocean.



1090

Figure 1823: History of coastal erosion and landslide-affected area within the region of interest (68 ha). This figure shows that the coastal erosion and peat mass movements occurred by turn and the landslide-affected area had been expanding towards the hinterland.



1095

Figure 1924: Time series of (a) estimated POC fluxes due to coastal erosion and (b) estimated POC export due to displacement of peat mass caused by PMMs for observation moment. The average POC flux of POC to the ocean was estimated to be 2.06 to 7.60 $tC m^{-1} yr^{-1}$ by coastal erosion and 1.43 to 5.41 $tC m^{-1}$ from PMMs. The error bars indicate the standard deviation (SD).

1100

Table 56: The landslide-affected area and the estimated volume of the eroded peat by the events of coastal erosion and peat mass movements in each period. Changes in time in the estimated amount of POC from peat mass displacement caused by PMMs and from flows due to coastal erosion. SD indicates the standard deviation of the POC flux calculated using the results of five patterns of cumulative carbon content calculations, including values from the literature. Where period (a) is 2/2/2010 to 23/7/2011, period (b) is 23/7/2011 to 18/9/2013, period (c) is 18/9/2013 to 2/4/2015, period (d) is 2/4/2015 to 4/3/2017 and period (e) is 4/3/2017 to 29/7/2018.

Period	Term	Coastline	Coastal erosion										
			Area			Volume			POC flux				
			min.	manually-traced	max.	min.	manually-traced	max.	min.	manually-traced	max.		
			Average \pm SD (<i>n</i> =5)										
days	m	ha	Mm ³	Mm ³	Mm ³	tC m ⁻¹ yr ⁻¹							
(a)	2010-2011	536	3,096	1.8	9.7	20.0	-	-	-	-	-	-	-
(b)	2011-2013	788	3,313	8.2	13.0	18.6	-	-	-	-	-	-	-
(c)	2013-2015	561	3,120	16.8	17.0	18.8	0.24	0.43	0.53	1.13 \pm 0.56	5.59 \pm 1.08	6.17 \pm 1.27	
(d)	2015-2017	702	3,162	18.4	18.5	18.8	0.64	0.75	0.80	5.46 \pm 1.09	7.60 \pm 1.60	7.65 \pm 1.69	
(e)	2017-2018	512	3,140	9.6	9.8	9.9	0.130	0.136	0.138	2.02 \pm 0.45	2.06 \pm 0.46	2.09 \pm 0.47	
Total		3099		54.8	68.0	86.1	1.01	1.32	1.47				

Date	Coastline	PMMs						POC exported rate per unit length		
		Area			Volume			Average \pm SD (<i>n</i> =5)		
		min.	manually-traced	max.	min.	manually-traced	max.	min.	manually-traced	max.
		tC m ⁻¹								
m	ha	Mm ³	Mm ³	Mm ³	Mm ³	Mm ³				
2/2/2010	3,096	4.8	7.4	14.7	0.06	0.10	0.22	1.25 \pm 0.33	2.11 \pm 0.53	4.65 \pm 1.12
23/7/2011	3,313	3.9	11.8	24.1	0.02	0.14	0.34	0.33 \pm 0.13	2.02 \pm 0.52	4.74 \pm 1.15
18/9/2013	3,120	7.8	8.8	9.8	0.14	0.15	0.16	1.28 \pm 0.29	1.43 \pm 0.33	1.57 \pm 0.36
2/4/2015	3,162	21.0	21.3	21.6	0.395	0.400	0.404	5.34 \pm 1.17	5.41 \pm 1.18	5.47 \pm 1.20
4/3/2017	3,140	16.0	16.2	16.3	0.228	0.230	0.232	2.51 \pm 0.61	2.54 \pm 0.62	2.56 \pm 0.62
29/7/2018	3,085	16.5	16.9	17.3	0.275	0.280	0.285	4.26 \pm 0.98	4.34 \pm 1.00	4.42 \pm 1.02
Total		70.0	82.4	103.8	1.12	1.30	1.64			

1105

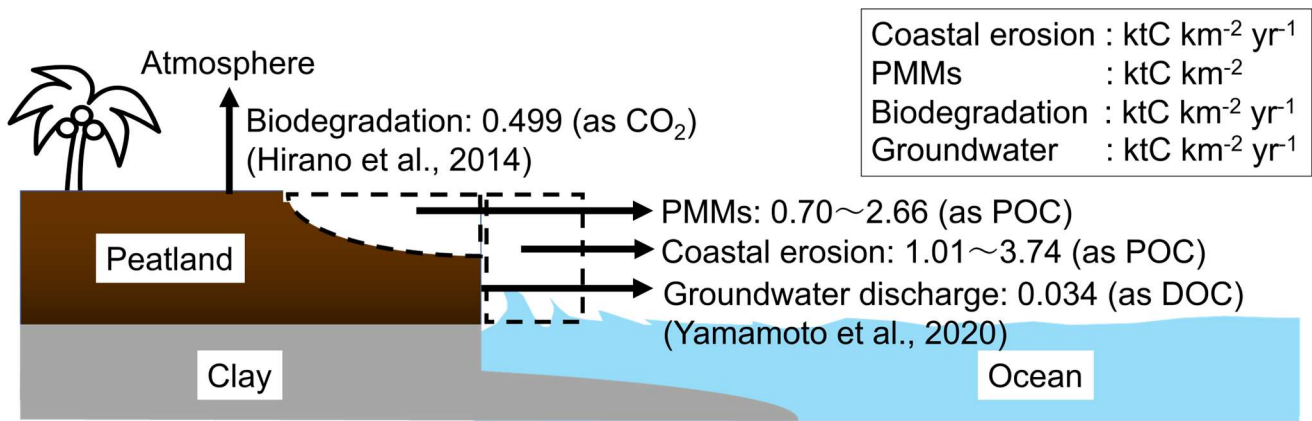


Figure 205: Estimated carbon flux of the watershed in the Bengkalis Island. Biodegradation was referred to Hirano et al., 2014. Groundwater discharge was referred to Yamamoto et al., 2020.

1110

5 Conclusions

In this study, we have identified the conditions under which a chain of coastal erosion and peat mass movement events (PMMs) occur on tropical peatland islands with peat-formed coasts, and we have estimated the export of POCs to the ocean resulting from these processes. In coastal areas of tropical peatlands, coastal erosion promoted peat mass movements and vice versa.

1115

This chain of events of coastal erosion and peat mass movements proceeds as follows; When peat mass movement events first occur on a coastal peatland, peat is exported from the coast into the ocean, forming a peaty debris fan. Subsequent erosion causes the peaty debris fan to disappear, leaving the peat cliffs and the area affected by landslides. Long-term progression of coastal erosions has affected carbon export to marine environments from the peatland. The carbon export rate due to coastal erosion in the study watershed (641 ha) due to coastal erosion contributed to an annual carbon export of 1.01-3.74 ktC km² yr⁻¹, which was estimated as 2.0-7.5 times higher than the carbon emissions due to from peat biodegradation of peatland. The rates of coastal erosion were affected by the land cover. The coastal erosion rates of oil palm plantations exceeded those of mangrove or peat swamp forests by more than double. The relationship between significant wave height and maximum wind speed indicates that stronger winds correspond to higher wave heights, emphasising the role of wind-induced wave activity in coastal processes, contribute significantly to the acceleration of coastal erosion. These findings suggest that elevated wave heights, driven by seasonal winds, may contribute significantly to the acceleration of coastal erosion.

120

125

The POC fluxes due to coastal erosion are estimated to average between 2.06 and 7.60 tC m⁻¹ yr⁻¹. PMMs also resulted in substantial peat loss and coastal geomorphic changes. The export of peat into the marine environment underscores the significant impact of these collapses on carbon fluxes and coastal dynamics. Heavy precipitation played a crucial role in the triggering of PMMs. In the case of December 2014, a weir breach event likely initiated the collapse of the lower reach of the peatland. The POC of the displacement of the peat mass caused by PMMs is estimated to average between 1.43 and 5.41 tC

130

~~m⁻¹. The carbon export rate in the study watershed (641 ha) due to coastal erosion contributed to an annual carbon export of 1.01–3.74 ktC km⁻² yr⁻¹, which is 2.0–7.5 times higher than the carbon emissions from peat biodegradation. While the carbon export rate through PMMs contributed to surplus carbon export, depending on the frequency of the PMMs, of 0.70–2.66 ktC km⁻². On a peatland coast with an average length of 3,152 m, the amount of additional carbon export POC exported to the ocean due to PMMs was estimated to range from 4.45 to 17.1 ktC, while it ranged from the POC exported due to coastal erosion was estimated to range from 6.35 to 23.9 ktC yr⁻¹ due to coastal erosion. Compared to the typical POC flux from tropical wet humid regions via riverine transport, these lateral carbon fluxes in this watershed (641 ha) correspond to approximately 295 to 1,089 times greater. Consequently, these lateral carbon exports on tropical peatland coasts add another route represent a new route for carbon export to the ocean, in addition to general POC discharges from rivers, in general. However, Further studies need to clarify, the fate of exported peat particles in marine environment to the oceans and needs to be clarified. It is still unclear emission of the carbon dioxide from whether the fate of deep layer of the peat is exposed peat cliff formed by to the atmosphere due to coastal erosion, to PMMs, erosion, and transport to the ocean, including whether it remains suspended at the surface or accumulates on the seafloor.~~

Appendix A: The global distribution of peatlands

~~Peatlands are distributed across subarctic, arctic, and tropical regions (Fig. A1). Throughout the Holocene, they have functioned as persistent carbon sinks. Globally, peatlands are estimated to have sequestered more than 600 GtC at a rate exceeding 5 GtC per century (Kleinen et al., 2010; Yu, 2011).~~

~~The total peatland area is estimated to range from 3.97 to 4.26 million km², accounting for approximately 3.05% to 3.28% of the Earth's land surface (Osaki and Tsuji, 2016; Ministry of the Environment, 2002). Despite this limited spatial extent, peatlands are estimated to store about 6% of the global soil carbon stock (Page et al., 2011; Scharlemann et al., 2014). Peatlands are distributed across subarctic, arctic, and tropical regions (Fig. A1). Throughout the Holocene, they have acted as sustainable carbon sinks, sequestering more than 600 GtC at a rate exceeding 5 GtC per century (Kleinen et al., 2010; Yu, 2011). The global peatland area is estimated between 3,969,831 and 4,258,068 km², representing approximately 3.05% to 3.28% of the Earth's total land area (Osaki and Tsuji, 2016; Ministry of the Environment, 2002). Despite their small area, peatlands store approximately 6% of the Earth's total soil carbon stock (Page et al., 2011; Scharlemann et al., 2014).~~

1. Bykovsky Peninsula, Siberia (Fig. A1a)

~~Annual erosion rates vary significantly on interannual and decadal scales (Lantuit et al., 2011). Sediment accumulation can reach 5.00 m yr⁻¹, with coastal retreat rates up to 10.00 m yr⁻¹. From 1986–2006, the average erosion rate was 1.09 m yr⁻¹.~~

with a peak of 2.06 m yr⁻¹ from 1975–1981. Storms (≥ 10 m s⁻¹ for ≥ 6 hrs) occurred on average 13.6 times/year between 1958 and 2006, but erosion did not correlate directly with storm frequency due to a "lag effect" (Lantuit and Pollard, 2008).

2. Beaufort Sea Coastline (Fig. A1b)

Yunker et al. (1991) divided the coastline from Cape Dalhousie to the Alaska border into 776 segments, calculating coastal retreat and estimating peat flux into the sea by multiplying retreat rates with peat thickness.

3. Elson Lagoon, Alaska (Fig. A1c)

From 1949 to 2000, retreat rates increased from 0.56 m yr⁻¹ (1948–1979) to 0.86 m yr⁻¹ (1979–2000), resulting in a 47% increase and 28 ha land loss. Erosion is restricted to the ice-free season (3–4 months yr⁻¹). Regional retreat rates range from 2 to 6 m yr⁻¹, with maxima exceeding 10 m yr⁻¹ (Rachold et al., 2002).

4. Baltic Sea Coastal Peatlands (Fig. A1d)

Coastal low-lying peatlands cover ~ 0.16 – 0.2 km² (Lehfeldt and Milbradt, 2000). Coastal erosion and storm abrasion have exposed peat layers by removing overlying sand. Saltwater intrusion affects $\sim 1,800$ km² of wetlands (Sterr, 2008), and ~ 3 km of wetland has been lost in the southern Baltic Sea since peat formation began. Coastal wetlands face multiple stressors, including sea-level rise, flooding, submergence, and infrastructure restrictions on inland migration (Nicholls and Cazenave, 2010; Wong et al., 2014; Chambers et al., 2019).

5. Amazonian Peatlands and Coastal Erosion (Fig. A1e)

Research in Amazonian peatlands began in the 1950s and has expanded significantly since 2009, shifting from carbon dynamics to degradation and conservation (Malpica-Piñeros et al., 2024). The Amazon Basin spans nine countries, with most peatland studies concentrated in Peru. High-altitude peatlands are found in the Andes, Guiana Shield, and Brazilian Shield. In Guiana, coastal erosion such as beach retreat has been observed (Chevallier et al., 2023).

6. Boreal Peatlands and Peatland Failures (Fig. A1f)

Peat mass movements (PMMs) in boreal regions include bog bursts, bog slides, and peat flows (Dykes and Warburton, 2007). Common triggers include heavy rainfall, drainage, and snowmelt. Failures have been documented since the 16th century in northern England and Ireland (e.g., Bowes et al., 1960; Warburton et al., 2004; Dykes and Jemmings., 2011). Most failures occur on 2–3 m thick peat over slopes of 4°–8°, but steeper failures also occur. Consequences include fish kills (McCahon et al., 1987) and drainage disruptions (Alexander et al., 1986).

7. Coastal Wetland Vulnerability and Degradation (Fig. A1g)

195 According to Chambers et al., 2019, low-lying coastal wetlands are undergoing degradation due to combined climatic and anthropogenic stressors, resulting in reduced ecological health and shrinking spatial extent. These wetlands, located within the intertidal ecotone between marine and terrestrial environments, face multi-directional threats.

8. Tropical Peatland Failures (Fig. A1h)

200 Documented cases of PMMs in tropical peatlands are rare. The only known cases include: A suspected landslide on the Tutoh River, Malaysia in 1966 (Wilford, 1966). Fig. 1 shows the global distribution of peatlands. These peatlands are distributed across subarctic, arctic, and tropical regions. Throughout the Holocene, peatlands have acted as sustainable carbon sinks, sequestering more than 600 GtC at an average rate exceeding 5 GtC per century (Kleinen et al., 2010; Yu, 2011). The global peatland area has been estimated to range from a minimum of 3,969,831 km² to a maximum of 4,258,068 km², with an intermediate estimate of 3,985,000 km² (Osaki and Tsuji, 2016). The Earth's land area is approximately 13 billion ha (Ministry of the Environment White Paper, 2002), with peatlands accounting for 3.05% to 3.28% of the total land area. Although peatlands cover only about 3% of the Earth's land area, they store approximately 6% of the Earth's total carbon (Page et al., 2011; Scharlemann et al., 2014). 006) using aerial photographs and satellite imagery, alongside in situ meteorological and tidal data to analyse erosion mechanisms (Lantuit et al., 2011). The results reveal that annual erosion rates exhibit significant interannual and decadal-scale variability. At the Bykovsky Peninsula, sediment accumulation rates reach up to 5.00 m yr⁻¹ in certain areas, while the most affected locations experience coastal retreat at rates of up to 10.00 m yr⁻¹. Specifically, the site recorded an average erosion rate of 1.09 m yr⁻¹ between 1986 and 2006, while a higher rate of 2.06 m yr⁻¹ was observed from 1975 to 1981. The local coastal morphology varies, ranging from relatively stable vegetated slopes to nearly vertical cliffs, with some areas featuring escarpments up to 45 m in height. The geological composition consists of silt, sand, peat, and complex deposits from the Holocene period. Focusing on the summer to autumn period in the Arctic (1 June to 15 October, approximately 4.5 per 30 days), storms were defined as events where wind speeds reached 10 m s⁻¹ or higher for at least six hours. Based on this definition, 665 storms were recorded between 1958 and 2006, corresponding to an average annual occurrence of approximately 13.6 storms. While storms are often assumed to play a significant role in coastal erosion, no direct correlation has been demonstrated. In permafrost dominated coastal regions, a "lag effect" (Lantuit and Pollard, 2008) has been identified, where the peak of coastal erosion does not coincide with the peak of storm activity. Yunker et al., 1991 divided the coastline along the Beaufort Sea from Cape Dalhousie to the Alaska border into 776 coastal segments. For each segment, they calculated the rate of coastal retreat and multiplied it by the thickness of the peat layer to estimate the annual flux of peat material into the Beaufort Sea (Fig. 1b).

225 At Elson Lagoon, Alaska, a time series of coastal erosion rates along a 10.8 km stretch of the lagoon shoreline was determined by georeferencing aerial photographs and high-resolution satellite imagery from 1949 to 2000 (Fig. 1c). The coastline retreated at an average rate of 0.56 m yr⁻¹ from 1948 to 1979, and this rate increased by 47% to 0.86 m yr⁻¹ from 1979 to 2000. During this latter period, a total of 28 hectares of land was lost. In the Arctic, coastal erosion is restricted to the ice-free period of approximately 3–4 months yr⁻¹. Along some sections of the Arctic coastline, erosion rates exceeding 10 m yr⁻¹ have been

recorded, while the regional average ranges from 2 to 6 m yr⁻¹ (Rachold et al., 2002). Observations of coastal retreat rates and coastal processes along the Barrow coastline, Alaska, began in the late 1940s and continued into the early 1980s (MacCarthy 1953; Harper 1978; Hume and Schalk 1967; Hume et al., 1972). Harper, 1978 reported that the coastline between Barrow Bay and Peard Bay (a 75 km stretch) experienced an average retreat rate of 0.31 m yr⁻¹ from 1949 to 1976. In the Barrow region, permafrost extends to a maximum depth of approximately 400 m, with a thin, peaty surface layer averaging less than 30 cm in thickness (Brown et al., 2003).

The coastal low-lying peatlands along the southern Baltic Sea are estimated to cover an area of approximately 0.16–0.2 km² (Fig. 1d). The offshore boundary of the former peatland roughly coincides with the offshore limit of a dynamic, coast-parallel longshore bar, with peat deposits eroded seaward. Globally, soft coastlines are increasingly affected by adverse processes such as erosion, flooding, and submergence. Sea-level rise and climate change will further intensify the pressure on coastal urban areas and ecosystems, shaping their future development (Vestergaard, 1997; Furmanczyk and Dudzinska-Nowak, 2009).

Ongoing coastal dynamic processes, such as wave- and current-induced erosion, sediment transport, and accumulation, have significantly influenced coastline evolution (Lehfeldt and Milbradt, 2000). These processes have led to coastline displacement through land loss or land reclamation, thereby altering the spatial extent of coastal ecosystems and habitats. Among the most vulnerable coastal areas are low-lying coastal wetlands, which face severe threats from saltwater intrusion, erosion, and submergence (Vestergaard, 1997; Nicholls and Cazenave, 2010; Wong et al., 2014). Along the Baltic Sea, approximately 1,800 km² of coastal wetlands are affected by saltwater intrusion (Sterr, 2008). In the southern Baltic Sea, coastal erosion has resulted in the loss of approximately 3 km of wetland in an eastward direction since the onset of peatland formation. This has led to peat layer exposure along the beach, where wave erosion occurs along the seaward margin of the wetland following the abrasion of overlying sand layers by storm events.

According to Chambers et al., 2019, the degradation of low-lying coastal wetlands is driven by stressors associated with global climate change and anthropogenic disturbance, leading to losses in both their health and spatial extent. Coastal wetlands are highly vulnerable to sea-level rise, with projections estimating a 22–30% global areal loss by 2100 (Nicholls et al., 1999; IPCC, 2007). Occupying the intertidal ecotone between marine and terrestrial environments, coastal wetlands experience loss from multiple directions. On the seaward edge, storm events, increasing water depth, wave height, and wave power may accelerate erosion (Schwimmer, 2001; Mariotti and Fagherazzi, 2010), while drowning occurs when relative sea-level rise outpaces soil surface elevation gains (Krauss et al., 2010). Additionally, steep topography and human infrastructure may restrict wetlands from migrating upslope, limiting their ability to maintain an optimal elevation relative to sea level. This constraint may result in habitat loss or conversion (Day et al., 2008; Hussein, 2009). Natural wetland degradation drivers include land subsidence, sea-level rise, droughts, hurricanes, tsunamis, storms, erosion, and biological impacts (Dugan, 1993).

Malpica-Piñeros et al., 2024 reviewed research activities on Amazonian peatlands, which began with ecological studies in the 1950s. A substantial thematic expansion has been observed since 2009, initially focusing on carbon accumulation and greenhouse gas fluxes, and later shifting toward degradation and conservation after 2017. This trend has been accompanied by a spatial bias favouring the Peruvian lowlands. To date, scientific attention remains limited for the peatlands of western Brazil,

the Bolivian lowlands, and the Guianas. Most research on Amazonian peatlands has been conducted by international institutions, but recent years have seen a growing contribution from local research institutes and groups. Amazonia is home to the world's largest tropical rainforest and river system, containing 10% of global species diversity (Charity et al., 2016). Spanning nine countries in tropical South America, the Amazon Basin is primarily situated in Brazil (59%), with the remainder distributed across Bolivia (BOL), Colombia (COL), Ecuador (ECU), French Guiana (GUF), Guyana (GUY), Peru (PER), Suriname (SUR), and Venezuela (VEN) (Charity et al., 2016). High-altitude peatland landscapes in the Amazon Basin are found across three major regions: the lower Andean Cordillera, the Guiana Shield, and the Brazilian Shield, at elevations between 500 and 1500 m. In Guiana, beach erosion has been reported (Chevallier et al., 2023), indicating a potential for similar coastal processes in this study's context (Fig. 1e).

In boreal peatlands, gully formation due to fluvial erosion is a common process of blanket bog peatland erosion (Evans and Warburton, 2005). In addition to fluvial erosion, peatland failures in boreal peatlands are triggered by snowmelt, rainfall, drainage construction, and peat extraction. Peatland failures have been described using various terms, including peat landslides, bog bursts, and peat failures. However, in Dykes et al., 2007 classified previously documented peatland failures under the broader category of peat mass movements (Fig. 1f).

Numerous peatland failures have been reported in northern peatlands such as northern England and Ireland since the 16th century (Bowes et al., 1960; Crisp et al., 1964; Kirk et al., 2001; Mills et al., 2002; Warburton et al., 2004; Dykes et al., 2006; Boylan et al., 2008; Dykes et al., 2011). Peatland failures in northern peatlands are often triggered by heavy or prolonged rainfall (~90 mm in 90 min) (Dykes et al., 2007b). Most failures occur on thin (~2–3 m thick) blanket bog slopes, sometimes involving tens to hundreds of thousands of cubic meters of peat (Dykes et al., 2007). Reported consequences of peatland failures include mass fish kills in river systems (McCahon et al., 1987; Wilson et al., 1996) and disruptions to natural drainage systems (Alexander et al., 1986; Coxon et al., 1989). Peatland failures have been classified based on failure block morphology, soil composition, post-failure topography (e.g., secondary features such as tension cracks), failure mechanisms, peat mass displacement velocity, and moisture content of the failed slope (Dykes et al., 2007). According to this classification, peatland failures are categorized into bog burst, bog flow, bog slide, peat slide, peaty debris slide, and peat flow (Dykes et al., 2007). According to Boylan et al., 2008, 70 peat slope failures have been reported in Ireland over the past 400 years, although the actual number of occurrences is believed to be significantly higher. Reported cases have increased since 1800, with some failures reaching volumes of up to 5,000,000 m³, although most are small-scale. A negative correlation between peat thickness and slope angle has been observed, with most failures occurring on slopes between 4° and 8°. However, failures can also occur on steeper slopes (>20°) if the peat layer is thinner, often involving interactions with the underlying mineral soil. Failure zones range from hundreds of meters to several kilometres, and larger failure volumes tend to result in longer peat mass displacement distances.

In tropical peatlands, reports of peat mass movements are significantly fewer compared to boreal peatlands. Aside from a recent case on Bengkalis Island (Yamamoto et al., 2019), the only previously documented instance was a suspected peat landslide along the Tutoh River, Malaysia, in 1966 (Wilford, 1966) (Fig. 1h). On Bengkalis Island, coastal landslide has

occurred that closely resemble bog bursts observed in boreal peatlands (Dykes et al., 2007). The residual landforms of these bog bursts exhibit crack patterns like those described in progressive failure, a mechanism well known in rock mass collapse, as defined by Bjerrum, 1967.

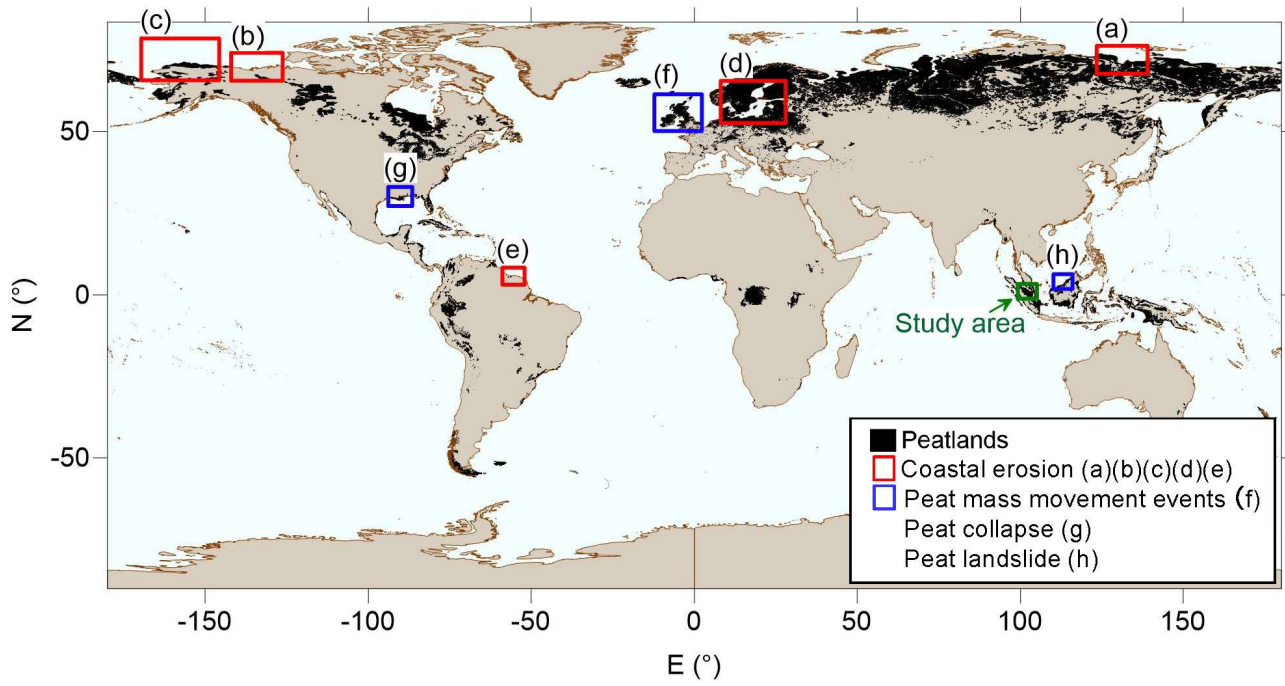
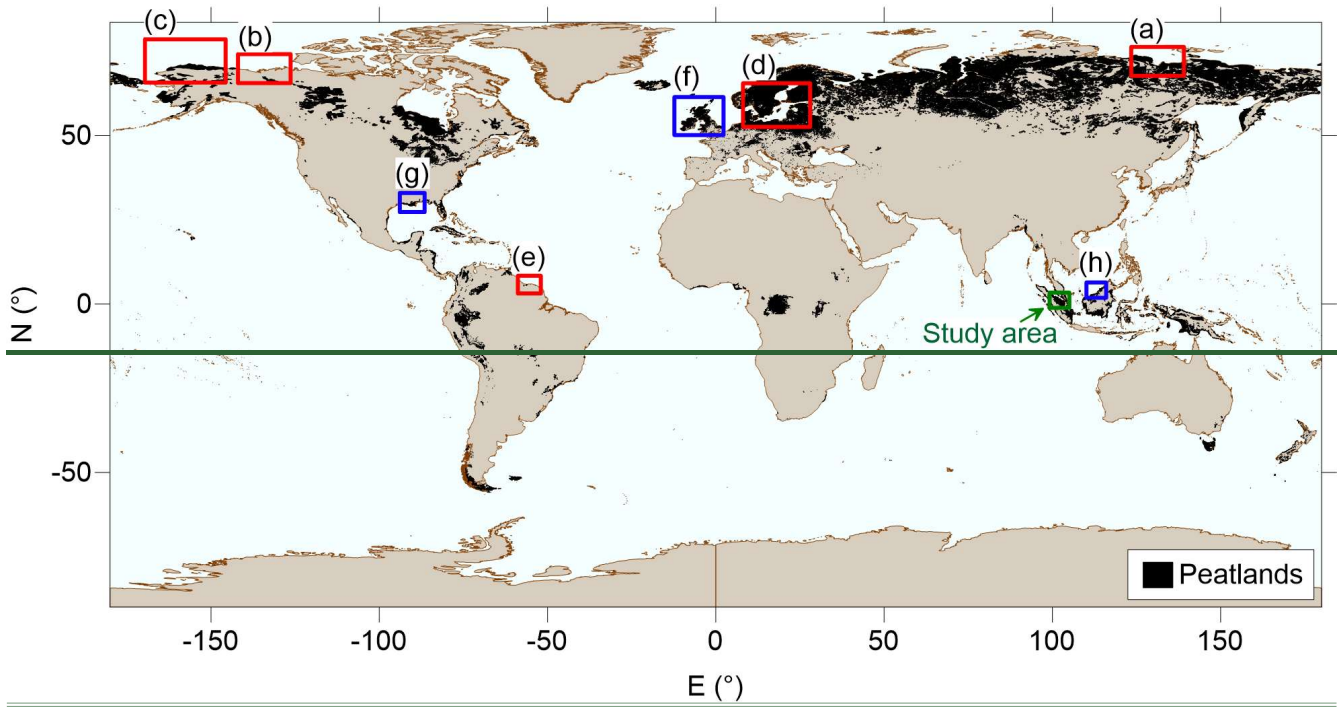


Figure A1: Global Distribution of the lateral degradation in Peatlands (Based on data from the Global Peatland Database / Greifswald Mire Centre (2024)).

1305

Appendix B: Time series of NDVI data viewed and analysed in Sentinel hub EO browser

EO Browser was utilized as a web-based platform for processing remote sensing data in a cloud computing environment. Sentinel images were obtained from Sentinel Hub, which is connected to EO Browser via API, and statistical analysis of the Normalized Difference Vegetation Index (NDVI) was conducted within EO Browser. The procedure for NDVI statistical analysis in EO Browser is as follows: First, the acquisition period for the Sentinel images was selected, and polygons from a KML file created in a GIS environment were imported into EO Browser. The statistical analysis of NDVI allowed for the calculation of average values within the selected polygons and the assessment of temporal changes over the specified period. To minimize the impact of cloud cover, the analysis was conducted with cloud coverage set to 0%. Since erroneous data were occasionally included, the exported CSV files were reviewed, and any erroneous data were manually removed.

Appendix C: Relationship between NDVI and vegetation cover

Time-series changes in NDVI were analyzed using Landsat8, while Sentinel-2 imagery was employed to examine the relationship between NDVI and vegetation cover. Consequently, we first established the relationship between NDVI values from Landsat8 and Sentinel-2. An oil palm plantation was selected as the target for comparison (Fig. 34c). To determine whether NDVI variation is related to vegetation coverage, VARI (Visible Atmospherically Resistant Index) images were generated from UAV aerial photogrammetric data acquired on 4 March 2017. The VARI images were binarized using a threshold of 0, and a scatter diagram was constructed to compare the binarized VARI values with the NDVI data. Pixel sizes were matched to facilitate the correlation analysis between vegetation coverage and NDVI. NDVI (Landsat 8), NDVI (Sentinel-2) and VARI were calculated using Eq. (16), Eq. (17) and Eq. (18).

$$NDVI = \frac{B5 - B4}{B5 + B4} \quad (16)$$

$$NDVI = \frac{B8 - B4}{B8 + B4} \quad (17)$$

$$VARI = \frac{G - R}{G + R - B} \quad (18)$$

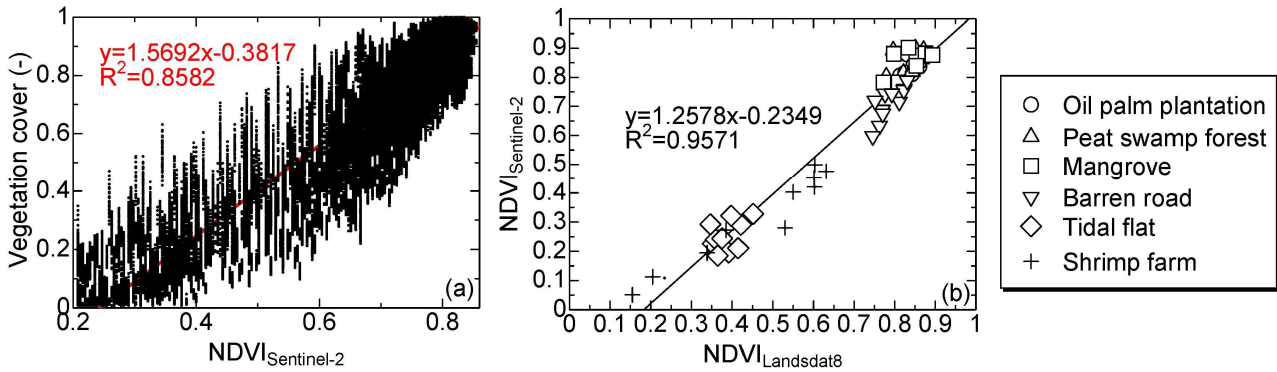
Where $B5$ represents the NIR with 30 m resolution (wavelength: 850-880 nm); $B4$ represents the red band with 30 m resolution (wavelength: 640-670 nm); $B8$ represents the NIR with 10 m resolution (wavelength: 842 nm); $B4$ represents the red band with 10 m resolution (wavelength: 665 nm). G represents the green band; R represents the red band; B represents the blue band.

Changes in NDVI and vegetation cover were plotted as a time series to highlight where the vegetation became discontinuous. Fig. 34a illustrates the relationship between vegetation cover and NDVI which exhibits a clear correlation.

1335 as expressed by Eq. (19) (with VC representing vegetation cover and $NDVI_{Sentinel-2}$ representing NDVI of Sentinel-2).
 Additionally, a strong correlation was observed between the NDVI values from Landsat 8 and Sentinel-2; this relationship is
 shown in Fig. CB2b and expressed by Eq. (20), where x is the $NDVI_{Landsat8}$ from Landsat 8 and $NDVI_{Sentinel-2}$ is that from
 Sentinel-2.

$$VC = 1.5692NDVI_{Sentinel-2} - 0.3817 \quad (R^2 = 0.8582) \quad (19)$$

$$1340 \quad NDVI_{Sentinel-2} = 1.2578NDVI_{Landsat8} - 0.2349 \quad (R^2 = 0.9571) \quad (20)$$



1345 **Figure BC1: (a): Relationship between Sentinel-2 NDVI and vegetation cover (b): Relationship between Landsat 8 NDVI and Sentinel-2 NDVI, and Both figures show a linear relationship.**

Appendix D: Land cover classification using machine learning

To extract bare land from oil palm plantations in satellite images, we used the normalised difference vegetation index (NDVI), and the normalised difference moisture index (NDMI) derived from Sentinel-2 imagery to classify the land cover. NDVI and
 1350 NDVI were calculated using Eq. (17) and Eq. (21), respectively. For machine learning, Support Vector Machine (SVM) algorithms were used to classify the oil palm tree plantations from the other landcovers. The UAV images, taken on 4 March 2017, 29 July 2018, and 5 November 2019, were used as the ground truth of the land cover. The precision of the land cover classification was evaluated by calculating the true positive rate, recall, specificity, precision, negative predictive value and F-score based on the confusion matrix. The dividing lines were calculated with palm oil plantation vegetation as true positives
 1355 (TP) and other types of land cover as false negatives (FN).

$$NDMI = \frac{B8A - B11}{B8A + B11} \quad (21)$$

Where B8A represents the NIR with 20 m resolution (wavelength: 865 nm); B11 represents the SWIR with 20 m resolution (wavelength: 1610 nm). According to Mandanici and Bitelli, 2016, the Pearson correlation coefficient and the slope of the linear relationship between the reflectance and index values of the multispectral instrument (MSI) and the TM5 bands are as close to 1 as possible, with the intercept close to 0. Therefore, the machine learning model for land cover classification created for Sentinel-2 images was applied directly to Landsat5 images.

As a result of the machine learning of the landcover classification using NDVI and NDMI, we got the partition line separating vegetation area and bare land area given by Eq. (22). Validation results of the machine learning were as follows: true positive rate, 0.8804; recall, 0.6940; specificity, 0.9950; precision, 0.9885; negative predictive value, 0.8410; and F-score, 0.4077.

$$NDMI = 0.5198NDVI + 0.7505 \quad (22)$$

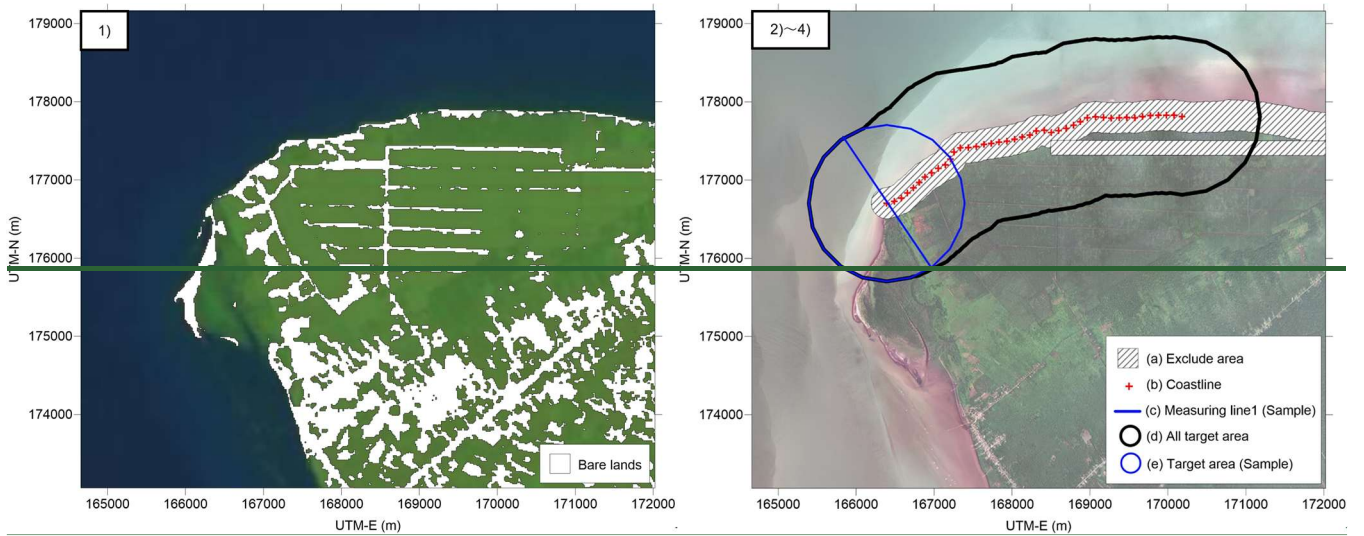


Figure 7: Methodology of removal of vegetation from DEMNAS data. 1) A Landsat5 image (2 February 2010) was used to classify bare land and other land covers using machine learning. 2) The bare land raster was set at 1 and multiplied by the DEMNAS data to produce the bare land elevation data. The elevation anomalies at the boundary between the peat swamp forest and the bare road and a radius of 200 m from the coastline (a) were masked. 3) A measuring line was made in the offshore direction from inland at points where the coastline was divided at 100 m intervals (b) (c). 4) The median elevation of the bare lands located 1 km (d) (e) from the coastline was assigned to the coastline and linearly complemented.

Appendix E: Vegetation removal from DEMNAS data

Because DEMNAS is a DSM that contains the tree height (vegetation), we removed the tree height from the DSM to make DTM. First, the bare lands in the research area in Landsat 5 image taken on 2 February 2010 were identified by the classifier

that was established in 3.2.1 and binarized. The binarized bare land area and DEMNAS data were combined to extract elevation values for bare land. During this process, the peat swamp forest and adjacent bare road and a radius of 200 m from the coastline that were flagged as anomalies were masked (Fig. E17a). The 200 m radius DEMNAS data depicted collapsed terrain, which would not need to remove tree heights; therefore, these areas were excised. The DEMNAS derived coastline, which the points of the altitudes of 0 m at 100 m intervals were extracted (Fig. E17b). An approximation of the polynomial curve of the extracted coastline was calculated and a 2 km offshore measurement line was constructed centred on the coast (Fig. E17c). The radius of 1 km from the coastline was set as a buffer area for buffer analyses in GIS to obtain elevation of the bare land (Figs. E17d and E17e). For any point in which statistical values were not attainable, linear interpolation was applied between adjacent points. The elevation difference from the median bare land elevation was considered as tree heights and the difference was subtracted to calculate the bare land elevation. Values above 0 m elevation were used to interpolate by kriging to generate a DTM with an 8 m resolution.

Fig. E2 shows the differences in the DEMNAS before and after vegetation removal. The median elevation values of the bare land within 1 km from coastline were used in the vegetation removal from the DEMNAS data. Comparison between ground surface geodetic survey results by Real Time Kinematic-Global Navigation Satellite System (RTK-GNSS) and DEMNAS data after vegetation removal are presented in Fig. E3. The RMSE of the ground elevation obtained from the RTK-GNSS and DEMNAS data after vegetation removal was 0.6951 m. The RMSE was subtracted from the DSM obtained from the UAV aerial photogrammetry to match the DEMNAS elevation. This elevation difference can be caused from by the skewness by the elevation decline because of the waterway.

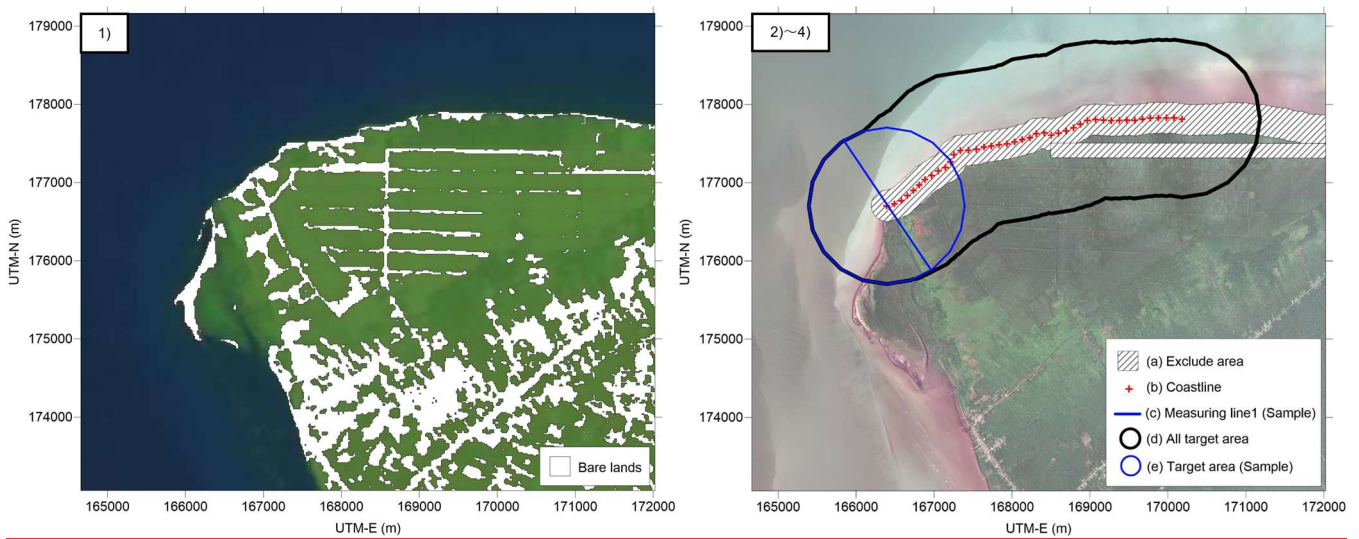


Figure E17: Methodology of removal of vegetation from DEMNAS data. 1) A Landsat5 image (2 February 2010) was used to classify bare land and other land covers using machine learning. 2) The bare land raster was set at 1 and multiplied by the DEMNAS data

to produce the bare land elevation data. The elevation anomalies at the boundary between the peat swamp forest and the bare road and a radius of 200 m from the coastline (a) were masked. 3) A measuring line was made in the offshore direction from inland at points where the coastline was divided at 100 m intervals (b) (c). 4) The median elevation of the bare lands located found 1 km (d) (e) from the coastline was assigned to the coastline and linearly complemented.

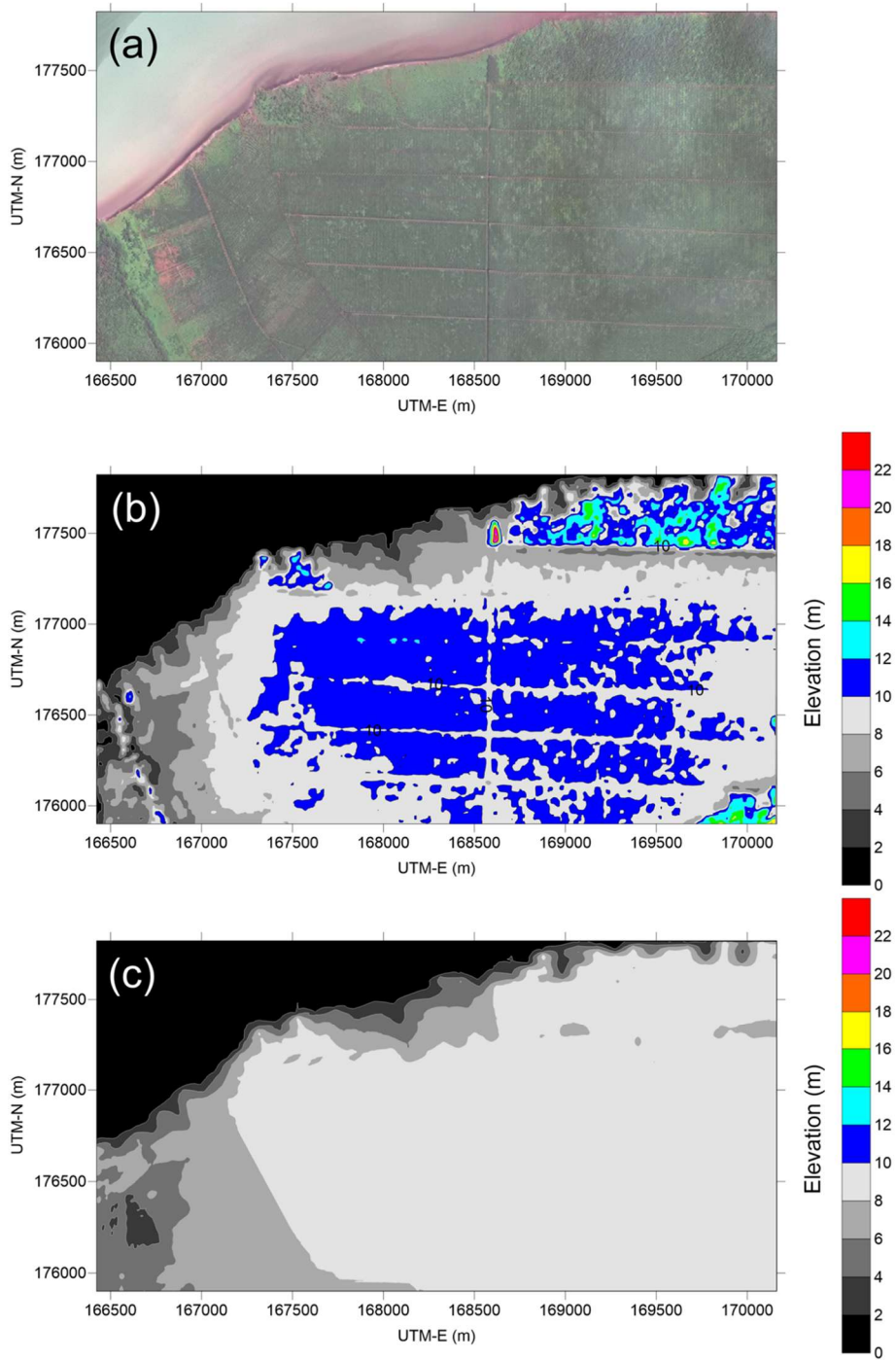


Figure E2: Comparison of (a) SPOT-6 data with (b) original DEMNAS data with (c) DTM removed from vegetation. The elevation of the bare land above 0 m was used to interpolate and generate a DTM with an 8 m resolution by kriging.

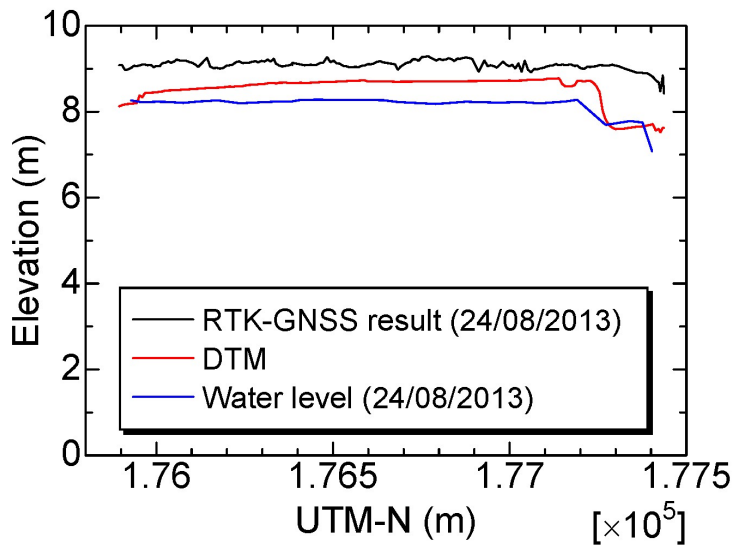


Figure E3: Comparison of the RTK-GNSS land survey with a section created from DEMNAS data. The section where the elevations of DTM has decreased was the section where the collapse was identified in December 2013 after the RTK-GNSS land survey. The RMSE of removing the landslide-affected area was 0.6951 (m).

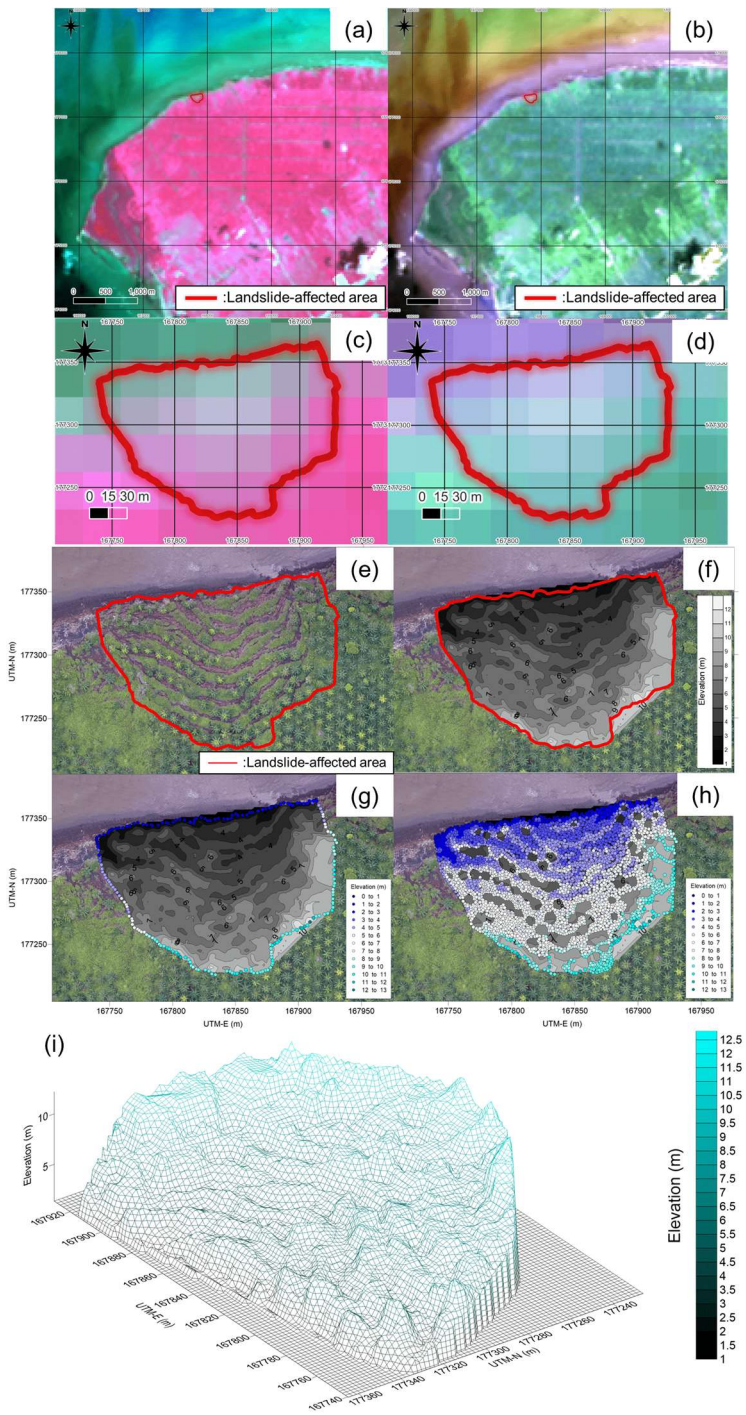
1415

Appendix FA: Comparison of optical satellite images and UAV-based orthomosaic and estimation methodology of the volume of the land slide-induced exported peat to the ocean

1420

In this study, optical satellite imagery and UAV-based orthomosaic were used to identify landslide-affected areas and coastlines. A comparison of Landsat8 imagery, which has a resolution equivalent to Landsat5, the lowest resolution of the optical satellites used, and UAV-based orthomosaic Landslide-affected areas at the same location is shown (Figs. FA1a, FA1b, FA1c, FA1d and FA1e; described in Sect. 3.2.4 and Sect. 3.2.6). Errors due to tracing were considered to vary depending on the resolution of the imagery, such as low-resolution satellite imagery, high-resolution satellite imagery and UAV-based orthomosaic, as the landslide-affected area and coastline cannot be identified unless the zoom is adjusted so that a wide area is visible, depending on the resolution of the imagery (Figs. FA1a, FA1b, FA1c, FA1d and FA1e; described in Sect. 3.2.4 and Sect. 3.2.6). The process in GIS software of estimated the volume of peat exported to the ocean is shown (Figs. FA1e, FA1f, FA1g, FA1h, and FA1i; described in Sect. 3.2.3).

1425



1430 **Figure FA1:** Comparison of optical satellite images and UAV-based orthomosaic and the process in GIS software of estimating the volume of peat exported to the ocean. (a) Landslide-affected-area identified by wide-area visibility and UAV-based orthomosaic (4 March 2017) in Landsat 8 false colour image (9 March 2017). (b) Landslide-affected-area identified by wide-area visibility and UAV-

based orthomosaic (4 March 2017) in Landsat 8 true colour image (9 March 2017). (c) Landslide-affected-area identified by zoomed-area visibility and UAV- based orthomosaic (4 March 2017) in Landsat 8 false colour image (9 March 2017). (d) Landslide-affected-area identified by zoomed-area visibility and UAV- based orthomosaic (4 March 2017) in Landsat 8 true colour image (9 March 2017). (e) Landslide-affected-area identified by UAV- based orthomosaic (4 March 2017). (f) DEM was post-collapse DEM, which were generated by sampling elevation data in the landslide-affected areas of vegetation removed DSM. (g) Elevation points at the edge of the DSM of the landslide affected area extracted to recreate the initial land surface. (h) Elevation points (4,516 points) inside the DSM of the landslide-affected area extracted to recreate the DEM after collapse. (i) Shape of the collapse site with the vegetation removed.

Appendix [GB](#): Error evaluation method for traced coastal erosion areas and landslide-affected areas in GIS software

This study considered traced errors in coastal erosion areas and landslide-affected areas, which were calculated by manual tracing in GIS software. The concept of an error evaluation method for traced coastal erosion areas and landslide-affected areas on GIS software is presented in Fig. [GB1](#). When considered at the scale of one pixel in the image, it was assumed that the manually traced lines would have trace errors within one pixel. Therefore, the traced error will depend on the resolution. Here, for the case where Google Earth was used, it was assumed that a tracing error equivalent to that of Landsat5 would occur, as the resolution was not opened. For cases where low-resolution images are used, the tracing errors are greater because the landslide-affected area and the coastline cannot be identified without scaling the scale (Figs. A1a, A1b, A1c, A1d and A1e). Errors in tracing planes also affect the calculation of volumes. Traced errors were also reflected in volume calculations.

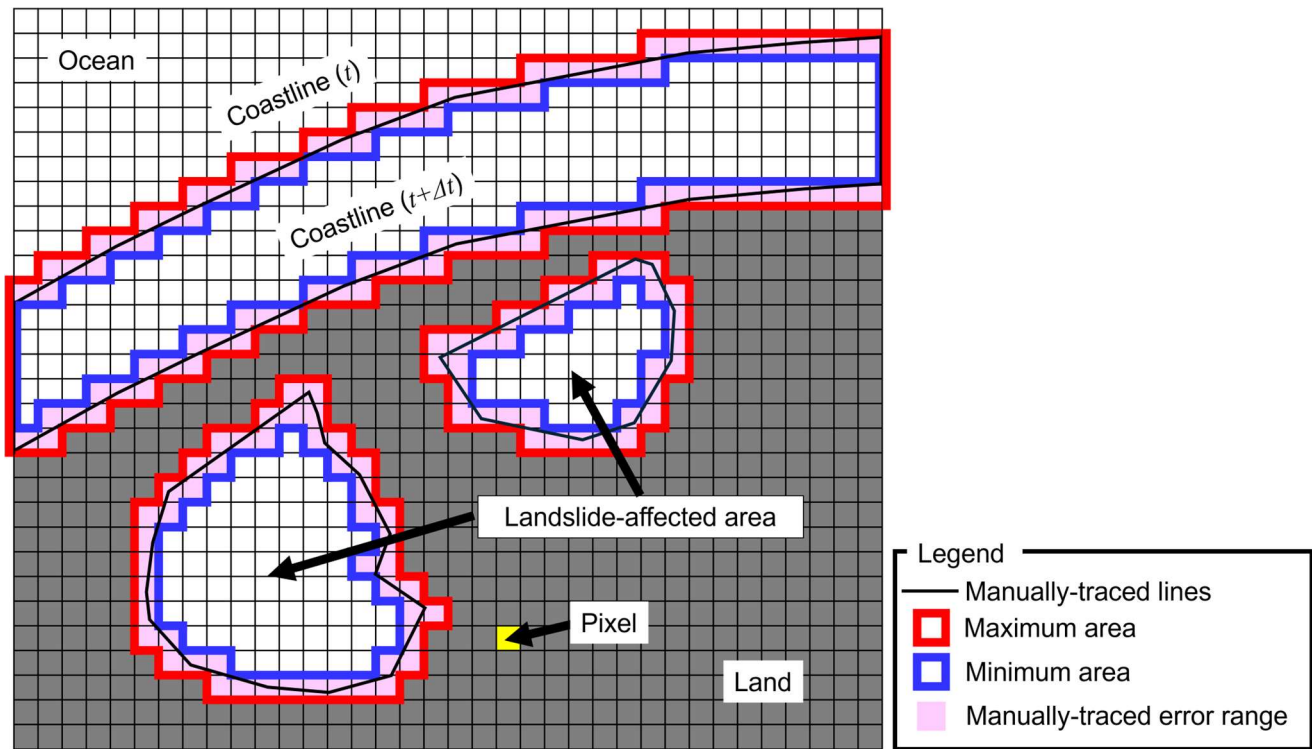


Figure G1B: Concept of the error evaluation method for traced coastal erosion areas and landslide-affected areas in the GIS software. Manual tracing errors tend to be resolution dependent.

1455

Appendix HC: Evaluation of resolution-induced errors using Landsat 8 and Sentinel-2 imagery

We evaluated the errors caused by differences in resolution using satellite images from Landsat 8 and Sentinel-2 acquired at the same time ($n=7$). To achieve this, we conducted 20 tracings per time for comparison. Using Landsat 8 with a 30 m resolution and Sentinel-2 with a 10 m resolution, landslide-affected areas captured at the same time were manually traced, and the error was evaluated (Fig. CH1). Larger collapses exhibited greater tracing errors, with an overall RMSE of 0.608. ha the results also indicate that tracing variability is greater with Landsat 8, which has a lower resolution.

1460

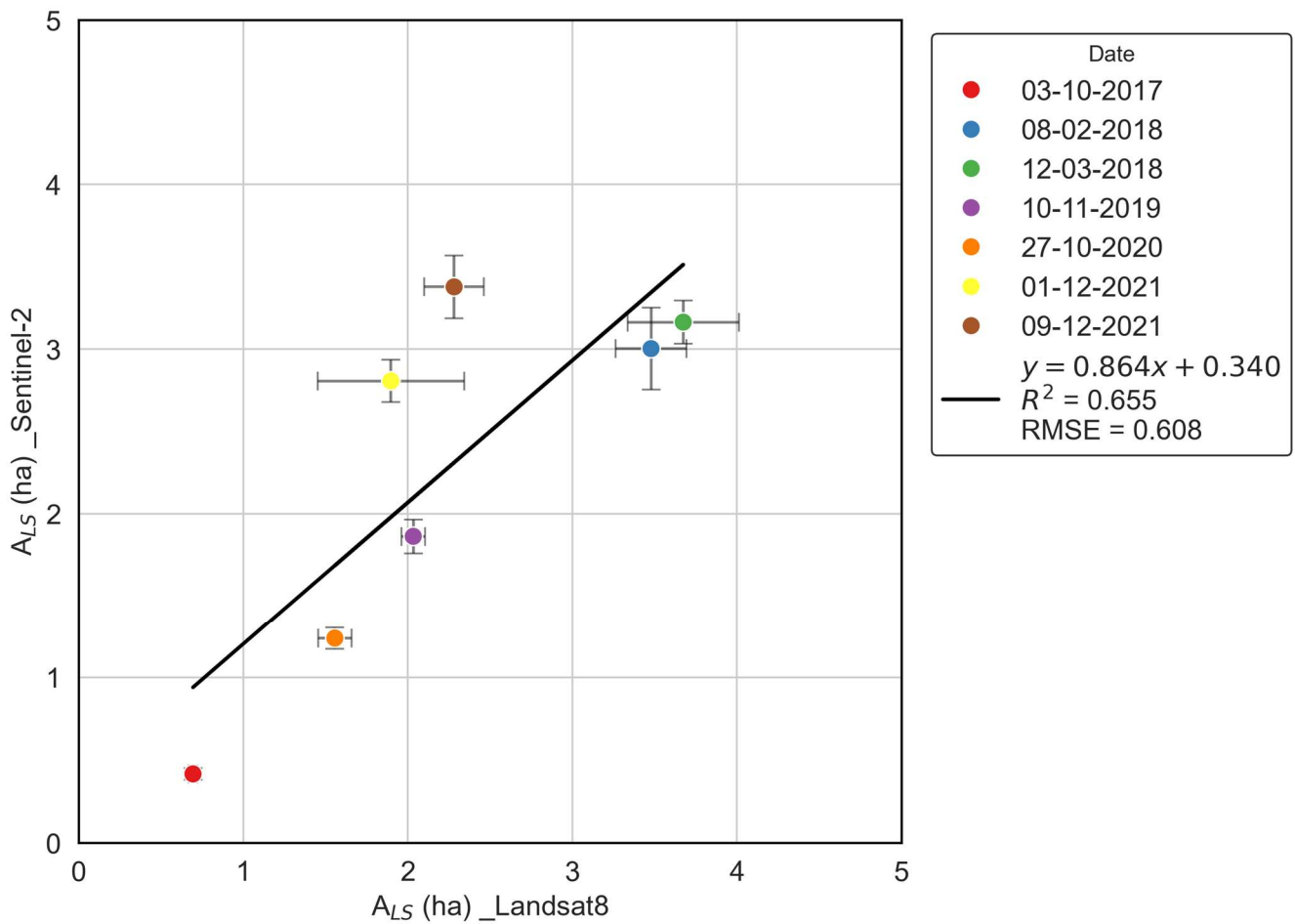


Figure H1C: Evaluation of resolution-induced errors using Landsat 8 and Sentinel-2 imagery.

1465 *Authors' contributions.* HK: Writing of the original draught and data analysis. KY: Conceptualisation, Field survey planning, Field survey, and Data analysis. SS: Aerial photogrammetry. MH: Soil sampling. SS and NB: Aerial photogrammetry. AKoyama: Field survey and Soil sampling. AKanno: Field survey. YA, MS: Field survey. All authors contributed to the interpretation of the results and the writing and editing of the final manuscript.

1470 *Competing interests.* The authors declare that they have no conflict of interest.

Acknowledgements. This work was supported by JSPS KAKENHI (Grant Numbers 17H01668 and 26303015). The fieldwork was supported by staff and students from the Bengkalis State Polytechnic and the University of Riau. Particulate organic carbon analysis was performed at Saga University with the help of Prof. Yuichi Hayami and Dr. Kenji Yoshino. We also thank
1475 Editage (www.editage.jp) for the English language editing.

References

- [Alexander, R.W., Coxon, P., Thorn, R.H.: A bog flow at Straduff Townland, county Sligo. Proc. R. Ir. Acad. 86B, 107-119, 1986.](#)
- 1480 Basir, N., Hiraishi, T., and Jauhari, Z. A.: The Ability of Red Mangrove, Gray Mangrove, and Mangrove Palm to Reduce Erosion Rate at The Northern Coast of Bengkalis Island Indonesia, in: Proceedings of 11th Applied Business and Engineering Conference (ABEC 2023) (Bengkalis, Indonesia), 2023.
- [Baum, A., Rixen, T., and Samiaji, J.: Relevance of peat draining rivers in central Sumatra for the riverine input of dissolved organic carbon into the ocean, Estuarine, Coastal and Shelf Science 73, 563-570, 2007.](#)
- 1485 Bjerrum, L.: Progressive failure in slopes of overconsolidated plastic clay and clay shales. ASCE Journal of Soil Mechanics and Foundations Division, Vol. 93, SM5, 3-49, 1967.
- Bowes, D.R.: A bog-burst in the Isle of Lewis. Scott. Geogr. J. 76, 21-23, 1960.
- Boylan, N., Jennings, R., Long, M.: Peat slope failure in Ireland. Q. J. Eng. Geol. Hydrogeol. 41 (1), 93-108, 2008.
- ~~[Brown, J., Jorgenson, M. T., Smith, O. P. and Lee, W.: Long-term rates of coastal erosion and carbon input, Elson Lagoon, Barrow, Alaska, Swets & Zeitlinger, Lisse, ISBN 90-5809-582-7, 2003.](#)~~
- ~~[Charity, S., Dudley, N., Oliveira, D., Stolton, S. \(eds.\): Living Amazon Report 2016: A Regional Approach to Conservation in the Amazon. WWF Living Amazon Initiative, Brasilia and Quito, 112, 2016.](#)~~
- Chambers, L. G., Steinmuller, H. E. and Breithaupt, J. L.: Toward a mechanistic understanding of “peat collapse” and its potential contribution to coastal wetland loss, Ecology, 100(7), 2019.
- 1495 Chevallier, D., Glrondot, M., Péron, C., Martin, J., Bonola, M., Chevalier, J., Thoisy, B. D., Kelle, L., Maho, Y. L., Gardel, A. and Anthony, E. J.: Beach erosion aggravates the drastic decline in marine turtle populations in French Guiana, Regional Environmental Change, 23:116, 2023.
- Couwenberg, J., Dommain, R., and Joosten, H.: Greenhouse gas fluxes from tropical peatlands in south-east Asia, Global Change Biology, 16, 1715–1732, 2010.
- ~~[Coxon, P., Coxon, C.E., Thorn, R.H.: The Yellow River \(County Leitrim, Ireland\) flash flood of June 1986. In: Beven, K., Carling, P. \(Eds.\), Floods: Hydrological, Sedimentological and Geomorphological Implications. Wiley, Chichester, pp. 199-217, 1989.](#)~~
- ~~[Crisp, D.T., Rawes, M., Welch, D.: A Pennine peat slide. Geogr. J. 130 \(4\), 519-524, 1964.](#)~~
- 1505 Dariah, A., Susanti, E., Mulyani, A., and Agus, F.: Predictor factor of carbon stock in peat soils. In: Husen et al. (eds.) Sustainable Peatland Management, Indonesian Agency for Agriculture Research and Development, Ministry of Agriculture, Bogor, Indonesia, 213–221, 2012.

- Day, J. W., Christian, R. R., Boesch, D. M., Yanez-Arancibia, A., Morris, J., Twilley, R. R., Naylor, L., Schaffner, L. and Stevenson, C.: *Consequences of climate change on the ecogeomorphology of coastal wetlands. Estuaries and Coasts* 31:477–491, 2008.
- 1510 Dommain, R., Couwunberg, J., and Joosten, H.: Development and carbon sequestration of tropical peat domes in south-east Asia: links to post-glacial sea-level changes and Holocene climate variability, *Quaternary Science Reviews*, 30, 999–1010, 2011.
- ~~Dugan, P.: *Wetlands in Danger*. Michael Beasley, Reed International Books, London. 192, 1993.~~
- 1515 ~~Dykes, A.P., Kirk, K.J.: Slope instability and mass movements in peat deposits. In: Martini, I.P., Marti'nez Cortizas, A., Chesworth, W. (Eds.), *Peatlands: Evolution and Records of Environmental and Climatic Changes*. Elsevier, Amsterdam, pp. 377–406 (Chapter 16), 2006.~~
- Dykes P, A. and Warburton, J.: Mass movements in peat: A formal classification scheme, *Geomorphology* 86, 73–93, 2007.
- ~~Dykes, A.P., Warburton, J.: Geomorphological controls on failures of peat covered hillslopes triggered by extreme rainfall. *Earth Surf. Process Landforms* 32, 1841–1862, 2007b.~~
- 1520 Dykes, A.P., Jennings, P.: Peat slope failures and other mass movements in western Ireland, August 2008. *Q. J. Eng. Geol. Hydrogeol.* 44 (1), 5–16, 2011.
- [Evans, M. and Lindsay, J.: Impact of gully erosion on carbon sequestration in blanket peatlands. *Climate Research Clim Res* Vol. 45, 31–41, 2010.](#)
- 1525 ~~Evans, M. G. and Warburton, J.: Sediment budget for an eroding peat moorland catchment in Northern England. *Earth Surface Processes and Landforms* 30(5): 557–77, 2005.~~
- ~~Evans, M. and Warburton, J.: *Geomorphology of Upland Peat (Erosion, Form and Landscape Change)*, RGS-IBG book series, Blackwell Publishing, pp.262, 2007.~~
- ~~Frolking, S., Talbot, J., Jones, M. C., Treat, C. C., Kauffman, J. B., Tuittila, E. S., and Roulet, N.: Peatlands in the Earth of the 21st century climate system, *Environmental Review*, 19, 371–396, 2011.~~
- 1530 Furmanczyk, K., and Dudzinska-Nowak, J.: Effects of extreme storms on coastline changes: a southern Baltic example. *J. Coast. Res.* 1637–1640, 2009.
- Galy, V., Peucker-Ehrenbrink, B., and Eglinton, T.: Global carbon export from the terrestrial biosphere controlled by erosion, *Nature*, 521, 204–207, 2015.
- 1535 ~~Harper, J.R.: Coastal erosion rates along the Chukchi Sea coast near Barrow, Alaska, *Arctic* 31: 428–433, 1978.~~
- ~~Hedges, J.I., Quay, P.D., Grootes, P.M., Richey, J.E., Devol, A.H., Farwell, G.W., Schmidt, F.W., and Salati, E.: Organic Carbon-14 in the Amazon River system: *Science*, v.231, 1129–1131, 1986.~~
- ~~Hedges, J.I. and Keil, R.G.: Sedimentary organic matter preservation: an assessment and speculative synthesis, *Marine Chemistry*, 49, 81–115, 1995.~~
- 1540 Hilton, R. G., Galy, V., Gaillardet, J., Dellinger, M., Bryant, C., O'Regan M., Gröcke, D.R., Coxall, H., Bouchez, J., and Calmels, D.: Erosion of organic carbon in the Arctic as a geological carbon dioxide sink, *Nature*, 524, 84–87, 2015.

- Hirano, T., Segah, H., Harada, T., Limin, S., June, T., Hirata, R., and Osaki, M.: Carbon dioxide balance of a tropical swamp forest in Kalimantan, Indonesia, *Global Change Biology*, 13, 412–425, 2007.
- Hirano, T., Segah, H., Kusin, K., Limin, S., Takahashi, H., and Osaki, M.: Effects of disturbances on the carbon balance in tropical peat swamp forests, *Global Change Biology*, 18, 3410–3422, 2012.
- 1545 ~~Hirano, T., Segah, H., Harada, T., Limin, S., June, T., Hirata, R., and Osaki, M.: Carbon dioxide balance of a tropical swamp forest in Kalimantan, Indonesia, *Global Change Biology*, 13, 412–425, 2007.~~
- ~~Hirano, T., Segah, H., Kusin, K., Limin, S., Takahashi, H., and Osaki, M.: Effects of disturbances on the carbon balance in tropical peat swamp forests, *Global Change Biology*, 18, 3410–3422, 2012.~~
- Hirano, T., Kusin, K., Limin, S., and Osaki, M.: Carbon dioxide emissions through oxidative peat decomposition on burnt tropical peatland, *Global Change Biology*, 20, 555–565, 2014.
- 1550 Hooijer, A., Page, S., Canadell, J. G., Silvius, M., Kwadijk, J., Wösten, H., and Jauhiainen, J.: Current and future CO₂ emissions from drained peatlands in Southeast Asia, *Biogeosciences*, 7, 1505–1514, 2010.
- ~~Hume, J.D. and Schalk, M.: Shoreline processes near Barrow, Alaska: a comparison of the normal and the catastrophic, *Arctic* 20: 86–103, 1967.~~
- 1555 ~~Hume, J.D., Schalk, M. and Hume, P.W.: Short term climate changes and coastal erosion, Barrow, Alaska, *Arctic* 25: 272–278, 1972.~~
- ~~Hussein, A. H.: Modeling of sea level rise and deforestation in submerging coastal ultisols of Chesapeake Bay. *Soil Science Society of America Journal* 73:185–196, 2009.~~
- ~~IPCC. 2007. Climate change 2007: the physical science basis: contribution of working group I to the fourth assessment report of the intergovernmental panel on climate change. S. Solomon, D. Qin, M. Manning, Z. Chen, M. Marquis, K. B. Averyt, M. Tignor, and H. Miller, editors. Cambridge University Press, Cambridge, UK, 2007.~~
- 1560 ~~IPCC. 2007. Climate change 2007: the physical science basis: contribution of working group I to the fourth assessment report of the intergovernmental panel on climate change. S. Solomon, D. Qin, M. Manning, Z. Chen, M. Marquis, K. B. Averyt, M. Tignor, and H. Miller, editors. Cambridge University Press, Cambridge, UK, 2007.~~
- Kagawa, H., Yamamoto, K., Haidar, M., Kanno, A., Akamatsu, Y., Suzuki, M., Sutikno, S., Basir, N., and Sekine, M.: Present condition of coastal erosion in the Islands in Riau Province, Indonesia, in: Proceedings of the Civil Engineering Society G (Environment) (Collection of Research Papers on Environmental Engineering), 73(7), III_213–III_219, 2017.
- 1565 ~~Kirk, K.J.: Instability of Blanket Bog Slopes on Cuileagh Mountain, N.W. Ireland (Unpublished Ph.D. thesis). University of Huddersfield, U.K., 2001.~~
- Kleinen, T., Brovkin, V., von Bloh, W., Archer, D., and Munhoven, G.: Holocene carbon cycle dynamics, *Geophysical Research Letters*, 37, L02705, 2010.
- 1570 Koyama, A., Yamamoto, K., Sutikno, S., Basir, N., and Suzuki, M.: Investigation of Peat Landslide in Indonesia Bengkalis Island by Sounding Test, in: Proceedings of 53rd Geotechnical Engineering Research Meeting (Takamatsu City), 2018.

- 1575 ~~Krauss, K. W., Cahoon, D. R., Allen, J. A., Ewel, K. C., Lynch, J. C., and Cormier, N.: Surface elevation change and susceptibility of different mangrove zones to sea level rise on Pacific high islands of Micronesia. *Ecosystems* 13:129–143, 2010.~~
- ~~Kreuzburg, M., Ibenthal, M., Janssen, M., Rehder, G., Voss, M., Naumann, M. and Feldens, P.: Sub-marine Continuation of Peat Deposits from a Coastal Peatland in the Southern Baltic Sea and its Holocene Development, *Frontiers in Earth Sciences*, Volume 6, Article 103, 1–12, 2018.~~
- 1580 Lantuit H. and Pollard W.H.: Fifty years of coastal erosion and retrogressive thaw slump activity on Herschel Island, southern Beaufort Sea, Yukon Territory, Canada, *Geomorphology* 95, 84–102, 2008.
- Lantuit, H., Atkinson, D., Overduin, P. P., Grigoriev, M., Rachold, V., Grosse, G. and Hubberten, H. W.: Coastal erosion dynamics on the permafrost-dominated Bykovsky Peninsula, north Siberia, 1951–2006, *Polar Research*, 30:1, 7341, 2011.
- 1585 ~~Lehfeldt, R., and Milbradt, P.: “Longshore sediment transport modelling in 1 and 2 dimensions, in: advances in Hydro science and engineering,” in: *Proceedings of the 4th International Conference on Hydro Science and Engineering Abstract (Seoul), 2000.*~~
- Ludwig, W., Probst, J. L., and Kempe, S.: Predicting the oceanic input of organic carbon by continental erosion, *Global Biogeochemical Cycles*, 10(1), 23–41, 1996.
- ~~MacCarthy, G.R.: Recent changes in the shoreline near Point Barrow Alaska, *Arctic* 6: 44–51, 1953.~~
- 1590 ~~Mandanici, E. and Bitelli, G.: Preliminary Comparison of Sentinel 2 and Landsat 8 Imagery for a Combined Use, *Remote sensing*, 8, 1014, 1–10, 2016.~~
- Malpica-Piñeros, C., Barthelmes, A. and Joosten, H.: What, when and how? A review of peatland research in Amazonia, *Mires and Peat*, Volume 31, Article 03, 26, 2024.
- 1595 ~~Mariotti, G., and Fagherazzi, S.: A numerical model for the coupled long-term evolution of salt marshes and tidal flats, *Journal of Geophysical Research: Earth Surface* 115:1–15, 2010.~~
- ~~Mayorga, E., Aufdenkampe, A.K., Masiello, C.A., Krusche, A.V., Hedges, J.I., Quay, P.D., Richey, J.E., and Brown, T.A.: Young organic matter as a source of carbon dioxide outgassing from Amazonian rivers, *Nature*, v.436, 538–541, 2005.~~
- 1600 [Matsuo, H., Yamamoto, K., Imai, T., Nakamura, S., Kagawa, H., Sigit, S., Ahmad, M., Muhamad, Y., Hendra, S.: Flotation of Peat Particles by Dissolved Organic Matter Eluted from the Re-Deposited Tropical Peat in Tropical Peatland Coast. *Journal of Water and Environment Technology*, Vol 23, No.3, 167–178, 2025.](#)
- McCahon, C.P., Carling, P.A., Pascoe, D.: Chemical and ecological effects of a Pennine peat-slide. *Environ. Pollut.* 45, 275–289, 1987.
- 1605 ~~Mills, A.J., 2002. *Peat Slides: Morphology, Mechanisms and Recovery* (Unpublished Ph.D. thesis). University of Durham, UK, 2002.~~
- Ministry of the Environment White Paper, Introduction, Section 1, Subsection 2: Global Environment, 2002.

- Mopper, K., Zhou, X., Kieber, R.J., Kieber, D.J., Sikorski, R.J., and Jones, R.D.: Photochemical degradation of dissolved organic carbon and its impact on the oceanic carbon cycle, *Nature*, 605 353, 60–62, 1991.
- 1610 [Nabilah, D. H., Wibowo, A. A., and Wardan, K. S.: Detection of Peatland Coastline Changes Due to Land Use Change On Bengkalis Island, Riau, Indonesia, in: Proceedings of 5th International Conference of Geography and Disaster Management 2023 \(Online\), 2024.](#)
- Nicholls, R. J., Hoozemans, F. M. J. and ~~Marehand, M~~[Marchand, M.](#): Increasing flood risk and wetland losses due to global sea-level rise: regional and global analyses. *Global Environmental Change—Human and Policy Dimensions* 9: S69–S87, 1999.
- 1615 Osaki, M. and Tsuji, N.: Tropical peatland ecosystems, Springer Tokyo, 633pp, 2016.
- [Page, S.E., Siegert, F., Rieley, J.O., Boehm, H.D.V., Jaya, A., and Limin, S.: The amount of carbon released from peat and forest fires in Indonesia during 1997, *Nature*, 420, 61–65, 2002.](#)
- ~~Page, S.E., Siegert, F., Rieley, J.O., Boehm, H.D.V., Jaya, A., and Limin, S.: The amount of carbon released from peat and forest fires in Indonesia during 1997, *Nature*, 420, 61–65, 2002.~~
- 1620 Page, S.E., Rieley, J., and Banks, C.: Global and regional importance of the tropical peatland carbon pool, *Global Change Biology*, 17, 798–818, 2011.
- [Pawson, R.R., Rothwell, J.J., Daniels, D. R., Evans, M.G.E. and Allott, T.E.H.: Fluvial organic carbon flux from an eroding peatland catchment, southern Pennines, UK, *Hydrol. Earth Syst. Sci. Discuss.*, 4, 719–745, 2007.](#)
- [Pawson, R. R., Evans, M. G. and Allott, T. E. H.: Fluvial carbon flux from headwater peatland streams: Significance of particulate carbon flux, *Earth Surface Processes and Landforms*, 37\(11\), 1203–1212, 2012.](#)
- 1625 Rachold, V., Brown, J. and Solomon, S. (eds): Arctic Coastal Dynamics-Report of an International Workshop, Reports on Polar and Marine Research, 413, 103, 2002.
- ~~Richey, J.E., Melack, J.M., Aufdenkampe, A.K., Ballester, V.M., and Hess, L.L.: Outgassing from Amazonian rivers and wetlands as a large tropical source of atmospheric CO₂, *Nature*, v.416, 617–620, 2002.~~
- 1630 Ritung, S., Wahyunto, Nugroho, K., Sukarman, Hikmatullah, Suparto, and Tafakresnanto, C.: Tim Penyusun Peta Lahan Gambut Indonesia Skala 1:250.000 (Indonesian peatland map at the scale 1:250,000), Indonesian Center for Agricultural Land Resources Research and Development, Bogor, Indonesia, 2011.
- Rudiyanto, Minasny, B., Satyanto, B.I., Saptomo, S.K., and McBratney, A.B.: Open digital mapping as a cost-effective method for mapping peat thickness and assessing the carbon stock of tropical peatlands, *Geoderma*, 313, 25–40, 2018.
- 1635 Scharlemann, J. P., Tanner, E. V., Hiederer, R. and Kapos, V.: Global soil carbon: understanding and managing the largest terrestrial carbon pool, *Global soil carbon: understanding and managing the largest terrestrial carbon pool*, *Carbon Management*, 5:1, 81-91, 2014.
- ~~Schwimmer, R.: Rates and processes of marsh shoreline erosion in Rehoboth Bay, Delaware, USA. *Journal of Coastal Research* 17:672–683, 2001.~~
- 1640 ~~Sterr, H.: Assessment of vulnerability and adaptation to sea-level rise for the coastal zone of germany. *J. Coast. Res.* 24, 380–393, 2008.~~

- Supardi, Subekty, A.D., and Neuzil, S.G.: General geology and peat resources of Siak Kanan and Bengkalis Island peat deposits, Sumatra, Indonesia, Geological Society of America Special Paper, 286, 45–61, 1993.
- [Tolunay, D., Kowalchuk, G. A., Erkens, G., Hefting, M. M.: Aerobic and anaerobic decomposition rates in drained peatlands: Impact of botanical composition, Science of the Total Environment 930, 172639, 2024.](#)
- 1645 ~~Sutikno, S., Sandhyavitri, A., Haidar, M., and Yamamoto, K.: Shoreline Change Analysis of Peat Soil Beach in Bengkalis Island Based on GIS and RS, International Journal of Engineering and Technology. 9, 3, 233–238, 2017.~~
- Umarhadi, D. A., Widyatmanti, W., Kumar, P., Yunus, A. P., Khedger, K. M., Kharazi, A., and Avtar, R.: Tropical peat subsidence rates are related to decadal LULC changes: Insights from InSAR analysis, Science of the Total Environment, 816, 151561, 2022.
- 1650 US Army Map Service: Bengkalis, Series T503, NA48-9, 1955.
- ~~Vestergaard, P.: Possible impact of sea level rise on some habitat types at the Baltic coast of Denmark. J. Coast. Conserv. 3, 103, 1997.~~
- Wahyunto, Ritung, S., and Subagjo, H.: Peta Luas Sebaran Lahan Gambut dan Kandungan Karbon di Pulau Sumatera / Maps of Area of Peatland Distribution and Carbon Content in Sumatra: 1990–2002, Wetlands International—Indonesia Programme & Wildlife Habitat Canada (WHC), Bogor, Indonesia, 2003.
- 1655 Warburton, J., Holden, J., and Mills, A.J.: Hydrological controls of surficial mass movements in peat, Earth-Science Reviews, 67, 139–156, 2004.
- Warren, M.W., Kauffman, J.B., Murdiyarso, D., Anshari, G., Hergoualc’h, K., Kurnianto, S., Purbopuspito, J., Gusmayanti, E., Afifudin, M., Rahajoe, J., Alhamd, L., Limin, S., and Iswandi, A.: A cost-efficient method to assess carbon stocks in tropical peat soil, Biogeosciences, 9, 4477–4485, 2012.
- 1660 [Whittle, A. and Gallego-Sala, A. V.: Vulnerability of the peatland carbon sink to sea-level rise, Sci. Rep. 6, 28758, 2016.](#)
- Wilford, G. E.: Peat landslide in Sarawak, Malaysia, and its significance in relation to washouts in coal seams, Journal of sedimentary Research, 36(1), 244–247, 1966.
- 1665 [Witze, A.: Why arctic fires are bad news for climate change, unprecedented wildfires released record levels of carbon, partly because they burnt peatlands., Nature News in focus Vol.585, 2020.](#)
- ~~Wilson, P., Griffiths, D., Carter, C.: Characteristics, impacts and causes of the Carrtogether bog flow, Sperrin Mountains, Northern Ireland. Scott. Geogr. Mag. 112, 39–46, 1996.~~
- Wong, P. P., Losada, I. J., Gattuso, J.-P., Hinkel, J., Khattabi, A., McInnes, K. L., et al.: Coastal systems and low-lying areas. Clim. Change 2104, 361–409, 2014.
- 1670 Xu, J., Morris, P.J., Liu, J., and Holden, J.: PEATMAP: Refining estimates of global peatland distribution based on meta-analysis. University of Leeds. Online at <https://doi.org/10.5518/252>, accessed January 18, 2024, 2017.

- 1675 [Yamamoto, K., Watanabe, T., Okuyama, H., Haidar, M., Noerdin, B., Kanno, A. and Masahiko, S.: Peat Coast Erosion of the Bengkalis Island and its Effect on the Groundwater Discharge, in: Proceedings of the Civil Engineering Society B2 \(Coastal Engineering\), 70\(2\), I_1466–I_1470, 2014.](#)
- Yamamoto, K., Asakuma, T., Kagawa, H., Sutikno, S., Basir, N., and Kanno, A.: Occurrence and disappearance of temporary peat fan by the landslide at the coastal peat coast, in: Proceedings of the Civil Engineering Society B2 (Coastal Engineering) 75(2): I_1249–I_1254, 2019.
- 1680 ~~Yamamoto, K., Basir, N., Sutikno, S., Kanno, A., Kagawa, H., Suzuki, M., Akamatsu, Y., and Koyama, A.: Tropical peat debris storage in the tidal flat in northern Bengkalis Island, Indonesia, in: Proceedings of MATEC Web of Conferences, 276, 06002, 2019.~~
- Yamamoto, K., Watanabe, M., Kagawa, H., Matsumoto, A., Sutikno, S., and Koyama, A.: Elution of dissolved organic matter into coastal seawater from collapsed peat deposit, in: Proceedings of the Civil Engineering Society B2 (Coastal Engineering), 76(2), I_1333–I_1338, 2020.
- 1685 Yu, Z.: Holocene carbon flux histories of the world's peatlands: global carbon cycle implications, *The Holocene*, 21(5), 761–774, 2011.
- Yunker, M. B., Macdonald, R. W., Fowler, B. R., Cretney, W. J., Dallimore, S. R. and Mclaughlin, F. A.: Geochemistry and fluxes of hydrocarbons to the Beaufort Sea shelf: A multivariate comparison of fluvial inputs and coastal erosion of peat using principal components analysis, *Geochimica et Cosmochimica Acta* Vol.55, 255-273, 1991.